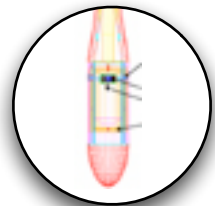


CHAPTER 3

GRAVITATION AND RELATIVITY PHYSICS



Progress in Developing a Superconducting Microwave Oscillator for Precision Measurements on Orbit

J. Nissen, J. A. Lipa, S. Wang, D. Avaloff, D. A. Stricker and S. Buchman, Y.C. Lin

*W. W. Hansen Experimental Physics Laboratory, Stanford University, Stanford, CA
94305, USA*

ABSTRACT

We describe the development of a superconducting microwave oscillator with high frequency stability for use aboard the International Space Station. The project has four main goals; an improved test of Local Position Invariance, improved Kennedy Thorndyke and Michelson–Morley special relativity tests, and an enhancement of the performance of atomic clocks being developed elsewhere for use in space. In addition precision clocks play an important role in experimental tests of Lorentz and CPT violation. Aboard the International Space Station, unwanted resonant–frequency variations are expected to be caused mainly by acceleration effects due to residual drag and vibration, temperature variations, and fluctuations in the energy stored in the cavity. In the past, acceleration effects appeared to be the predominant limit. A new cavity support system has been designed to reduce the acceleration effects and a fractional frequency sensitivity of 1 part in 10^{17} per μg has been demonstrated.

INTRODUCTION

On large length scales and under extreme conditions Einstein’s theory of general relativity encapsulates many of the fundamental physical laws used for predicting the intertwined behavior of matter and spacetime. One of the most fundamental aspects of this theory is the behavior of clocks. So far, clocks have been used to test the theory in three different ways. A hydrogen maser was used to measure the gravitational red shift¹ to about a part in 10^4 using a rocket flight to an altitude of 10,000 km. The time delay for electromagnetic signals passing close to the sun has been measured² to a part in 10^3 . Finally, the assumption of Local Position Invariance (LPI) in the Einstein Equivalence Principle has been tested³ to 2%. Beyond general relativity, clocks have been used to test some of the foundations of special relativity by looking for effects due to a possible anisotropy of the velocity of light⁴, and to set bounds⁵ on the present rate of change of the fine structure constant.

The LPI principle of general relativity states that clocks made in different ways all keep exactly the same time, no matter where they are co–located in the universe. This might not be true if some of the laws of physics vary slightly from place to place. One of our goals is to perform an improved LPI test by comparing the microwave cavity frequency with that of an atomic clock to a part in 10^{16} , as a function of position and gravitational potential as the Earth travels in its eccentric orbit around the Sun. A basis of the test is the observation that the frequencies of a microwave cavity and an atomic clock have different dependencies on fundamental physical constants³. Alternatively, one can view the experiment as setting limits on effects predicted by various theories competing with special relativity as descriptions of the interaction of matter and spacetime such as the Lorentz– and CPT–violating Standard–Model extension⁶.

Tests of the foundations of special relativity fall into two main classes: one involving angle-dependent effects and the other absolute velocity effects. A generalized treatment of the Lorentz transformations has been given by Mansouri and Sexl⁷ (1977) who consider the possibility of an anisotropic propagation velocity of light relative to a preferred frame. If a laboratory is assumed to be moving at a velocity v at an angle θ relative to the axis of a preferred frame, the speed of light as a function of θ is given by

$$c(\theta)/c = 1 + (1/2 - \beta + \delta)v^2/c^2 \sin^2\theta + (\beta - \alpha - 1)v^2/c^2 \quad (1)$$

where α is the time dilation parameter, β is the Lorentz contraction parameter, and δ tests for transverse contraction, to be determined either experimentally or in the particular theory being considered. In special relativity the last two terms on the right hand side of equation 1 are zero. In a Michelson–Morley experiment the amplitude of the θ –dependent term is measured, while in a Kennedy–Thorndyke experiment the amplitude of the θ –independent term is determined. To evaluate experiments it is often assumed that the preferred frame is the rest frame of the cosmic microwave background. In this case by far the biggest contributor to v is the apparent velocity of the earth along the anisotropy axis, approximately 370 km/sec.

With the advent of the International Space Station (ISS), substantially greater resolution is achievable for these relativity tests. The relative velocity of an experiment on the ISS would be modulated at the orbital period as measured in inertial coordinates giving rise to the periodically varying clock signal. Since the modulation of the velocity vector is due to the ISS orbital motion, it is clear that certain flight times could be more favorable than others to perform the experiment. Also, since the orbital plane precesses at approximately 5°/day, significant changes in the signal would be expected with time. This easily modeled signature would be valuable if an effect was detected. In the case of the θ –dependent class, a signal could be generated by mounting two cavities at right angles, since their frequencies are sensitive to the velocity of light only in the radial directions. At present the best limit⁸ on this form of isotropy is $(1/2 - \beta + \delta) < 3 \times 10^{-9}$. By comparing the frequencies of two orthogonally mounted cavities at twice orbital roll rate, the limit for this effect could be improved of a factor of about 300 with a few days averaging. The present limit⁹ on the Kennedy–Thorndyke term is $(\beta - \alpha - 1) < 6.6 \times 10^{-5}$. With an Allan variance of 5×10^{-16} referencing to an atomic clock, and averaging over 100 orbits, we would expect to set a limit of $\sim 8 \times 10^{-10}$, a factor of 8×10^4 improvement. This signal would be modulated at the orbital period.

With the advent of laser-cooled atoms, the prospects for substantially more stable atomic clocks have dramatically improved. It now appears that laser-cooled cesium and rubidium frequency standards with stability of better than 10^{-16} are feasible in space, and single atom clocks with a stability of 10^{-18} are discussed. When coupled with superconducting cavity oscillators (SCOs) these developments open up new possibilities for experiments in fundamental physics. In collaboration with the Jet Propulsion Laboratory we are developing a superconducting microwave oscillator (SUMO), a space version of the SCO. SUMO will be an insert in the Low Temperature Microgravity Physics Facility (LTMPF) and will require three to six months of operation in order to meet its science objectives. Longer-term experiments, using two or more oscillators and separate facilities, include precision red-shift measurements and possibly the detection of gravitational waves¹⁰. The possibility of using SCOs for pulsar timing in space has also been mentioned¹¹. SUMO should significantly augment the scope and capability of the space clock ensemble by acting as a high stability, low phase noise 'flywheel' when slaved to an atomic clock.

APPARATUS

The apparatus consists of a pair of superconducting cavities mounted on thermally controlled stages at 1.4 K and located in separate cryostats. The cylindrical-symmetry axis of one cavity was oriented horizontally. The axis of the other cavity was oriented vertically and acted as a reference for the cavity under test. This arrangement discriminates against common mode variations in the SCO such as helium level, acceleration and temperature variations which could be masked if the cavities were in the same cryostat. Magnetic shields were used to reduce the field at the cavity to $\sim 10^{-3}$ Gauss. The connections between the cavities and the room temperature electronics were made using stainless steel semi-rigid coaxial cable. The SCO electronics system utilized the high Q cavity resonance to stabilize a voltage-controlled oscillator (VCO). A small part of the power of the VCO was used to excite the cavity. This signal was frequency-modulated at 1 MHz, and the amplitude-modulated component reflected by the cavity was detected. The phase and amplitude of this signal represented the deviation of the VCO frequency from the cavity frequency, and were used to servo the VCO frequency. Figure 1 shows a block diagram of a frequency control loop. The VCO consisted of a voltage controlled 10 Mhz quartz oscillator which acted as a reference for a frequency modulated microwave synthesizer. The outputs from the two microwave synthesizers locked to individual cavities are beat against each other to produce difference frequencies of a few tens of Hz. This signal can be utilized to look for variations in the speed of light in two orthogonal cavities.

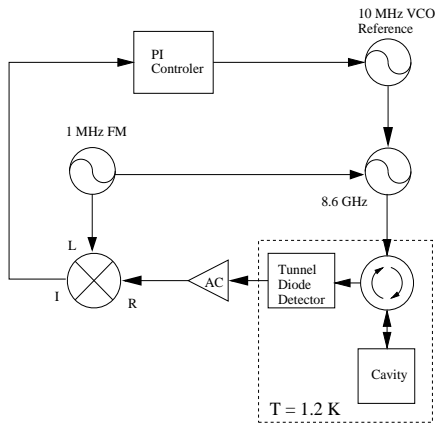


Fig. 1) SCO electronics block diagram.

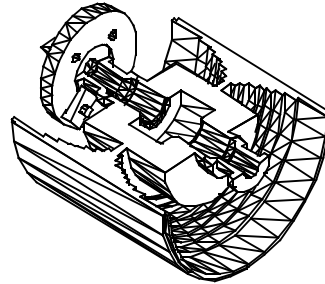


Fig. 2) Cutaway of the center mounted cavity.

RECENT PROGRESS

Accelerations of the cavity, such as that due to the earth's gravitational pull, cause distortions in the cavity shape. When these distortions change the radius of the cavity, they can cause a shift in the resonant frequency. To minimize the frequency changes that occur due to changing accelerations we have designed a supporting structure for the cavity that takes advantage of some of the symmetries in the cavity design. Figure 2 shows a cross-sectional view of a new cavity now in test. The design is based on a finite-element analysis of the effects of acceleration on the cavity dimensions, and numerical calculations of the fields inside the cavity at the walls, plus the perturbation of the energy of the fields in the cavity due to the wall displacement. Supporting the cavity radially around its center reduces the sensitivity of the frequency to acceleration because of symmetry. By varying the geometry of the supporting structure one can theoretically reduce the frequency shift to zero, but this would require precise control of cavity and support dimensions as well as a high confidence in the numeric calculation. In practice we can fine tune

the support structure by adding mass to the ends of the cavity. On the ISS the residual accelerations at very low frequencies are mostly caused by aerodynamic drag and are estimated to be below 10^{-6} g, potentially allowing fractional frequency stability in the 10^{-18} range

Evaluation of the case with the acceleration vector perpendicular to the axis of symmetry requires calculations performed with a full three dimensional model. When this vector is transverse, the overall displacement of the cavity is much greater than the non-symmetric distortions we are sensitive to. Because of this, numeric noise in the three dimensional calculations was clearly visible at the level of 10^{-19} $\Delta f/f$ per μg . For the models investigated there were no asymmetric distortions of the cavity above this numerical noise floor.

We mounted the center-supported cavity with its symmetry axis horizontal in order to maximize its sensitivity to axial acceleration when the cryostat is tilted. A second cavity in a fixed cryostat was used for the reference. The center mounted cavity had a Q of 2×10^9 at about 1.4K. It was tilted over a range of 2 degrees and a fractional frequency sensitivity of less than 1 part in 10^{17} per μg was measured.

Near 1.4K the temperature coefficient of the cavity frequency is typically $\Delta f/f \sim 3 \times 10^{-9}$ per degree. Thus to achieve a signal stability of 10^{-16} at orbital periods we need to control the cavity temperature to about $\pm 3 \times 10^{-8}$ K. The recent flight of the CHEX experiment¹² on the Shuttle has demonstrated that this is within the range of existing capability using advanced high resolution thermometry techniques. For SUMO we are using a new type of sensor¹³ made from a palladium-manganese alloy with 99.59 atomic percentage Pd and 0.41% Mn. This has a Curie temperature of about 1K¹⁴. The transition temperature of this alloy can be adjusted to any desired temperature below 4K by changing the concentration of Mn. Temperature control has been demonstrated to 300 nK indicating a fractional frequency stability of 10^{-15} in one second. For the half orbital period the temperature stability is dominated by thermometer drift.

The major issue with thermal control is the varying energy dump from charged particle radiation as the experiment moves around the ISS orbit. We can make an estimate of this effect by scaling from the observations on CHEX to the present situation. It is expected that the variations in the radiation environment will be as much as a factor of five worse on ISS relative to the 28° inclination Shuttle case, but we expect to have adequate margin relative to the $\pm 3 \times 10^{-7}$ K requirement. A more quantitative analysis is in progress.

CONCLUSIONS

We have described a project to place superconducting cavity oscillators in orbit on the ISS. Our recent measurements have achieved levels of $\sim 5 \times 10^{-16}$ for time scales of 100 to 3000 seconds at 1.4 K, competitive with modern atomic clocks. A design suitable for use in space is under development. On the ISS the cavities can be used in conjunction with atomic clocks to perform tests of relativity, and as low phase-noise flywheels for atomic fountain experiments. Our analysis of the limitations of superconducting cavity oscillators indicates that improvements to the 10^{-17} range are quite possible. Acceleration sensitivity measurements are consistent with this number and temperature stability is approaching this goal.

ACKNOWLEDGMENTS

We wish to thank the NASA Office of Life and Microgravity Sciences and Applications for its support with grants # NAG3-1940 and NAG8-1439, and J. Turneaure, W. Moeur and M. Dong for substantial assistance in the initial phases of the project.

REFERENCES

1. Vessot, R.F.C., et al., "Test of Relativistic Gravitation with a Space-Borne Hydrogen Maser", *Phys. Rev. Letts.*, **45**, 2081–2084 (1980).
2. Shapiro, I., "Fourth Test of General Relativity", *Phys. Rev. Letts.*, **13**, 789–791 (1964).
3. Turneaure, J.P., Will, C.M., Farrel, B.F., Mattison, E.M., and Vessot, R.F.C., "Test of the Principle of Equivalence by a Null Gravitational Red-Shift Experiment", *Phys. Rev. D*, **27**, 1705–1714 (1983).
4. Will, C.M., "Clock Synchronization and Isotropy of the One-Way Speed of Light", *Phys. Rev. D*, **45** 403–411 (1992).
5. Prestage, J.D., Tjoelker, R.L., and Maleki, L., "Atomic Clocks and Variations of the Fine-Structure Constant", *Phys. Rev. Letts.*, **74**, 3511–3514 (1995).
6. D. Colladay and V.A. Kostelecky, *Phys.Rev.D* **55**, 6760 (1997), 116002 (1998).
7. Mansouri, R. and Sexl, R.U., "A Test Theory of Special Relativity" *Gen. Rel. and Grav.*, **8**, 497 (1977).
8. Brillet, A., and Hall, J.L., "Improved Laser Test of the Isotropy of Space", *Phys. Rev. Letts.*, **42**, 549–552 (1979).
9. Hils, D., and Hall, J.L., "Improved Kennedy–Thorndike Experiment to Test Special Relativity", *Phys. Rev. Letts.*, **64**, 1697–1700 (1990).
10. Piran, T., Reiter, E., Unruh, W.G., and Vessot, R.F.C., "Filtering of Spacecraft Doppler Tracking Data and Detection of Gravitation Radiation", *Phys. Rev. D*, **34**, 984–990 (1986).
11. Strayer, D., and Yeh, N–C., private communication (1998).
12. Lipa, J.A., Swanson, D.R., Nissen, J.A., Geng, Z.K., Williamson, P.R., Stricker, D.R., Chui, T.C.P., Israelsson, U.E., and Larson, M., "The Specific Heat of Helium Confined to a 57–micron Planar Geometry near the Lambda Point", *Phys. Rev. Letts.*, **84**, 4894–4898 (2000).
13. Klemme, B.J., et.al., "PdMn and PdFe: New Materials for Temperature Measurement near 2K", *J. Low Temp. Phys.*, **116**, 133–146 (1999).
14. Nieuwenhuys, G.J., "Magnetic–Behavior of Cobalt, Iron and Manganese Dissolved in Palladium", *Adv. Phys.*, **24**, 515–591 (1975).

Space-Based Searches for Lorentz and CPT Violation ¹

Neil Russell

Physics Department, Northern Michigan University, Marquette, MI 49855, U.S.A.

email: nrussell@nmu.edu

In this talk, a summary is presented of recent research investigating ways in which high-precision atomic clocks on the International Space Station could search for violations of Lorentz and CPT symmetry. Space-based searches offer certain experimental advantages over Earth-based experiments investigating these symmetries. The results are based on work published in Physical Review Letters, volume 82, article 090801, 2002.

1. Introduction

This contribution to the proceedings of the 2002 NASA/JPL Workshop on Fundamental Physics in Space summarizes recent research [1] aimed at using atomic clocks and other apparatus on the International Space Station to search for violations of Lorentz and CPT symmetry at the Planck scale. We consider generalities relating to experiments mounted on spacecraft and consider some tests that could be performed using clocks planned for installation on the International Space Station (ISS). This work was done in collaboration with Robert Bluhm, Alan Kostelecký, and Charles Lane.

Lorentz symmetry is a feature of the standard model of particle physics. A considerable body of research exists investigating the possible violation of Lorentz symmetry, however. From the theoretical view, the motivation for this effort lies in discovering new physics beyond the standard model. From the experimental side, the rapidly improving sensitivities of various experiments may reveal previously unresolved effects. Recent theoretical work on Lorentz and CPT symmetry includes the development of a framework that allows for general minuscule violations of these symmetries in the context of particle physics. This framework is known as the standard-model extension [2].

Associated with the standard-model extension is a range of literature discussing a variety of theoretical issues, as well as a growing number of experimental results bounding possible effects. The violation of Lorentz symmetry [3] may arise in the context of string theory, and may be accompanied also by CPT violation [4]. Violation of Lorentz and CPT symmetry has also been discussed in the context of supersymmetry [5], and noncommutative field theory [6]. The standard-model extension is expected to be the low-energy limit of some fundamental underlying theory, and so the violations would most likely be suppressed by ratios involving the low-energy mass and the 10^{19} -GeV Planck mass. The broad applicability of the standard-model extension to all areas of physics is an attractive feature. Among the interesting implications is a possible mechanism for generating the baryon asymmetry in the universe [7]. For the neutral mesons, some bounds on standard-model extension parameters exist for the neutral K and D mesons, and results are anticipated for the neutral B system [8, 9, 10, 11]. In the photon sector, data from distant cosmological

¹Presented by Alan Kostelecký at the 2002 NASA/JPL Workshop for Fundamental Physics in Space, Dana Point, CA, May 2002.

sources places stringent bounds on Lorentz symmetry [2, 12, 13]. In the lepton sector, recent results have come from a muonium experiment, and from anomaly-frequency comparisons of oppositely-charged muons at CERN and BNL [14]. Earlier work considered electron-positron comparisons using Penning traps [15]. Impressive results are possible with a spin-polarized torsion pendulum [16].

Of particular relevance here are clock-comparison experiments with atoms and ions [17, 18, 19, 20]. Such experiments can identify spectral lines with resolutions at the Planck scale [21]. The general principle of a clock-comparison experiment is to search for violations of rotational symmetry by monitoring the frequency variations of a Zeeman hyperfine transition as the quantization axis changes direction. Usually, the frequencies of two different clocks are monitored as the laboratory rotates with the Earth. To avoid issues with signals travelling between two different locations, the clocks are co-located. Placing such an experiment in a satellite may produce results slightly better than have been achieved on earth, and this proceedings aims to consider some of the issues associated with this possibility.

2. Clocks and Inertial Frames

Atomic transitions can be measured with great precision and so are suitable candidates for time standards. In conventional physics with constant laboratory conditions, these clock frequencies are constant quantities. However, in the standard-model extension with Lorentz and CPT violation, some Zeeman hyperfine transitions are shifted in frequency [21]. For an experiment operating on such a transition, these shifts are controlled at leading order by parameters denoted in the clock reference frame as $\tilde{b}_3^w, \tilde{c}_q^w, \tilde{d}_3^w, \tilde{g}_d^w, \tilde{g}_q^w$. Here, the superscript w is p for the proton, n for the neutron, and e for the electron. These quantities are particular combinations of the basic coefficients $a_\mu^w, b_\mu^w, c_{\mu\nu}^w, d_{\mu\nu}^w, e_\mu^w, f_\mu^w, g_{\lambda\mu\nu}^w, H_{\mu\nu}^w$ appearing in the standard-model extension, and are related to expectation values in the underlying fundamental theory. For example,

$$\tilde{b}_3^w = b_3^w - m_w d_{30}^w + m_w g_{120}^w - H_{12}^w, \quad (1)$$

where m_w is the mass of the particle of type w and the subscripts are indices defined in a reference frame with the 3 direction defined as the clock quantization axis.

In the case of an Earth-based laboratory, the parameters $\tilde{b}_3^w, \tilde{c}_q^w, \tilde{d}_3^w, \tilde{g}_d^w, \tilde{g}_q^w$ are not fixed, but vary in time due to the sidereal rotation of the Earth with period $23\text{ h } 56\text{ min} \simeq 2\pi/\Omega$. The mathematical form of this time dependence can be found by considering the transformation from the laboratory frame containing the clock, with coordinates numbered $(0, 1, 2, 3)$, to a suitable nonrotating frame with coordinates (T, X, Y, Z) . Ideally, an inertial nonrotating frame is required, but for practical purposes any frame sufficiently inertial for the desired experimental sensitivity may be selected. Frames associated with the Earth, the Sun, the Milky Way galaxy, or the cosmic microwave background radiation would be possible choices for the inertial frame.

In earlier literature, the nonrelativistic transformation from the clock frame to the nonrotating frame has been considered [21]. In the case of space-based experiments, leading-order relativistic effects are of interest. An Earth-centered choice of reference frame must then be

rejected for such relativistic investigations because it is inertial over a limited time scale of perhaps a few days. Frames centered on the Sun, the galaxy, or the microwave background are approximately inertial over thousands of years, and are all acceptable for experiments. The choice of frame must be stated when reporting bounds on components of coefficients of Lorentz violation, since the numerical values will be frame-dependent.

A good choice of reference frame for our purposes is one centered on the Sun. So, we select the spatial origin on the Sun, the \hat{Z} unit vector parallel to the Earth's rotation axis, the \hat{X} unit vector in the equatorial plane pointing at the celestial vernal equinox, and \hat{Y} completing the right-handed system. The origin of the time variable T is taken to be the vernal equinox in the year 2000, using a clock located at the spatial origin. In this system, the Earth orbits about the Sun in a plane tilted at an angle of $\eta \simeq 23^\circ$ relative to the XY plane.

An adequate geometrical description of the orbital configuration can be obtained by approximating the Earth's orbit as a circular trajectory with angular frequency Ω_\oplus and speed β_\oplus . In addition, a satellite orbit about the Earth is approximated as circular with angular frequency ω_s and speed β_s . We use ζ to denote the angle between \hat{Z} and the axis of the satellite orbit. We denote by α the right ascension angle of the ascending node of the orbit. In the case of the ISS, α precesses by a few degrees per day.

Time intervals on a clock in a satellite are dilated when seen from the inertial Sun frame. Relative to the Sun-based frame, the clock velocity is $\vec{V}(T) = d\vec{X}/dT$, where the position vector $\vec{X}(T)$ of the clock is determined by positions of the Earth and the spacecraft. This vector $\vec{V}(T)$ is needed to obtain an accurate conversion between the times in the laboratory and in the Sun frame. In principle, effects such as perturbations in this vector and in the gravitational potential should be included in this description. In practice, these corrections may be neglected because the experiments involve comparing two clocks within the same satellite, which are essentially at the same location. In this case, standard relativity predicts identical rates of advance of the clocks. However, in the presence of Lorentz and CPT violation, clocks composed of different atomic species will be differently affected, despite being co-located.

Pertinent issues exist concerning the optimal orientation of the clock quantization axis relative to the geometric configuration of the system. If the clock apparatus is fixed within the satellite, the flight mode of the satellite will determine the clock quantization axis relative to the Sun frame. For this proceedings, we focus on a flight mode with quantization axis tangential to the circular satellite trajectory about the Earth. We choose the clock reference frame with 3 axis parallel to the satellite motion about the Earth, 1 axis pointing towards the center of the Earth, and 2 axis perpendicular to the satellite orbital plane. This configuration would be possible with some clock experiments on the ISS. The results outlined here are specific examples, but we note that other modes of flight and quantization-axis configurations can be handled by the methods discussed here. It is important to note that sensitivity to some components is only possible with specific quantization-axis orientations.

Experiments searching for Lorentz and CPT violation in the context of the standard-model extension are aimed at measuring the tensor-like parameters $a_\mu^w, b_\mu^w, c_{\mu\nu}^w, d_{\mu\nu}^w, e_\mu^w, f_\mu^w$,

$g_{\lambda\mu\nu}^w, H_{\mu\nu}^w$ in our standard solar reference frame. Measurements made in the laboratory frame must be transformed to the Sun-based frame by taking into account the relevant rotation and boost $\vec{V}(T)$. This means that the components of the coefficients for Lorentz violation in the clock frame must be expressed in terms of components in the Sun-based frame. To give an example, the transformation of the component b_3^w is

$$\begin{aligned}
b_3^w = & b_T^w \{ \beta_s - \beta_{\oplus} [\sin \Omega_{\oplus} T (\cos \alpha \sin \omega_s \Delta T \\
& + \cos \zeta \sin \alpha \cos \omega_s \Delta T) - \cos \eta \cos \Omega_{\oplus} T \\
& \times (\sin \alpha \sin \omega_s \Delta T - \cos \zeta \cos \alpha \cos \omega_s \Delta T) \\
& + \sin \eta \cos \Omega_{\oplus} T \sin \zeta \cos \omega_s \Delta T] \} \\
& - b_X^w (\cos \alpha \sin \omega_s \Delta T + \cos \zeta \sin \alpha \cos \omega_s \Delta T) \\
& - b_Y^w (\sin \alpha \sin \omega_s \Delta T - \cos \zeta \cos \alpha \cos \omega_s \Delta T) \\
& + b_Z^w \sin \zeta \cos \omega_s \Delta T,
\end{aligned} \tag{2}$$

where $\Delta T = T - T_0$ is the time interval measured from an agreed reference time T_0 . This transformation ignores effects such as the Thomas precession, holding only up to leading order in the velocities. The above result for b_3^w has to be included with the transformations for the other coefficients to get the full result for the observable parameter \tilde{b}_3^w in the Sun frame. The other coefficients \tilde{c}_q^w , \tilde{d}_3^w , \tilde{g}_a^w , and \tilde{g}_q^w are found by a similar method. The expressions that result depend on combinations of basic coefficients for Lorentz and CPT violation, on trigonometric functions of various angles, on frequency-time products, on β_{\oplus} , and on β_s .

3. Signal Features

Satellite-based experiments offer accessibility to all the spatial components of the basic coefficients for Lorentz and CPT violation. This eliminates a major constraint due to the fixed rotation axis for Earth-based experiments, preventing sensitivity to various spatial components. For instance, ground-based experiments sensitive to the laboratory-frame parameter \tilde{b}_3^w would in turn be sensitive only to the nonrotating-frame components $\tilde{b}_X^w, \tilde{b}_Y^w$. They can therefore bound only a limited subset of components of $b_{\mu}^w, d_{\mu\nu}^w, g_{\lambda\mu\nu}^w, H_{\mu\nu}^w$. This limitation would be overcome by a satellite platform. In the case of most satellites, the orbital axis is tilted relative to the Earth's rotation axis, and the orientation of this orbital axis precesses about the steady axis of the Earth. This precession makes the other spatial directions accessible to satellite tests.

Another attractive feature of the satellite platform for experiments is the relatively short orbital period. Since the satellite orbital period $2\pi/\omega_s$ for low-altitude satellites is much less than a sidereal day, data can be collected in a substantially reduced period. In the case of the ISS, the 92-minute orbital period translates into a data-collection period approximately 16 times shorter than on Earth, where the orbital period is about 24 hours. This could contribute to better results since it would reduce the sensitivity loss due to clock instabilities over time. One interesting advantage of this reduced experimental time is due to the fact that the Earth's velocity vector would remain essentially constant over the experimental

duration. This makes it possible to analyze the leading-order relativistic effects due to the speed $\beta_{\oplus} \simeq 1 \times 10^{-4}$ of the Earth relative to the Sun. Such tests are not possible with ground-based experiments, because they require several months of data, during which time the velocity of the Earth changes significantly. The analysis would be considerably simplified by the fact that the Earth could be regarded as an inertial reference frame. Direct extraction of leading-order relativistic effects would be possible.

The observations above show that many types of Lorentz and CPT violation that are unconstrained to date would be accessible in space-based experiments. As an example, consider a clock-comparison experiment with sensitivity to the observable \tilde{b}_3^w for particle species w . In the Sun-based frame and for each w , this observable is a linear combination of the basic coefficients $b_\mu^w, d_{\mu\nu}^w, g_{\lambda\mu\nu}^w, H_{\mu\nu}^w$ for Lorentz violation, numbering 35 independent observable components if the effect of field redefinitions is allowed for. Whereas a conventional ground-based experiment is sensitive to 8 of these, the same type of experiment mounted on a space platform would be sensitive to all 35. Another approach to overcoming constraints on accessible coefficients would be to construct a suitably-oriented rotating base for a ground-based experiment. This option is not pursued here, since the current work is aimed at understanding sensitivities of experiments planned for the ISS.

For ground-based experiments, some relativistic Lorentz and CPT coefficients are suppressed by the boost factor of the Earth, β_{\oplus} . In comparison, space-based clock-comparison experiments would also be sensitive to first-order relativistic effects proportional to the boost factor of the satellite, β_s . In Earth-based experiments, investigating the corresponding effects of the lab motion relative to the Earth's center would be impractical. Such effects would also be further suppressed by Ω/ω_s , which is about 6×10^{-2} in the case of the ISS.

A somewhat unexpected effect exists among the order- β_s corrections. It is found that in space-based experiments a dipole shift can lead to a potentially detectable signal with frequency $2\omega_s$. This is not seen in the nonrelativistic analysis of Earth-based clock-comparison experiments, where signals with the double frequency 2Ω occur only for quadrupole shifts. To better understand this, consider the parameter \tilde{b}_3^w , which nonrelativistically is the third component of a vector and would lead only to a signal with frequency ω_s . This parameter \tilde{b}_3^w contains the component d_{03} , however, which in a relativistic approach behaves like a two-tensor at leading order in β_s , and would therefore lead to a signal at frequency $2\omega_s$. We give an example: when the Earth is near the northern-summer solstice, \tilde{b}_3^w in the Sun-based frame has a double-frequency term that goes like $\cos(2\omega_s\Delta T)$ with coefficient C_2 containing the following spatial components of $d_{\mu\nu}^w$:

$$\begin{aligned}
C_2 \supset \beta_s \frac{m}{8} [& \cos 2\alpha (3 + \cos 2\zeta) (d_{XX}^w - d_{YY}^w) \\
& + (1 - \cos 2\zeta) (d_{XX}^w + d_{YY}^w - 2d_{ZZ}^w) \\
& - 2 \sin 2\zeta (\cos \alpha (d_{YZ}^w + d_{ZY}^w) - \sin \alpha (d_{ZX}^w + d_{XZ}^w)) \\
& + (3 + \cos 2\zeta) \sin 2\alpha (d_{XY}^w + d_{YX}^w)].
\end{aligned} \tag{3}$$

This shows that all observable spatial components of $d_{\mu\nu}^w$ could be accessed through appropriate monitoring of the 2ω frequency.

3. Experiments on Earth Satellites

The ISS will house a number of high-precision clocks and other oscillators capable of testing fundamental physics in the coming years. Instruments slated for installation include H masers, laser-cooled Cs and Rb clocks, and superconducting microwave cavity oscillators [22, 23, 24, 25]. Among the experimental advantages of the ISS are the orbital parameters $\beta_s \simeq 3 \times 10^{-5}$ and $\zeta \simeq 52^\circ$, which correspond to a speed and orbital plane outside the scope of Earth-based experiments. In addition, experiments on the ISS would be conducted in a microgravity environment with reduced environmental disturbances, and these features are expected to lead to sensitivity gains compared with ground-based clocks. The analysis presented in this proceedings is valid for tests with all these clocks, but not for the oscillators, which are discussed elsewhere [13].

In our discussion, we consider a canonical configuration with a signal clock being compared to a co-located reference clock. The signal clock is sensitive to leading-order Lorentz and CPT violation, while the reference clock, for example an H maser tuned to its clock transition $|1, 0\rangle \rightarrow |0, 0\rangle$, is insensitive to such effects.

Hydrogen Masers

A hydrogen maser operating on the transition $|1, \pm 1\rangle \rightarrow |1, 0\rangle$ would be one possible signal clock. A recent ground-based experiment used a double-resonance technique to monitor this transition frequency [20], which is sensitive to the parameters \tilde{b}_3^p and \tilde{b}_3^e in the clock frame. The sensitivity to relatively clean parameter combinations is a consequence of the simplicity of the hydrogen system as compared with atoms such as Rb or Cs used in atomic clocks. Mounting this experiment on the ISS would mean that an experimental run of only about a day would suffice to obtain data roughly equivalent to four months of data taken on Earth with a similar experiment on a fixed base. For both $w = e$ and $w = p$, all spatial components of b_μ^w , $m_w d_{\mu\nu}^w$, $m_w g_{\lambda\mu\nu}^w$, $H_{\mu\nu}^w$ could be sampled by exploiting the orbital inclination ($\zeta \neq 0$) and by repeating the experiment at a later time when orbital precession corresponds to a significantly different value of α . Making the assumption of a 500 μHz sensitivity, equalling that attained in Earth-based experiments, several presently unbounded components would be probed at the level of about 10^{-27} GeV, and others at about 10^{-23} GeV. We also estimate that cleaner bounds on certain spatial components of $m_w d_{\mu\nu}^w$, $m_w g_{\lambda\mu\nu}^w$ at the level of about 10^{-23} GeV could be obtained by searching for a signal at the double frequency $2\omega_s$. In all, about 50 components of coefficients for Lorentz and CPT violation that are currently unbounded could be tested at the Planck scale.

Cesium Clocks

In the case of a laser-cooled ^{133}Cs clock, a reference frequency could be provided by the usual clock transition $|4, 0\rangle \rightarrow |3, 0\rangle$, which is insensitive to Lorentz and CPT violation. A Zeeman hyperfine transition such as $|4, 4\rangle \rightarrow |4, 3\rangle$ would be needed to provide a signal. Since ^{133}Cs has an unpaired electron, this atom has sensitivity to electron parameters similar to that of the H maser. In the Schmidt model, the ^{133}Cs nucleus is a proton with angular momentum

7/2, giving sensitivity to all clock-frame parameters $\tilde{b}_3^p, \tilde{c}_q^p, \tilde{d}_3^p, \tilde{g}_d^p, \tilde{g}_q^p$, and yielding both dipole and quadrupole shifts. We note that components tested would include $c_{\mu\nu}^p$. Repeating results achieved in an Earth-based experiment would imply a sensitivity level of about 50 μHz [18] on the $|4, 4\rangle \rightarrow |4, 3\rangle$ transition. A similar experiment on the ISS would potentially run for a period reduced by a factor of 16. Furthermore, measurements of the double-frequency signal $2\omega_s$ would probe the spatial components of $c_{\mu\nu}^p$ at the 10^{-25} level, and other components at about the 10^{-21} level. We estimate that about 60 components of coefficients for Lorentz and CPT violation would be accessible at the Planck-scale.

Rubidium Clocks

Experiments with ^{87}Rb are similar in many ways to ones with ^{133}Cs . The clock transition $|2, 0\rangle \rightarrow |1, 0\rangle$, is insensitive to Lorentz and CPT violation, and so is a suitable reference signal. A Zeeman hyperfine transition such as $|2, 1\rangle \rightarrow |2, 0\rangle$ is a potential signal transition. Like H and ^{133}Cs , ^{87}Rb has an unpaired electron, and is therefore sensitive to similar electron parameters as discussed for those systems. The sensitivity to proton parameters is also similar to that for ^{133}Cs , up to factors of order unity, because the Schmidt nucleon for ^{87}Rb is a proton with angular momentum 3/2. An advantage from the theoretical viewpoint is the magic neutron number, which aids in calculational reliability and leads to cleaner results [21]. A considerable range of Lorentz and CPT bounds could be envisaged for ^{87}Rb with ideas along these lines.

Other Spacecraft

Lorentz and CPT tests could be done with on a variety of space platforms. Missions where the speeds of the craft with respect to the Sun are larger than the speed β_s for Earth-orbiting satellites are of particular interest. One possibility is the proposed SpaceTime [26] experiment, which would attain $\beta \simeq 10^{-3}$ on a trajectory sweeping from Jupiter in towards the Sun. This mission will fly $^{111}\text{Cd}^+$, $^{199}\text{Hg}^+$, and $^{171}\text{Yb}^+$ ion clocks in a craft rotating several times per minute. This rotation rate would offer the possibility of gathering data for a Lorentz and CPT test in as little as 15 minutes. The clock transitions $|1, 0\rangle \rightarrow |0, 0\rangle$ are insensitive to Lorentz and CPT violation for all three clocks, and so could be used as reference signals. Zeeman hyperfine transitions such as $|1, 1\rangle \rightarrow |1, 0\rangle$ are sensitive to Lorentz- and CPT-violating effects in the standard-model extension and could provide signal clocks. In the context of the Schmidt model, all three clocks are sensitive to the neutron parameters $\tilde{b}_3^n, \tilde{d}_3^n, \tilde{g}_d^n$ in the clock frame. Such experiments would be of particular interest because none of the above neutron parameters can be probed with the proposed ISS experiments. Several tests for Lorentz and CPT violation would be possible by seeking variations in the signal-clock outputs at the spacecraft rotation frequency ω_{ST} and also at $2\omega_{ST}$. Experiments in this category would gain an order of magnitude advantage over Earth-based or Earth-orbit experiments because of their larger boost factors.

4. Discussion

The standard-model extension is a microscopic theory predicting possible minuscule Lorentz-

and CPT-violating effects in physical systems. Some of the experimental challenges facing measurements of such effects can be overcome by mounting experiments on satellites orbiting the Earth. In particular, atomic clocks planned for the International Space Station will be able to exploit the relatively high rotation rates of the ISS as well as the relatively high speed relative to the Earth to gain sensitivity to relativistic effects within the context of the standard-model extension. Other experiments of interest in this context include satellite-mounted microwave oscillators.

5. Acknowledgments

I thank Robert Bluhm, Alan Kostelecký, and Chuck Lane for their collaboration on this work. This work was partially supported by a grant from Northern Michigan University.

References

1. R. Bluhm *et al.*, Phys. Rev. Lett. **88**, 090801 (2002).
2. D. Colladay and V.A. Kostelecký, Phys. Rev. D **55**, 6760 (1997); **58**, 116002 (1998); Phys. Lett. B **511**, 209 (2001); V.A. Kostelecký and R. Lehnert, Phys. Rev. D **63**, 065008 (2001).
3. For a broad overview of Lorentz and CPT symmetry issues, see, for example, V.A. Kostelecký, ed., *CPT and Lorentz Symmetry II*, World Scientific, Singapore, 2002.
4. V.A. Kostelecký and S. Samuel, Phys. Rev. D **39**, 683 (1989); **40**, 1886 (1989); Phys. Rev. Lett. **63**, 224 (1989); **66**, 1811 (1991); V.A. Kostelecký and R. Potting, Nucl. Phys. B **359**, 545 (1991); Phys. Lett. B **381**, 89 (1996); Phys. Rev. D **63**, 046007 (2001); V.A. Kostelecký, M. Perry, and R. Potting, Phys. Rev. Lett. **84**, 4541 (2000).
5. M.S. Berger and V.A. Kostelecký, Phys. Rev. D **65**, 091701(R) (2002).
6. S.M. Carroll *et al.*, Phys. Rev. Lett. **87**, 141601 (2001); Z. Guralnik *et al.*, Phys. Lett. B **517** 450 (2001); A. Anisimov *et al.*, Phys. Rev. D **65**, 085032 (2002).
7. O. Bertolami *et al.*, Phys. Lett. B **395**, 178 (1997).
8. KTeV Collaboration, Y.B. Hsiung *et al.*, Nucl. Phys. Proc. Suppl. **86**, 312 (2000).
9. V.A. Kostelecký, Phys. Rev. Lett. **80**, 1818 (1998); Phys. Rev. D **61**, 016002 (2000); **64**, 076001 (2001).
10. OPAL Collaboration, R. Ackerstaff *et al.*, Z. Phys. C **76**, 401 (1997); DELPHI Collaboration, M. Feindt *et al.*, preprint DELPHI 97-98 CONF 80 (1997); BELLE Collaboration, K. Abe *et al.*, Phys. Rev. Lett. **86**, 3228 (2001).
11. V.A. Kostelecký and R. Potting, Phys. Rev. D **51**, 3923 (1995); D. Colladay and V.A. Kostelecký, Phys. Lett. B **344**, 259 (1995); Phys. Rev. D **52**, 6224 (1995); V.A. Kostelecký and R. Van Kooten, Phys. Rev. D **54**, 5585 (1996); N. Isgur *et al.*, Phys. Lett. B **515**, 333 (2001).
12. S.M. Carroll, G.B. Field, and R. Jackiw, Phys. Rev. D **41**, 1231 (1990); R. Jackiw and V.A. Kostelecký, Phys. Rev. Lett. **82**, 3572 (1999).

13. V.A. Kostelecký and M. Mewes, Phys. Rev. Lett. **87**, 251304 (2001); preprint IUHET 449 (hep-ph/0205211).
14. V.W. Hughes *et al.*, Phys. Rev. Lett. **87**, 111804 (2001); R. Bluhm *et al.*, Phys. Rev. Lett. **84**, 1098 (2000).
15. H. Dehmelt *et al.*, Phys. Rev. Lett. **83**, 4694 (1999); R. Mittleman *et al.*, Phys. Rev. Lett. **83**, 2116 (1999); G. Gabrielse *et al.*, Phys. Rev. Lett. **82**, 3198 (1999); R. Bluhm *et al.*, Phys. Rev. Lett. **82**, 2254 (1999); Phys. Rev. Lett. **79**, 1432 (1997); Phys. Rev. D **57**, 3932 (1998).
16. B. Heckel *et al.*, in B.N. Kursunoglu *et al.*, eds., *Elementary Particles and Gravitation*, Plenum, New York, 1999; R. Bluhm and V.A. Kostelecký, Phys. Rev. Lett. **84**, 1381 (2000).
17. V.W. Hughes, H.G. Robinson, and V. Beltran-Lopez, Phys. Rev. Lett. **4** (1960) 342; R.W.P. Drever, Philos. Mag. **6** (1961) 683; J.D. Prestage *et al.*, Phys. Rev. Lett. **54** (1985) 2387; S.K. Lamoreaux *et al.*, Phys. Rev. A **39** (1989) 1082; T.E. Chupp *et al.*, Phys. Rev. Lett. **63** (1989) 1541.
18. C.J. Berglund *et al.*, Phys. Rev. Lett. **75** (1995) 1879; L.R. Hunter *et al.*, in V.A. Kostelecký, ed., *CPT and Lorentz Symmetry*, World Scientific, Singapore, 1999.
19. D. Bear *et al.*, Phys. Rev. Lett. **85**, 5038 (2000).
20. D.F. Phillips *et al.*, Phys. Rev. D **63**, 111101 (2001); M.A. Humphrey *et al.*, physics/0103068; Phys. Rev. A **62**, 063405 (2000).
21. V.A. Kostelecký and C.D. Lane, Phys. Rev. D **60**, 116010 (1999); J. Math. Phys. **40**, 6245 (1999).
22. N. Ashby, presented at the 2nd Pan Pacific Basin Workshop on Microgravity Science, Pasadena, January 2001.
23. P. Laurent *et al.*, Eur. Phys. J. D **3** (1998) 201.
24. C. Fertig *et al.*, presented at the Workshop on Fundamental Physics in Space, Solvang, June 2000.
25. S. Buchman *et al.*, Adv. Space Res. **25**, 1251 (2000).
26. L. Maleki and J.D. Prestage, in C. Lämmerzahl *et al.*, eds., *Testing Relativistic Gravity in Space: Gyroscopes, Clocks, Interferometers*, Springer-Verlag, Berlin, 2001.

Precision Studies of Relativity in Electrodynamics ¹

Matthew Mewes

Physics Department, Indiana University, Bloomington, IN 47405, U.S.A.

email: mmewes@indiana.edu

In this contribution to the proceedings of the 2002 Workshop for Fundamental Physics in Space, a discussion of recent work on astrophysical and laboratory tests of Lorentz symmetry in electrodynamics is presented. Stringent constraints are placed on birefringence of light emitted from galactic and extragalactic sources. The prospect of precision clock-comparison experiments utilizing resonant cavities are considered.

1. Introduction

In the past, high-precision tests of the properties of light have played an important role in the search for new physics. Historically, testing the Lorentz invariance of light has confirmed special relativity to a high degree of precision [1, 2, 3]. Many of the traditional experiments fit into one of two categories. Michelson-Morley experiments are designed to test rotational invariance by searching for anisotropy in the speed of light. Kennedy-Thorndike experiments test boost invariance by searching for variations in the speed of light due to changes in the velocity of the laboratory. In this work, I review a recent study of extremely precise tests of Lorentz symmetry in electrodynamics. This research was done in collaboration with Alan Kostelecký. A detailed discussion can be found in Ref. [4].

In recent years, the possibility that Planck scale physics may reveal itself at low energies as small Lorentz violations has lead to the development of a general Lorentz-violating standard-model extension [5, 6, 7]. It consists of the minimal standard model plus small Lorentz- and CPT-violating terms. The small violations may originate from nonzero vacuum expectation values of Lorentz tensors in the underlying theory [8]. Lorentz violations of this type also arise from noncommutative field theories [9].

The extension has provided a theoretical framework for a number of high precision tests of Lorentz symmetry. To date, experiments involving hadrons [10, 11, 12, 13, 14, 15], protons and neutrons [16, 17, 18, 19, 20], electrons [21, 22], photons [4, 23], and muons [24] have been performed.

A Lorentz-violating extended electrodynamics can be extracted from the standard-model extension [5]. In this work, we consider some experimental consequences of the extended electrodynamics. The theory predicts novel features which lead to sensitive tests of Lorentz symmetry. One unconventional property is the birefringence of light. The observed absence of birefringence of light emitted from distant sources leads to tight bounds on some of the coefficients for Lorentz violation [4, 23]. Some of these bounds are discussed in Sec. 3.

Another observable consequence of Lorentz violation is an orientation and velocity dependence in the frequencies of resonant cavities. This dependence provides the basis for future clock-comparison experiments sensitive to the photon-sector of the standard-model

¹Presented at 2002 NASA/JPL Workshop for Fundamental Physics in Space, Dana Point, California, May, 2002.

extension. Past clock-comparison experiments have been used to place constraints on the fermion sector [16, 17, 18, 19, 20]. Space-based versions of these experiments have recently been considered for precision tests of Lorentz symmetry on board the International Space Station (ISS) and other spacecraft [25]. Tests for Lorentz violation using resonant cavities are considered in Sec. 4.

2. Extended Electrodynamics

The photon sector of the standard-model extension yields a Lorentz-violating electrodynamics. It maintains the usual gauge invariance and is covariant under observer Lorentz transformations. The Lorentz-violating electrodynamics includes both CPT-even and -odd terms. However, the CPT-odd terms are theoretically undesirable since they may lead to instabilities [5, 26]. Furthermore, these terms have been bounded experimentally to extremely high precision using polarization measurements of distant radio galaxies [23]. Neglecting the CPT-odd terms, we are left with a CPT-conserving electrodynamics including small Lorentz violations.

The CPT-even lagrangian associated with the Lorentz-violating electrodynamics is [5]

$$\mathcal{L} = -\frac{1}{4}F_{\mu\nu}F^{\mu\nu} - \frac{1}{4}(k_F)_{\kappa\lambda\mu\nu}F^{\kappa\lambda}F^{\mu\nu} , \quad (1)$$

where $F_{\mu\nu}$ is the field strength, $F_{\mu\nu} \equiv \partial_\mu A_\nu - \partial_\nu A_\mu$. The first term is the usual Maxwell lagrangian. The second is an unconventional Lorentz-violating term. The coefficient for Lorentz violation, $(k_F)_{\kappa\lambda\mu\nu}$, is real and comprised of 19 independent components. The absence of observed Lorentz violation requires $(k_F)_{\kappa\lambda\mu\nu}$ to be small.

It is often convenient to work with the electric and magnetic fields, \vec{E} and \vec{B} , rather than the vector potential A^μ . In terms of the usual electric and magnetic fields, the lagrangian takes the form

$$\mathcal{L} = \frac{1}{2}(\vec{E}^2 - \vec{B}^2) + \frac{1}{2}\vec{E} \cdot (\kappa_{DE}) \cdot \vec{E} - \frac{1}{2}\vec{B} \cdot (\kappa_{HB}) \cdot \vec{B} + \vec{E} \cdot (\kappa_{DB}) \cdot \vec{B} . \quad (2)$$

The real 3×3 matrices κ_{DE} , κ_{HB} and κ_{DB} contain the same information as $(k_F)_{\kappa\lambda\mu\nu}$. The relationship between the two notations can be found in Ref. [4]. Taking $\kappa_{DE} = \kappa_{HB} = \kappa_{DB} = 0$ in Eq. (2) results in the usual Maxwell lagrangian in terms of \vec{E} and \vec{B} . The parity-even matrices, κ_{DE} and κ_{HB} , are symmetric, while the parity-odd matrix, κ_{DB} , has both symmetric and antisymmetric parts. The matrices $(\kappa_{DE} + \kappa_{HB})$ and κ_{DB} are traceless. These symmetries leave 11 parity-even and 8 parity-odd independent components.

The equations of motion for this lagrangian are

$$\partial_\alpha F_\mu{}^\alpha + (k_F)_{\mu\alpha\beta\gamma}\partial^\alpha F^{\beta\gamma} = 0 . \quad (3)$$

These constitute modified source-free inhomogeneous Maxwell equations. The homogeneous Maxwell equations,

$$\partial_\mu \tilde{F}^{\mu\nu} \equiv \frac{1}{2}\epsilon^{\mu\nu\kappa\lambda}\partial_\mu F_{\kappa\lambda} = 0 , \quad (4)$$

remain unchanged.

An interesting analogy exists between this theory and the usual situation in anisotropic media. Define fields \vec{D} and \vec{H} by the six-dimensional matrix equation

$$\begin{pmatrix} \vec{D} \\ \vec{H} \end{pmatrix} = \begin{pmatrix} 1 + \kappa_{DE} & \kappa_{DB} \\ \kappa_{HE} & 1 + \kappa_{HB} \end{pmatrix} \begin{pmatrix} \vec{E} \\ \vec{B} \end{pmatrix}, \quad (5)$$

with $\kappa_{HE} = -(\kappa_{DB})^T$. Then the modified Maxwell equations take the familiar form

$$\begin{aligned} \vec{\nabla} \times \vec{H} - \partial_0 \vec{D} &= 0, & \vec{\nabla} \cdot \vec{D} &= 0, \\ \vec{\nabla} \times \vec{E} + \partial_0 \vec{B} &= 0, & \vec{\nabla} \cdot \vec{B} &= 0. \end{aligned} \quad (6)$$

As a result, the behavior of electromagnetic fields in the extended electrodynamics is very similar to that of conventional fields in anisotropic media.

For the purpose of comparing the sensitivity of various experiments, it is convenient to make the decomposition into four 3×3 traceless matrices

$$\begin{aligned} (\tilde{\kappa}_{e+})^{jk} &= \frac{1}{2}(\kappa_{DE} + \kappa_{HB})^{jk}, & (\tilde{\kappa}_{e-})^{jk} &= \frac{1}{2}(\kappa_{DE} - \kappa_{HB})^{jk} - \frac{1}{3}\delta^{jk}(\kappa_{DE})^l{}_l, \\ (\tilde{\kappa}_{o+})^{jk} &= \frac{1}{2}(\kappa_{DB} + \kappa_{HE})^{jk}, & (\tilde{\kappa}_{o-})^{jk} &= \frac{1}{2}(\kappa_{DB} - \kappa_{HE})^{jk}, \end{aligned} \quad (7)$$

and a single rotationally symmetric trace component

$$\tilde{\kappa}_{\text{tr}} = \frac{1}{3}(\kappa_{DE})^l{}_l. \quad (8)$$

The matrices $\tilde{\kappa}_{e+}$ and $\tilde{\kappa}_{e-}$ and the single coefficient $\tilde{\kappa}_{\text{tr}}$ contain the parity-even coefficients, while the matrices $\tilde{\kappa}_{o+}$ and $\tilde{\kappa}_{o-}$ contain the parity-odd. The matrix $\tilde{\kappa}_{o+}$ is antisymmetric while the other three are symmetric.

In terms of this decomposition, the lagrangian is

$$\begin{aligned} \mathcal{L} &= \frac{1}{2}[(1 + \tilde{\kappa}_{\text{tr}})\vec{E}^2 - (1 - \tilde{\kappa}_{\text{tr}})\vec{B}^2] + \frac{1}{2}\vec{E} \cdot (\tilde{\kappa}_{e+} + \tilde{\kappa}_{e-}) \cdot \vec{E} \\ &\quad - \frac{1}{2}\vec{B} \cdot (\tilde{\kappa}_{e+} - \tilde{\kappa}_{e-}) \cdot \vec{B} + \vec{E} \cdot (\tilde{\kappa}_{o+} + \tilde{\kappa}_{o-}) \cdot \vec{B}. \end{aligned} \quad (9)$$

From the form of Eq. (9), it is evident that the component $\tilde{\kappa}_{\text{tr}}$ corresponds to shift in the effective permittivity ϵ and effective permeability μ by $(\epsilon - 1) = -(\mu^{-1} - 1) = \tilde{\kappa}_{\text{tr}}$. Therefore, the effect of a nonzero $\tilde{\kappa}_{\text{tr}}$ is an overall shift in the speed of light. This result generalizes to the nine independent coefficients in $\tilde{\kappa}_{\text{tr}}$, $\tilde{\kappa}_{e-}$ and $\tilde{\kappa}_{o+}$. To leading order, these can be viewed as a distortion of the spacetime metric of the form $\eta^{\mu\nu} \rightarrow \eta^{\mu\nu} + k^{\mu\nu}$, where $k^{\mu\nu}$ is small, real and symmetric.

Small distortions of this type are normally unphysical, since they can be eliminated through coordinate transformations and field redefinitions. However, in the context of the full standard-model extension, eliminating these terms from the photon sector will alter other sectors and the effects of such terms can not be removed. Thus, in experiments where the properties of light are compared to the properties of other matter, these terms are relevant. While in experiments sensitive to the properties of light only, these nine coefficients are

not expected to appear. The resonant-cavity based experiments discussed in Sec. 4 fall into the first category, while the astrophysical tests of Sec. 3 belong to the second. The tests discussed in Sec. 3 rely on measurements of birefringence, which in essence compares the properties of light with different polarizations. Therefore, these tests are only sensitive to the ten independent components of $\tilde{\kappa}_{e+}$ and $\tilde{\kappa}_{o-}$.

When reporting bounds on birefringence it is convenient to express them in terms of a ten-dimensional vector k^a containing the ten independent components of $\tilde{\kappa}_{e+}$ and $\tilde{\kappa}_{o-}$ [4]. The relationship between $\tilde{\kappa}_{e+}$, $\tilde{\kappa}_{o-}$ and k^a is given by

$$\begin{aligned} (\tilde{\kappa}_{e+})^{jk} &= - \begin{pmatrix} -(k^3 + k^4) & k^5 & k^6 \\ k^5 & k^3 & k^7 \\ k^6 & k^7 & k^4 \end{pmatrix} , \\ (\tilde{\kappa}_{o-})^{jk} &= \begin{pmatrix} 2k^2 & -k^9 & k^8 \\ -k^9 & -2k^1 & k^{10} \\ k^8 & k^{10} & 2(k^1 - k^2) \end{pmatrix} . \end{aligned} \quad (10)$$

Bounds can then be expressed in terms of $|k^a| \equiv \sqrt{k^a k^a}$, the magnitude of the vector k^a .

3. Astrophysical Tests

In order to understand the effects of Lorentz violation on the propagation of light, we begin by considering plane-wave solutions. Adopting the ansatz $F_{\mu\nu}(x) = F_{\mu\nu} e^{-ip_\alpha x^\alpha}$, the modified Maxwell equations yield an Ampère law given by the linear equation

$$(-\delta^{jk} p^2 - p^j p^k - 2(k_F)^{j\beta\gamma k} p_\beta p_\gamma) E^k = 0 . \quad (11)$$

Solving this equation determines the dispersion relation

$$p_\pm^0 = (1 + \rho \pm \sigma) |\vec{p}| , \quad (12)$$

and electric field

$$\vec{E}_\pm \propto (\sin \xi, \pm 1 - \cos \xi, 0) + O(k_F) . \quad (13)$$

To leading order, the quantities ρ , $\sigma \sin \xi$ and $\sigma \cos \xi$ are linear combinations of $(k_F)_{\kappa\lambda\mu\nu}$ and depend on \hat{v} , the direction of propagation. One unconventional feature of these solutions is the birefringence of light in the absence of matter. In the conventional case, this behavior is commonly found in the presence of anisotropic media.

The general vacuum solution is a linear combination of the \vec{E}_+ and \vec{E}_- . For nonzero σ , these solutions obey different dispersion relations. As a result, they propagate at slightly different velocities. At leading order, the difference in the velocities is given by

$$\Delta v \equiv v_+ - v_- = 2\sigma . \quad (14)$$

For light propagating over astrophysical distances, this tiny difference may become apparent.

As can be seen from the above solutions, birefringence depends on the linear combination $\sigma \sin \xi$ and $\sigma \cos \xi$. As expected, these only contain the ten independent coefficients which

appear in $\tilde{\kappa}_{e+}$ and $\tilde{\kappa}_{o-}$. Expressions for $\sigma \sin \xi$ and $\sigma \cos \xi$ in terms of these ten independent coefficients and the direction of propagation can be found in the literature [4].

Next, we consider two observable effects stemming from the birefringence. The first is the difference in arrival time of two modes in unpolarized light. The second is the change in polarization of polarized light emitted from distant sources.

3.1. Pulse Dispersion

For a source producing relatively unpolarized light, the components \vec{E}_{\pm} associated with each mode will be comparable. For light produced at a given instant, the difference in velocity will induce a difference in the observed arrival time of the two modes given by $\Delta t \simeq \Delta v L$, where L is the distance to the source.

To make use of this idea, we consider sources that produce radiation with rapidly changing time structure. Sources producing narrow pulses of radiation such as pulsars and gamma-ray bursts are ideal. For sources of this type, the pulse can be regarded as the superposition of two independent pulses, one for each mode. As the pulse propagates, the difference in velocity will cause the two pulses to separate. A signal for Lorentz violation would manifest itself as the observation of two sequential pulses of similar structure. The pulses would be linearly polarized at mutually orthogonal polarization angles. This type of double pulse has not yet been observed.

Single pulse measurements can be used to place bounds on Lorentz violation. Suppose a source produces a pulse with a characteristic width w_s . As the pulse propagates, the

Source	L		w_o	
GRB 971214 [27, 28]	2.2	Gpc	50	s
GRB 990123 [28, 29]	1.9	Gpc	100	s
GRB 980329 [28, 30]	2.3	Gpc	50	s
GRB 990510 [28, 31]	1.9	Gpc	100	s
GRB 000301C [32, 33]	2.0	Gpc	10	s
PSR J1959+2048 [34]	1.5	kpc	64	μ s
PSR J1939+2134 [34]	3.6	kpc	190	μ s
PSR J1824-2452 [34]	5.5	kpc	300	μ s
PSR J2129+1210E [34]	10.0	kpc	1.4	ms
PSR J1748-2446A [34]	7.1	kpc	1.3	ms
PSR J1312+1810 [34]	19.0	kpc	4.4	ms
PSR J0613-0200 [34]	2.2	kpc	1.4	ms
PSR J1045-4509 [34]	3.2	kpc	2.2	ms
PSR J0534+2200 [34, 35]	2.0	kpc	10	μ s
PSR J1939+2134 [34, 36]	3.6	kpc	5	μ s

Table 1: Source data for velocity constraints.

two modes spread apart and the width of the pulse will increase. The observed width can be estimated as $w_o \simeq w_s + \Delta t$. Therefore, observations of w_o place conservative bounds on $\Delta t \simeq \Delta v L \simeq 2\sigma L$. The resulting bound on σ constrains the ten-dimensional parameter space of $\tilde{\kappa}_{e+}$ and $\tilde{\kappa}_{o-}$. Since a single source constrains only one degree of freedom, a minimum of ten sources located at different positions on the sky are required to fully constrain the ten coefficients.

Table 1 lists a sample of 16 sources consisting of gamma-ray bursts and pulsars, as well as their distances and pulse widths. Each width places a bound on σ for that particular source. Combining these bounds using a method described in Ref. [4] constrains the ten-dimensional parameter space. At the 90% confidence level, we obtain a bound of $|k^a| < 3 \times 10^{-16}$ on the coefficients for Lorentz violation.

3.2. Spectropolarimetry

In this subsection, we consider the effect of Lorentz violation on polarized light. Decomposing a general electric field into its birefringent components, we write

$$\vec{E}(x) = (\vec{E}_+ e^{-ip_+^0 t} + \vec{E}_- e^{-ip_-^0 t}) e^{i\vec{p} \cdot \vec{x}}. \quad (15)$$

Each of the components propagates with different phase velocity. A change in the relative phase results from this difference. The shift in relative phase is given by

$$\Delta\phi = (p_+^0 - p_-^0)t \simeq 4\pi\sigma L/\lambda, \quad (16)$$

where L is the distance to the source and λ is the wavelength of the light. The change in relative phase results in a change in the polarization as the radiation propagates.

The L/λ dependence suggests the effect is larger for more distant sources and shorter wavelengths. Recent spectropolarimetry of distant galaxies at wavelengths ranging from infrared to ultraviolet has made it possible to achieve values of L/λ greater than 10^{31} . Measured polarization parameters are typically order 1. Therefore, we expect an experimental sensitivity of 10^{-31} or better to components of $(k_F)_{\kappa\lambda\mu\nu}$.

In general, plane waves are elliptically polarized. The polarization ellipse can be parameterized with angles ψ , which characterizes the orientation of the ellipse, and $\chi = \pm \arctan \frac{\text{minor axis}}{\text{major axis}}$, which describes the shape of the ellipse and helicity of the wave. The phase change, $\Delta\phi$, results in a change in both ψ and χ . However, measurements of χ are not commonly found in the literature. Focusing our attention on ψ , we seek an expression for $\delta\psi = \psi - \psi_0$, the difference between ψ at two wavelengths, λ and λ_0 . We find [4]

$$\delta\psi = \frac{1}{2} \tan^{-1} \frac{\sin \tilde{\xi} \cos \zeta_0 + \cos \tilde{\xi} \sin \zeta_0 \cos(\delta\phi - \phi_0)}{\cos \tilde{\xi} \cos \zeta_0 - \sin \tilde{\xi} \sin \zeta_0 \cos(\delta\phi - \phi_0)}, \quad (17)$$

where we have defined $\delta\phi = 4\pi\sigma(L/\lambda - L/\lambda_0)$, $\tilde{\xi} = \xi - 2\psi_0$ and $\phi_0 \equiv \tan^{-1}(\tan 2\chi_0 / \sin \tilde{\xi})$, $\zeta_0 \equiv \cos^{-1}(\cos 2\chi_0 \cos \tilde{\xi})$. The polarization at λ_0 is given by the polarization angles ψ_0 and χ_0 .

Source	L_{eff} (Gpc)	$10^{30}L_{eff}/\lambda$	$\log_{10} \sigma$
IC 5063 [37]	0.04	0.56 - 2.8	-30.8
3A 0557-383 [38]	0.12	2.2 - 8.5	-31.2
IRAS 18325-5925 [38]	0.07	1.0 - 4.9	-31.0
IRAS 19580-1818 [38]	0.14	1.8 - 9.3	-31.0
3C 324 [39]	2.44	82 - 180	-32.3
3C 256 [40]	3.04	110 - 220	-32.4
3C 356 [41]	2.30	78 - 170	-32.3
F J084044.5+363328 [42]	2.49	88 - 170	-32.4
F J155633.8+351758 [42]	2.75	99 - 160	-32.4
3CR 68.1 [43]	2.48	84 - 180	-32.4
QSO J2359-1241 [44]	2.01	110 - 120	-31.2
3C 234 [45]	0.61	55 - 81	-31.7
4C 40.36 [46]	3.35	120 - 260	-32.4
4C 48.48 [46]	3.40	120 - 260	-32.4
IAU 0211-122 [46]	3.40	120 - 260	-32.4
IAU 0828+193 [46]	3.53	130 - 270	-32.4

Table 2: Source data for polarization constraints.

The idea is to fit existing spectropolarimetric data to Eq. (17). Under the reasonable assumption that the polarization of the light when emitted is relatively constant over the relevant wavelengths, any measured wavelength dependence in the polarization is due to Lorentz violation.

Table 2 lists 16 sources with published polarimetric data with wavelengths ranging from 400 to 2200 nm. In this table, the effective distance L_{eff} is listed which takes cosmological redshift of the light into account. Using a fitting procedure described in Ref. [4], we obtain a bound on σ for each source. Combining these bounds in the same manner as in the pulse-dispersion case, a constraint on the ten-dimensional parameter space is found. At the 90% confidence level, we obtain a bound of $|k^a| < 2 \times 10^{-32}$ on the coefficients for Lorentz violation responsible for birefringence.

4. Resonant Cavities

Clock-comparison experiments have proved to be some of the most sensitive tests of Lorentz symmetry [16, 17, 18, 19, 20]. The frequencies of these clocks are typically atomic Zeeman transitions. Lorentz violation causes these frequencies to vary with changes in orientation or velocity of the clock. Experiments searching for a variation due to the rotational motion of the Earth have placed stringent bounds on Lorentz violation in the fermion sectors of the standard-model extension.

Modern versions of the Michelson-Morley and Kennedy-Thorndike experiments utilize

resonating electromagnetic cavities [47, 48, 49]. Resonant cavities serve as clocks in clock-comparison experiments which are sensitive to Lorentz violation in the photon sector. These experiments search for a variation in the resonant frequency of a cavity as its orientation or velocity changes. For a typical Earth-based experiment, the variation in resonant frequency occurs at harmonics of the Earth's sidereal frequency, $\omega_{\oplus} \simeq 2\pi/(23 \text{ hr } 56 \text{ min})$. Due to the orbital motion of the Earth, the variation may also contain annual components.

The ISS and other spacecraft provide interesting platforms for future clock-comparison experiments. The orbital properties of the spacecraft may result in radically different behavior. For example, the orbital period of the ISS is about 92 min. The comparable period for an Earth-based experiment is the Earth's sidereal period. This suggests a significant reduction in data-acquisition time for a space-based experiment compared to its Earth-based counterpart.

We begin our discussion by considering the effects of Lorentz violation on the resonant frequency of cavities. We then consider two classes of cavities, optical and microwave, which are currently under development for precision tests of relativity.

4.1 General Considerations

The quantity of interest is the fractional resonant-frequency shift $\delta\nu/\nu$. Consider a harmonic system satisfying the Maxwell equations (6). Suppose \vec{E}_0 , \vec{B}_0 , \vec{D}_0 and \vec{H}_0 are the conventional solutions with resonant angular frequency ω_0 . Let \vec{E} , \vec{B} , \vec{D} and \vec{H} be solutions for nonzero $(k_F)_{\kappa\lambda\mu\nu}$ with angular frequency ω . Manipulating the Maxwell equations for both sets of fields, we obtain the expression

$$\begin{aligned} \frac{\delta\nu}{\nu} = \frac{\omega - \omega_0}{\omega_0} = & - \left(\int_V d^3x (\vec{E}_0^* \cdot \vec{D} + \vec{H}_0^* \cdot \vec{B}) \right)^{-1} \\ & \times \int_V d^3x \left(\vec{E}_0^* \cdot \vec{D} - \vec{D}_0^* \cdot \vec{E} - \vec{B}_0^* \cdot \vec{H} + \vec{H}_0^* \cdot \vec{B} \right. \\ & \left. - i\omega_0^{-1} \vec{\nabla} \cdot (\vec{H}_0^* \times \vec{E} - \vec{E}_0^* \times \vec{H}) \right), \end{aligned} \quad (18)$$

where the integrals are over the volume V of the cavity.

Note that the divergence term in Eq. (18) results in a surface integral over the boundary of V . In many situations, we can neglect such boundary terms. For example, neglecting Lorentz violations in other sectors, the fields vanish inside a perfect conductor, by usual arguments. Idealizing the walls of the cavity as a perfect conductor, the Faraday equation $\vec{\nabla} \times \vec{E} + \partial_0 \vec{B} = 0$, implies the tangential component of \vec{E} vanishes at the surface. In this scenario, the divergence term in Eq. (18) is zero.

Using Eq. (18), we can find the frequency shift perturbatively in terms of the conventional solutions. For a cavity void of matter, we have $\vec{E}_0 = \vec{D}_0$ and $\vec{B}_0 = \vec{H}_0$. The constitutive relations (5) give the approximate equalities

$$\vec{D} - \vec{E} \simeq \kappa_{DE} \cdot \vec{E}_0 + \kappa_{DB} \cdot \vec{B}_0, \quad \vec{H} - \vec{B} \simeq \kappa_{HE} \cdot \vec{E}_0 + \kappa_{HB} \cdot \vec{B}_0. \quad (19)$$

With these relations and the vanishing of the boundary term, the leading order fractional

frequency shift is

$$\frac{\delta\nu}{\nu} = -\frac{1}{4\langle U \rangle} \int_V d^3x \left(\vec{E}_0^* \cdot \kappa_{DE} \cdot \vec{E}_0 - \vec{B}_0^* \cdot \kappa_{HB} \cdot \vec{B}_0 + 2\text{Re}(\vec{E}_0^* \cdot \kappa_{DB} \cdot \vec{B}_0) \right), \quad (20)$$

where $\langle U \rangle = \int_V d^3x (|\vec{E}_0|^2 + |\vec{B}_0|^2)/4$ is the time-averaged energy stored in the unperturbed cavity. Note that $\delta\nu/\nu$ is real, indicating that the Q factor of the cavity remains unaffected by Lorentz violation at leading order.

The integrals in Eq. (20) are most readily carried out in a frame at rest with respect to the laboratory. Since the laboratory frame is not inertial in general, the laboratory-frame coefficients $(\kappa_{DE})_{\text{lab}}^{jk}$, $(\kappa_{DB})_{\text{lab}}^{jk}$ and $(\kappa_{HB})_{\text{lab}}^{jk}$ are not constant. However, using observer covariance, the laboratory-frame coefficients can be related to the coefficients in an inertial frame through observer Lorentz transformations.

There are many logical candidates for an inertial frame. For our purposes, a Sun-centered celestial equatorial frame will suffice. The coefficients in this frame $(\kappa_{DE})^{JK}$, $(\kappa_{HB})^{JK}$ and $(\kappa_{DB})^{JK}$ can be regarded as constant. The relative smallness of the velocity of the Earth in this frame, $\beta_{\oplus} \approx 10^{-4}$, implies it is usually sufficient to expand the transformation in powers of the velocity β . To order β , the relation between the laboratory-frame coefficients and the Sun-frame coefficients is given by

$$\begin{aligned} (\kappa_{DE})_{\text{lab}}^{jk} &= T_0^{jkJK} (\kappa_{DE})^{JK} - T_1^{(jk)JK} (\kappa_{DB})^{JK}, \\ (\kappa_{HB})_{\text{lab}}^{jk} &= T_0^{jkJK} (\kappa_{HB})^{JK} - T_1^{(jk)KJ} (\kappa_{DB})^{JK}, \\ (\kappa_{DB})_{\text{lab}}^{jk} &= T_0^{jkJK} (\kappa_{DB})^{JK} + T_1^{kjJK} (\kappa_{DE})^{JK} + T_1^{jkJK} (\kappa_{HB})^{JK}, \end{aligned} \quad (21)$$

with $T_0^{jkJK} \equiv R^{jJ} R^{kK}$ and $T_1^{jkJK} \equiv R^{jP} R^{kJ} \epsilon^{KPQ} \beta^Q$, where R^{jJ} is the rotation from the Sun frame to the laboratory frame, and β^Q is the velocity of the laboratory in the Sun frame. The tensor T_0 is a rotation, while T_1 is a leading-order boost contribution. Although the terms involving T_1 are suppressed by β , they access distinct combinations of coefficients and can introduce different time dependence, which may lead to fundamentally different tests.

4.2 Optical Cavities

Recent examples of modern Michelson-Morley and Kennedy-Thorndike experiments based on optical cavities include Refs. [47, 48, 49]. The basic setup of these experiments consists of a pair of stabilized lasers. One laser is stabilized by an optical cavity. The second laser is stabilized by a molecular transition which in the classical analysis is assumed to be insensitive to Lorentz violations. This laser serves as a reference frequency. The beat frequency of the combined signal is analyzed for a variation due to a change in the orientation or velocity of the cavity.

The sensitivities achieved in these experiments are typically on the order of 10^{-13} to $\delta\nu/\nu$. Analyzing these experiments in the context of the extended electrodynamics should therefore yield bounds on components of $(k_F)_{\kappa\lambda\mu\nu}$ at the level of 10^{-13} .

Regarding these cavities as two parallel planar reflecting surface, the usual solutions can be approximated as standing waves. In a reference frame at rest in the laboratory, we take

$$\vec{E}_0(x) = \vec{E}_0 \cos(\omega_0 \hat{N} \cdot \vec{x} + \phi) e^{-i\omega_0 t},$$

$$\vec{B}_0(x) = i\hat{N} \times \vec{E}_0 \sin(\omega_0 \hat{N} \cdot \vec{x} + \phi) e^{-i\omega_0 t}, \quad (22)$$

where \hat{N} is a unit vector pointing along the length of the cavity, ϕ is a phase, and \vec{E}_0 is a vector perpendicular to \hat{N} that specifies the polarization. The resonant frequencies of the conventional solutions are given by $\omega_0 = \pi m/l$, where m is an integer and l is the separation of the reflecting surfaces.

Substituting this solution into Eq. (20) yields the fractional frequency shift:

$$\frac{\delta\nu}{\nu} = -\frac{1}{2|\vec{E}_0|^2} [\vec{E}_0^* \cdot (\kappa_{DE})_{\text{lab}} \cdot \vec{E}_0 - (\hat{N} \times \vec{E}_0^*) \cdot (\kappa_{HB})_{\text{lab}} \cdot (\hat{N} \times \vec{E}_0)] . \quad (23)$$

This result depends on the orientation of the cavity in the laboratory and the polarization of the light. Transforming the laboratory-frame coefficients to the Sun-frame, using Eq. (21), introduces variations in the frequency shift due to the motion of the lab.

Consider a Earth-based laboratory. The transformation (21) includes variations at the Earth's sidereal and orbital frequencies. The orbital frequency components are a result of a boost, and are therefore suppressed relative to the purely rotational contributions. Consequently, the resonant frequency fluctuates at ω_\oplus and the second harmonic $2\omega_\oplus$, along with suppressed oscillations associated with the annual variation in the Earth's velocity.

Different experimental configurations result in different sensitivities to the coefficients $(k_F)_{\kappa\lambda\mu\nu}$, and can result in different frequencies in the variations of $\delta\nu/\nu$.

As an example, consider a cavity positioned horizontally in the laboratory with vertical polarization. Let θ be an angle specifying the orientation of the cavity in the horizontal plane. The frequency shift takes the form

$$\frac{\delta\nu}{\nu} = A + B \sin 2\theta + C \cos 2\theta, \quad (24)$$

where

$$\begin{aligned} A &= A_0 + A_1 \sin \omega_\oplus T_\oplus + A_2 \cos \omega_\oplus T_\oplus + A_3 \sin 2\omega_\oplus T_\oplus + A_4 \cos 2\omega_\oplus T_\oplus, \\ B &= B_0 + B_1 \sin \omega_\oplus T_\oplus + B_2 \cos \omega_\oplus T_\oplus + B_3 \sin 2\omega_\oplus T_\oplus + B_4 \cos 2\omega_\oplus T_\oplus, \\ C &= C_0 + C_1 \sin \omega_\oplus T_\oplus + C_2 \cos \omega_\oplus T_\oplus + C_3 \sin 2\omega_\oplus T_\oplus + C_4 \cos 2\omega_\oplus T_\oplus. \end{aligned} \quad (25)$$

The quantities $A_{0,1,2,3,4}$, $B_{0,1,2,3,4}$, and $C_{0,1,2,3,4}$ are linear in the coefficients for Lorentz violation and depend on the latitude of the laboratory.

From Eq. (24), we see that one possible strategy for searches for Lorentz-violation would be to rapidly rotate the cavity in the laboratory and search for variations at the harmonics of the cavity rotation frequency. This is the method used in the experiment of Brillet and Hall [47]. It has been estimated that their analysis constrains one combination of coefficients to about a part in 10^{15} [4].

Hills and Hall performed an experiment with the cavity fixed in the laboratory [48]. A bound is placed on the sidereal variation on the order of 10^{-13} . We see from Eqs. (24) and (25) that this constrains some combination of the coefficients A_1 , A_2 , B_1 , B_2 , C_1 , and C_2 .

A similar experiment has recently been performed by Braxmaier *et al.* [49]. Their analysis focuses on variations due to the orbital motion of the Earth. In the present context, this corresponds to β suppressed terms arising from the leading order boost contributions in the transformation (21). They achieve fractional-frequency sensitivity of $4.8 \pm 5.3 \times 10^{-12}$, which leads to an estimated constraint on a combination of coefficients on the order of 10^{-8} .

It should be noted that β suppressed terms involve parity-odd coefficients, while the unsuppressed terms are only sensitive to parity-even coefficients. Therefore, consideration of these terms seems worthwhile even at reduced sensitivity.

The above experiments place loose constraint on three combinations of coefficients. It is likely that reanalyzing these experiments in terms of the standard-model extension would place constraints on more combinations at similar levels.

4.3 Microwave Cavities

Microwave-cavity oscillators are among the most stable clocks. Cavities constructed of superconducting niobium have achieved frequency stabilities of 3×10^{-16} . In an effort to perform improved tests of relativity, superconducting microwave oscillators are being developed by the SUMO project for use on upcoming ISS missions [50].

Equation (20) can be applied to cavities of any geometry and operated in any mode. Here we consider a cylindrical cavity of circular cross section, operated in the fundamental TM_{010} mode. The integrals in Eq. (20) are easily carried out in a frame fixed to the cavity with its 3 axis along the symmetry axis. In terms of coefficients in the cavity-fixed frame, the fractional frequency shift is

$$\frac{\delta\nu}{\nu} = -\frac{1}{2}(\kappa_{DE})_{\text{cav}}^{33} + \frac{1}{4}[(\kappa_{HB})_{\text{cav}}^{11} + (\kappa_{HB})_{\text{cav}}^{22}] . \quad (26)$$

It is not difficult to generalize this expression to an arbitrary laboratory frame in which the cavities symmetry axis points in a direction specified by a unit vector \hat{N} . The result is

$$\frac{\delta\nu}{\nu} = \frac{1}{4}(\kappa_{HB})_{\text{lab}}^{jj} - \frac{1}{4}\hat{N}^j\hat{N}^k[2(\kappa_{DE})_{\text{lab}}^{jk} + (\kappa_{HB})_{\text{lab}}^{jk}] . \quad (27)$$

Using transformation (21) we express this in terms of the Sun-frame coefficients. We find

$$\frac{\delta\nu}{\nu} = -\frac{1}{4}\hat{N}^j\hat{N}^k R^{jJ} R^{kK} (\tilde{\kappa}_{e'})^{JK} - \frac{1}{2}(\delta^{jk} + \hat{N}^j\hat{N}^k) R^{jJ} R^{kK} \epsilon^{JPQ} \beta^Q (\tilde{\kappa}_{o'})^{KP} - \tilde{\kappa}_{\text{tr}} , \quad (28)$$

where for convenience we define the linear combinations

$$(\tilde{\kappa}_{e'})^{JK} = 3(\tilde{\kappa}_{e+})^{JK} + (\tilde{\kappa}_{e-})^{JK} , \quad (\tilde{\kappa}_{o'})^{JK} = 3(\tilde{\kappa}_{o-})^{JK} + (\tilde{\kappa}_{o+})^{JK} . \quad (29)$$

The matrix combinations $\tilde{\kappa}_{e'}$ and $\tilde{\kappa}_{o'}$ are traceless. The first contains five linearly independent combinations of the 11 parity-even coefficients for Lorentz violation, while $\tilde{\kappa}_{o'}$ contains all eight parity-odd coefficients.

As an example, consider two identical cavities, operated in the above mode, oriented at right angles to each other on the ISS. In general, the resonant frequency of the cavities will

vary at the first and second harmonics of the stations orbital frequency ω_s . A search for Lorentz violation could be performed by looking for this variation in the beat frequency of the two cavities. The variation takes the general form

$$\frac{\nu_{beat}}{\nu} \equiv \frac{\delta\nu_1}{\nu} - \frac{\delta\nu_2}{\nu} = \mathcal{A}_s \sin \omega_s T_s + \mathcal{A}_c \cos \omega_s T_s + \mathcal{B}_s \sin 2\omega_s T_s + \mathcal{B}_c \cos 2\omega_s T_s + \mathcal{C}, \quad (30)$$

where \mathcal{A}_s , \mathcal{A}_c , \mathcal{B}_s , and \mathcal{B}_c are four linear combinations of the coefficients for Lorentz violation. These combinations depend on the orientations of the cavity pair and on the orientation of the orbital plane with respect to the Sun-centered frame. The precession of the ISS orbit slowly changes the four combinations, allowing access to more coefficients. Typically, these are rather cumbersome [4] and are omitted here.

The sensitivity to the coefficients $(k_f)_{\kappa\lambda\mu\nu}$ strongly depends on the orientations of the cavities. It can be shown that orienting a cavity with \hat{N} in the orbital plane maximizes the sensitivity to the second harmonics, at leading order in β . Orienting a cavity so that \hat{N} is 45° out of the plane maximizes sensitivity to the first harmonics. A sensible configuration might have one cavity in the orbital plane and one 45° out of it.

There are many variations of the above experiment that could be performed. Earth-based experiments similar to those discussed Sec. 4.2 could also be performed using microwave cavities. Operating in different modes or using cavities filled with matter changes the combinations of coefficients to which the experiment is sensitive. It is also possible to compare the resonant frequency of a cavity to a reference clock other than another cavity oscillator. For example, the reference clock could be a hydrogen maser or atomic clock, which could conveniently be operated on a transition known to be insensitive to Lorentz violation [25].

With current stabilities, it seems likely that microwave-cavity oscillators could access coefficients that are currently unmeasured, at levels comparable to the those of optical-cavity experiments and perhaps at the 10^{-16} level.

5. Summary

In this work, we considered the experimental consequences of a Lorentz-violating electrodynamics which arises from a Lorentz- and CPT-violating standard-model extension. We found

		Astrophysical Tests		Cavity Tests	
Coeff.	No.	Velocity	Polarization	Optical	Microwave
$\tilde{\kappa}_{e+}$	5	-16	-32	★	-
$\tilde{\kappa}_{e-}$	5	n/a	n/a	★	-
$\tilde{\kappa}_{o+}$	3	n/a	n/a	★	-
$\tilde{\kappa}_{o-}$	5	-16	-32	★	-
$\tilde{\kappa}_{tr}$	1	n/a	n/a	-	-

Table 3: Existing constraints.

that astrophysical bounds on birefringence lead to stringent constraints on ten coefficients for Lorentz violation. Access to the remaining coefficients may be accomplished through clock-comparison tests involving resonant cavities.

We summarize the current constraints in Table 3. The 19 coefficients $(k_F)_{\kappa\lambda\mu\nu}$ are represented by the matrices $\tilde{\kappa}_{e+}$, $\tilde{\kappa}_{e-}$, $\tilde{\kappa}_{o+}$, $\tilde{\kappa}_{o-}$, $\tilde{\kappa}_{tr}$ defined in Eq. (7). The number of independent components in each matrix is shown in the second column. The third and fourth column give the order of magnitude of astrophysical bounds. Laboratory experiments with optical and microwave cavities can in principle access all the coefficients. The matrices for which a few components are probably constrained by the optical cavity experiments discussed in Sec. 4.1 are indicated by the symbol \star in the table. To date, no measurements of Lorentz violation using microwave cavities have been reported.

We conclude by remarking that even though the ten coefficients in $\tilde{\kappa}_{e+}$ and $\tilde{\kappa}_{o-}$ are tightly constrained by astrophysical measurements, confirming these in laboratory experiments provides an important check because the systematics in the two types of experiments are significantly different. Furthermore, cavity experiments access currently unexplored regions in parameter space, and they offer the possibility of discovering physics beyond the standard model.

Acknowledgments

I thank Alan Kostelecký for collaboration on this work. The research described here was supported in part by the National Aeronautics and Space Administration under grant number NAG8-1770 and by the United States Department of Energy under grant number DE-FG02-91ER40661.

References

1. A.A. Michelson and E.W. Morley, Am. J. Sci. **34**, 333 (1887); Phil. Mag. **24**, 449 (1887).
2. R.J. Kennedy and E.M. Thorndike, Phys. Rev. **42**, 400 (1932).
3. Later versions of these tests include G. Joos, Ann. Phys. **7**, 385 (1930); Naturwiss. **38**, 784 (1931); T.S. Jaseja *et al.*, Phys. Rev. **133**, A1221 (1964). For a review and analysis of early experiments, see, for example, R.S. Shankland *et al.*, Rev. Mod. Phys. **27**, 167 (1955).
4. V.A. Kostelecký and M. Mewes, Phys. Rev. Lett. **87**, 251304 (2001); preprint IUHET 449 (hep-ph/0205211).
5. D. Colladay and V.A. Kostelecký, Phys. Rev. D **55**, 6760 (1997); **58**, 116002 (1998); Phys. Lett. B **511**, 209 (2001);
6. For overviews of various ideas, see, for example, V.A. Kostelecký, ed., *CPT and Lorentz Symmetry II*, World Scientific, Singapore, 2002.
7. V.A. Kostelecký and R. Lehnert, Phys. Rev. D **63**, 065008 (2001).
8. V.A. Kostelecký and S. Samuel, Phys. Rev. D **39**, 683 (1989); **40**, 1886 (1989); Phys.

- Rev. Lett. **63**, 224 (1989); **66**, 1811 (1991); V.A. Kostelecký and R. Potting, Nucl. Phys. B **359**, 545 (1991); Phys. Lett. B **381**, 89 (1996); Phys. Rev. D **63**, 046007 (2001); V.A. Kostelecký, M. Perry, and R. Potting, Phys. Rev. Lett. **84**, 4541 (2000); M.S. Berger and V.A. Kostelecký, Phys. Rev. D **65**, 091701(R) (2002).
9. S.M. Carroll *et al.*, Phys. Rev. Lett. **87**, 141601 (2001); Z. Guralnik *et al.*, Phys. Lett. B **517**, 450 (2001); A. Anisimov *et al.*, hep-ph/0106356; C.E. Carlson *et al.*, Phys. Lett. B **518**, 201 (2001).
 10. KTeV Collaboration, Y.B. Hsiung *et al.*, Nucl. Phys. Proc. Suppl. **86**, 312 (2000).
 11. OPAL Collaboration, R. Ackerstaff *et al.*, Z. Phys. C **76**, 401 (1997); DELPHI Collaboration, M. Feindt *et al.*, preprint DELPHI 97-98 CONF 80 (1997); BELLE Collaboration, K. Abe *et al.*, Phys. Rev. Lett. **86**, 3228 (2001).
 12. R.W. Gardner, FOCUS Collaboration, in Ref. [6].
 13. V.A. Kostelecký, Phys. Rev. Lett. **80**, 1818 (1998); Phys. Rev. D **61**, 016002 (2000); **64**, 076001 (2001).
 14. V.A. Kostelecký and R. Potting, Phys. Rev. D **51**, 3923 (1995); D. Colladay and V.A. Kostelecký, Phys. Lett. B **344**, 259 (1995); Phys. Rev. D **52**, 6224 (1995); V.A. Kostelecký and R. Van Kooten, Phys. Rev. D **54**, 5585 (1996); N. Isgur *et al.*, Phys. Lett. B **515**, 333 (2001).
 15. O. Bertolami *et al.*, Phys. Lett. B **395**, 178 (1997).
 16. V.W. Hughes, H.G. Robinson, and V. Beltran-Lopez, Phys. Rev. Lett. **4** (1960) 342; R.W.P. Drever, Philos. Mag. **6** (1961) 683; J.D. Prestage *et al.*, Phys. Rev. Lett. **54** (1985) 2387; S.K. Lamoreaux *et al.*, Phys. Rev. A **39** (1989) 1082; T.E. Chupp *et al.*, Phys. Rev. Lett. **63** (1989) 1541.
 17. V.A. Kostelecký and C.D. Lane, Phys. Rev. D **60**, 116010 (1999); J. Math. Phys. **40**, 6245 (1999).
 18. C.J. Berglund *et al.*, Phys. Rev. Lett. **75** 1879 (1995); L.R. Hunter *et al.*, in V.A. Kostelecký, ed., *CPT and Lorentz Symmetry*, World Scientific, Singapore, 1999.
 19. D. Bear *et al.*, Phys. Rev. Lett. **85**, 5038 (2000).
 20. D.F. Phillips *et al.*, Phys. Rev. D **63**, 111101 (2001); M.A. Humphrey *et al.*, physics/0103068; Phys. Rev. A **62**, 063405 (2000).
 21. H. Dehmelt *et al.*, Phys. Rev. Lett. **83**, 4694 (1999); R. Mittleman *et al.*, Phys. Rev. Lett. **83**, 2116 (1999); G. Gabrielse *et al.*, Phys. Rev. Lett. **82**, 3198 (1999); R. Bluhm *et al.*, Phys. Rev. Lett. **82**, 2254 (1999); Phys. Rev. Lett. **79**, 1432 (1997); Phys. Rev. D **57**, 3932 (1998).
 22. B. Heckel *et al.*, in B.N. Kursunoglu *et al.*, eds., *Elementary Particles and Gravitation*, Plenum, New York, 1999; R. Bluhm and V.A. Kostelecký, Phys. Rev. Lett. **84**, 1381 (2000).
 23. S.M. Carroll, G.B. Field, and R. Jackiw, Phys. Rev. D **41**, 1231 (1990).
 24. V.W. Hughes *et al.*, Phys. Rev. Lett. **87**, 111804 (2001); R. Bluhm *et al.*, Phys. Rev.

- Lett. **84**, 1098 (2000).
25. R. Bluhm *et al.*, Phys. Rev. Lett. **88**, 090801 (2002).
 26. R. Jackiw and V.A. Kostelecký, Phys. Rev. Lett. **82**, 3572 (1999).
 27. S.R. Kulkarni *et al.*, Nature **393**, 35 (1998).
 28. W.S. Paciesas *et al.*, Ap. J. Supp. **122**, 465 (1999).
 29. S.R. Kulkarni *et al.*, Nature **398**, 389 (1999).
 30. A.S. Frutcher, Ap. J. **512**, L1 (1999).
 31. P.M. Vreeswijk *et al.*, GCN Circ. **324**, (1999).
 32. D.A. Smith, K. Hurley, and T. Cline, GCN Circ. **568**, (2000).
 33. S.M. Castro *et al.*, GCN Circ. **650**, (2000).
 34. J.H. Taylor, R.N. Manchester, and A.G. Lyne, Ap. J. Supp. **88**, 529 (1993).
 35. S. Sallmen *et al.*, Ap. J. **517**, 460 (1999).
 36. A. Kinkhabwala and S.E. Thorsett, Ap. J. **535**, 365 (2000).
 37. J.H. Hough *et al.*, Mon. Not. R. astr. Soc. **224**, 1013 (1987).
 38. C. Brindle *et al.*, Mon. Not. R. astr. Soc. **244**, 577 (1990).
 39. A. Cimatti *et al.*, Ap. J. **465**, 145 (1996).
 40. A. Dey *et al.*, Ap. J. **465**, 157 (1996).
 41. A. Cimatti *et al.*, Ap. J. **476**, 677 (1997).
 42. M.S. Brotherton *et al.*, Ap. J. **487**, L113 (1997).
 43. M.S. Brotherton *et al.*, Ap. J. **501**, 110 (1998).
 44. M.S. Brotherton *et al.*, Ap. J. **546**, 134 (2001).
 45. M. Kishimoto *et al.*, Ap. J. **547**, 667 (2001).
 46. J. Vernet *et al.*, Astron. Astrophys. **366**, 7 (2001).
 47. A. Brillet and J.L. Hall, Phys. Rev. Lett. **42**, 549 (1979).
 48. D. Hils and J.L. Hall, Phys. Rev. Lett. **64**, 1697 (1990).
 49. C. Braxmaier *et al.*, Phys. Rev. Lett. **88**, 010401 (2002).
 50. S. Buchman *et al.*, Adv. Space Res. **25**, 1251 (2000); J. Turneare *et al.*, Phys. Rev. D **27**, 1705 (1983).

STEP Technology Status

Glen Sapilewski
STEP Program, Hansen Labs, Stanford University
Stanford, CA 94305-4085

Significant technical progress has been made this past year advancing key technologies needed to implement STEP. Together with our collaborators in Europe and industry, we have continued to advance the development of the STEP Instrument (Differential Accelerometer, Quartz Block, and Probe) and the STEP Dewar.

We have manufactured for the first time a thin film magnetic bearing (with superconducting cables) as specified by the flight Differential Accelerometer design. A prototype accelerometer with magnetic bearing is currently under test in our Accelerometer Test Facility (ATF). The ATF suspends a test mass at 4 K by a 1.5-meter long fiber. The torsion mode has a 100 second period, comparable to the stiffness required by the magnetic bearing in orbit. We will present prototype accelerometer and ATF status.

STEP Instrument and Dewar design has progressed significantly in two ways: (1) Probe design led by the University of Birmingham with Rutherford Appleton Laboratory, and in collaboration with Stanford University with Lockheed Martin; and (2) Dewar design with aerogel led by Lockheed Martin in collaboration with Stanford, JPL, and the University of Trento. The Dewar thermal model incorporating the Probe design predicts a Dewar lifetime of 8.2 months (requirement is 6 months).

Short-Range Inverse-Square Law Experiment in Space

Ho Jung Paik and M. Vol Moody

Department of Physics, University of Maryland, College Park, MD 20742

Donald M. Strayer

Jet Propulsion Laboratory, 4800 Oak Grove Drive, Pasadena, CA 91109

The objective of ISLES (Inverse-Square Law Experiment in Space) is to perform a null test of Newton's law on ISS with a resolution of one part in 10^5 at ranges from $100\ \mu\text{m}$ to $1\ \text{mm}$. ISLES will be sensitive enough to detect axions with the strongest allowed coupling and test the string-theory prediction with $R \geq 5\ \mu\text{m}$. The experiment will be cooled to $\leq 2\ \text{K}$ in LTMPF, which permits superconducting magnetic levitation in micro-g, allowing very soft, low-loss suspension of the test masses. The low magnetic damping, combined with a low-noise SQUID, leads to extremely low intrinsic noise in the detector. To minimize Newtonian errors, ISLES employs a near null source, a circular disk of large diameter-to-thickness ratio. Two test masses, also disk-shaped, are suspended on the two sides of the source mass at a distance of $100\ \mu\text{m}$. The signal is detected by a superconducting differential accelerometer, which is a highly sensitive gravity sensor.

1. Objective of ISLES

The Newtonian inverse-square ($1/r^2$) law of gravity is a cornerstone of General Relativity (GR). Its validity has been impressively demonstrated by astronomical observations in the solar system, exceeding a level of one part in 10^8 at $10^7 \sim 10^9\ \text{km}$. In the wake of interests in searching for a "fifth force," the past two decades has seen increased activities in testing the $1/r^2$ law on the laboratory and geological scales. The experimental limit at $1\ \text{cm} \sim 10\ \text{km}$ now stands at one part in $10^3 \sim 10^4$. However, due to difficulties associated with designing sensitive short-range experiments, the range below $1\ \text{mm}$ has been left largely unexplored (Adelberger *et al.*, 1991).

Figure 1 shows the existing limit for the $1/r^2$ law at ranges below $1\ \text{mm}$ and the sensitivity of ISLES, plotted as a function of range l , where the total potential is written as

$$V(r) = -\frac{GM}{r}(1 + a e^{-r/l}). \quad (1)$$

Violations predicted by various theories are also indicated. The expected resolution of ISLES is $|a| = 1 \times 10^{-5}$ at $l = 100\ \mu\text{m} \sim 1\ \text{mm}$ and $|a| = 1 \times 10^{-2}$ at $l = 10\ \mu\text{m}$. At $100\ \mu\text{m}$, this represents an improvement over the existing limits (Hoyle *et al.*, 2001) by over six orders of

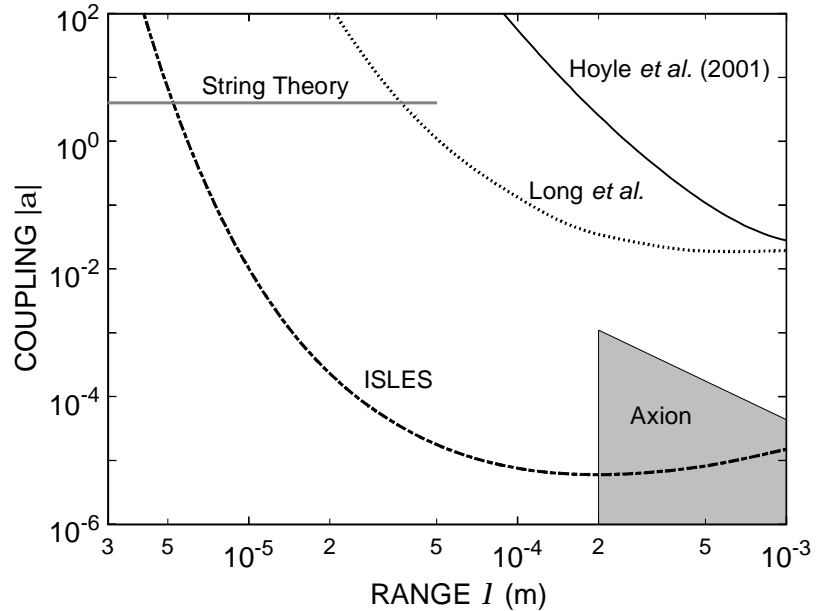


Figure 1. Sensitivity of ISLES versus the existing limit.

magnitude. ISLES reaches four orders of magnitude beyond the level aimed at by Long *et al.* (1999) in their laboratory experiment. The improvement at $\leq 100 \mu\text{m}$ is greater. The ISLES is capable of detecting the axion with highest allowed coupling ($q = 3 \times 10^{-10}$) and will test a string theory prediction with $R_2 \geq 5 \mu\text{m}$. ISLES is based on the superconducting gravity gradiometer (SGG) technology fully developed at the University of Maryland (Moody *et al.*, 2002).

2. Scientific Value of Short-Range $1/r^2$ Law Test

Test of General Relativity. Existence of a short-range mass-mass interaction implies a violation of the $1/r^2$ law, a cornerstone of GR. Such a force may or may not have composition dependence. Therefore, the $1/r^2$ law could be violated even when the Equivalence Principle (EP) holds rigorously. So ISLES will complement STEP (Satellite Test of the Equivalence Principle), which aims at testing the EP to one part in 10^{18} at the opposite end of the range, $l \geq 10^4 \text{ km}$

Test of string theories. String theories can be consistently formulated only in nine spatial dimensions. Because the space we observe is three-dimensional, the extra dimensions must be hidden. If there are n compact dimensions with radii R_1, R_2, \dots, R_n , Gauss's law implies that the Planck mass M_{Pl} is related to a fundamental scale M_* by

$$M_{Pl}^2 \approx M_*^{2+n} R_1 R_2 \dots R_n. \quad (2)$$

As we probe distances shorter than one of the radii R_i , a new dimension opens up and changes the r dependence of the gravitational force law.

One theoretically well-motivated value for M_* is 1 TeV, which solves the gauge hierarchy problem; namely, gravity is so weak compared to the other forces. For two large dimensions of similar size, one obtains $R_1 \approx R_2 \approx 1 \text{ mm}$ (Arkani-Hamed *et al.*, 1999). Cosmological and astrophysical constraints give a bound $M_* > 100 \text{ TeV}$ (Cullen and Perelstein, 1999; Hall and Smith, 1999), with the most stringent bound, $M_* > 1700 \text{ TeV}$, coming from the evolution of neutron stars (Hannestad and Raffelt, 2002). This most stringent bound corresponds to $R_1 \approx R_2 < 40 \text{ nm}$. While this is beyond the reach of ISLES, there are cosmological assumptions going into these bounds, and a null result would supply independent confirmation of the model being tested.

Search for the axion. The Standard Model of particle physics successfully accounts for all existing particle data; however, it has one serious blemish: the strong CP problem. Strong interactions are such that parity (P), time reversal (T), and charge conjugation (C) symmetries are automatically conserved in perturbation theory. However, non-perturbative effects induce violations of P and CP (parameterized by a dimensionless angle q), but no such violations have been observed in strong interactions. Peccei and Quinn (1977) developed an attractive resolution of this problem. One ramification of their theory is the existence of a new light-mass boson, the *axion* (Weinberg, 1978; Wilczek, 1978). The axion mediates a short-range mass-mass interaction. The experimental upper bound $q \leq 3 \times 10^{-10}$ corresponds to a violation of the $1/r^2$ law at the level of $|a| \approx 10^{-4}$ at $l = 1 \text{ mm}$, which is within reach for ISLES.

The axion could also solve the major open question in astrophysics: the composition of dark matter. Galactic rotation curves and inflation theory require that there should be more mass in the universe than is observed. Although neutrino mass, MACHOs (MASSive Compact Halo Objects), and many hypothetical particles have been offered as explanations, the solution remains elusive. The axion is one of the strongest candidates for the cold dark matter (Turner, 1990).

3. Principle of Experiment

Newtonian null source. To maximize the masses that can be brought to 100 μm from each other, flat disk geometry is used for both the source and test masses, as is done by Long *et al.* (1999). An infinite plane slab is a Newtonian null source. We approximate this by using a circular disk of sufficiently large diameter. Figure 2 shows the configuration of the source and test masses with associated coils and capacitor plates.

Levitated test masses. Two disk-shaped superconducting test masses are suspended on two sides of the source mass and are coupled magnetically to form a differential accelerometer. The motions induced in the test masses are detected by sensing coils (L_{S1} and L_{S2}).

Under 1 g, it is difficult to suspend two flat disks on two sides of the source mass at such proximity without significantly modifying the geometry and stiffening the differential mode, thus degrading the resolution of the experiment. In micro-g, each test mass can be suspended by applying only minute forces from a pancake coil (L_{S1} or L_{S2}) and a small ring coil (L_{R1} or L_{R2}) coupled to a narrow slanted rim of the test mass with negligible mass.

Second harmonic detection. As the source mass is driven at frequency f_s along the symmetry axis, the first-order Newtonian fields arising from the finite diameter of the source mass are canceled upon differential measurement, leaving only a second-order error at $2f_s$. By symmetry, the Yukawa signal also appears at $2f_s$. The second harmonic detection, combined with the common-mode rejection ratio (CMRR) of the detector, reduces source-detector vibration coupling by over 300 dB.

Expected signal. The design allows a source displacement of $\pm 50 \mu\text{m}$. The differential acceleration signals expected from the Newtonian (with 10% correction) and Yukawa forces with $|a| = 10^{-5}$ and $I = 100 \mu\text{m}$ are plotted in Figure 3 as a function of the source mass position. The rms amplitude of the Yukawa signal, corresponding to a $\pm 50\text{-}\mu\text{m}$ displacement, is $8.5 \times 10^{-12} a \text{ m s}^{-2}$. The rms amplitude of the Newtonian term, arising from the finite diameter of the source mass, is $1.0 \times 10^{-16} \text{ m s}^{-2}$ before compensation. The Newtonian error will be computed and removed to $\leq 10\%$, which is straightforward.

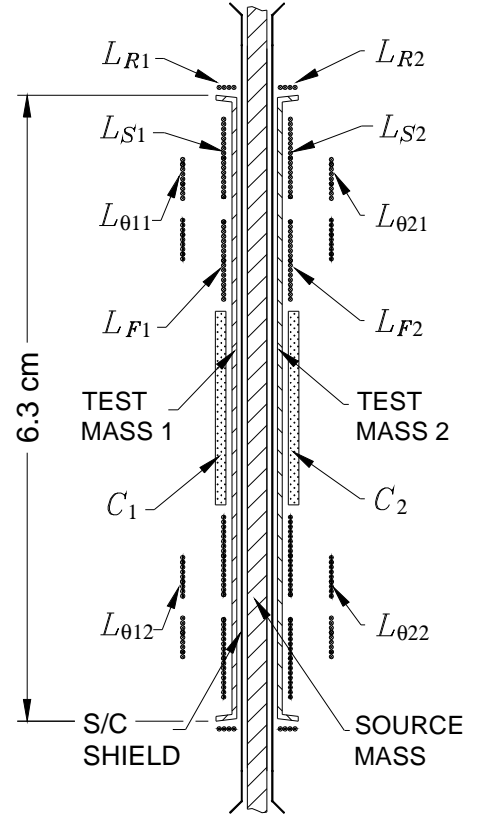


Figure 2. Configuration of the source and test masses.

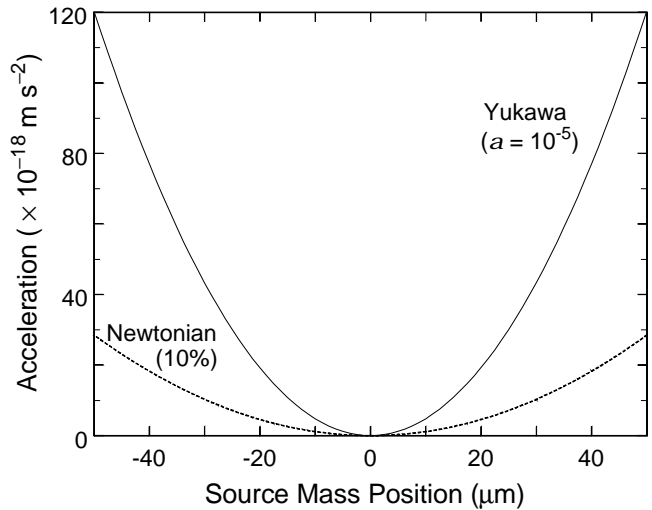


Figure 3. Newtonian and Yukawa signals versus source position.

Need for low gravity. Sensitive experiments searching for weak forces invariably require soft suspension for the measurement degree of freedom. A promising soft suspension is superconducting magnetic levitation. Levitation in 1 g, however, requires a large magnetic field, which tends to couple to the measurement axis through metrology errors and thus stiffens the mode. The high field also makes suspension more dissipative. Fields close to the critical field (H_c) of the superconductor must be used to levitate the masses in 1 g. Surface impurities will reduce H_c locally. The field will also be stronger near sharp edges. These effects cause the magnetic fields to be trapped, which contributes to damping of the motions through flux creep.

The situation improves dramatically in space. The g-level is reduced by five to six orders of magnitude, so the test masses can be supported with weaker magnetic springs, permitting the realization of both the lowest resonance frequency and lowest dissipation. Our calculation shows that, even on such a relatively noisy platform as the ISS, the space experiment will have at least 100 times better resolution over the ground experiment.

4. Experimental Hardware

Overview of the apparatus. Figure 4 shows a cross-sectional view of the apparatus. The entire housing is fabricated from niobium (Nb). The source mass is made out of tantalum (Ta), which closely matches Nb in thermal contraction. It is suspended by cantilever springs at the edge and driven magnetically. A thin Nb shield provides electrostatic and magnetic shielding between the source and each test mass. The test masses are suspended and aligned by magnetic fields from various coils. Two auxiliary three-axis superconducting accelerometers are mounted on two sides of the housing to provide linear and angular acceleration signals.

The entire assembly weighs 6.0 kg and fits within the 20-cm diameter envelope of the LTMPF instrument well. The masses need not be caged during launch and ISS maneuvers since their sway space will be limited to $\pm 50 \mu\text{m}$ by mechanical stops.

The ISLES cryogenic and electrical requirements will be met with the standard LTMPF provision with minor improvements. The entire apparatus is fastened to the second-stage thermal platform of the Cryo Insert of LTMPF, which will be stabilized to $5 \mu\text{K}$ (Figure 5). The orientation of the detector was chosen such that its sensitive axis is aligned with the pitch (y) axis of the ISS when LTMPF is mounted on JEM-EF. This orientation minimizes the centrifugal acceleration noise.

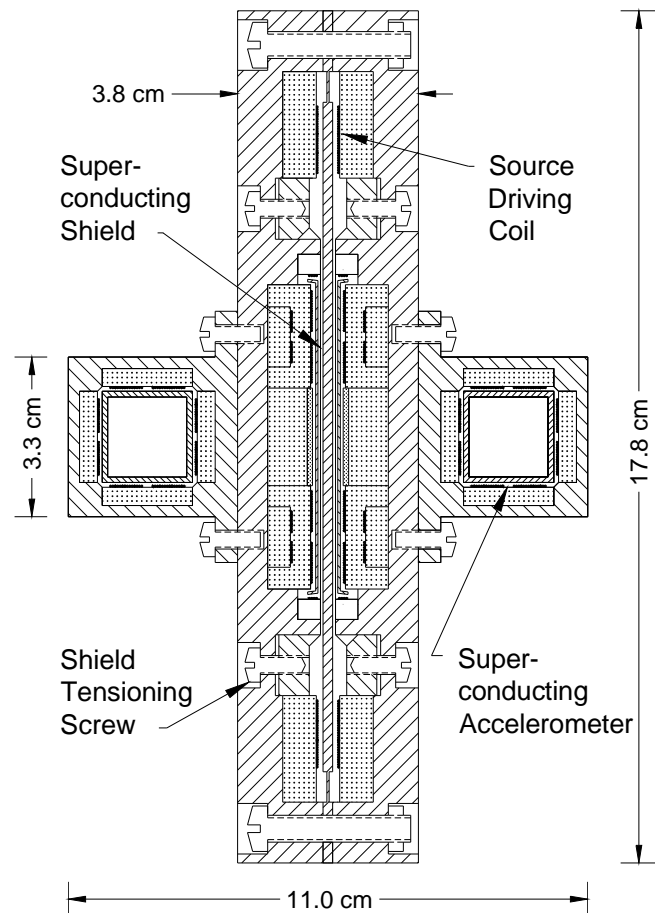


Figure 4. Cross section of the ISLES apparatus.

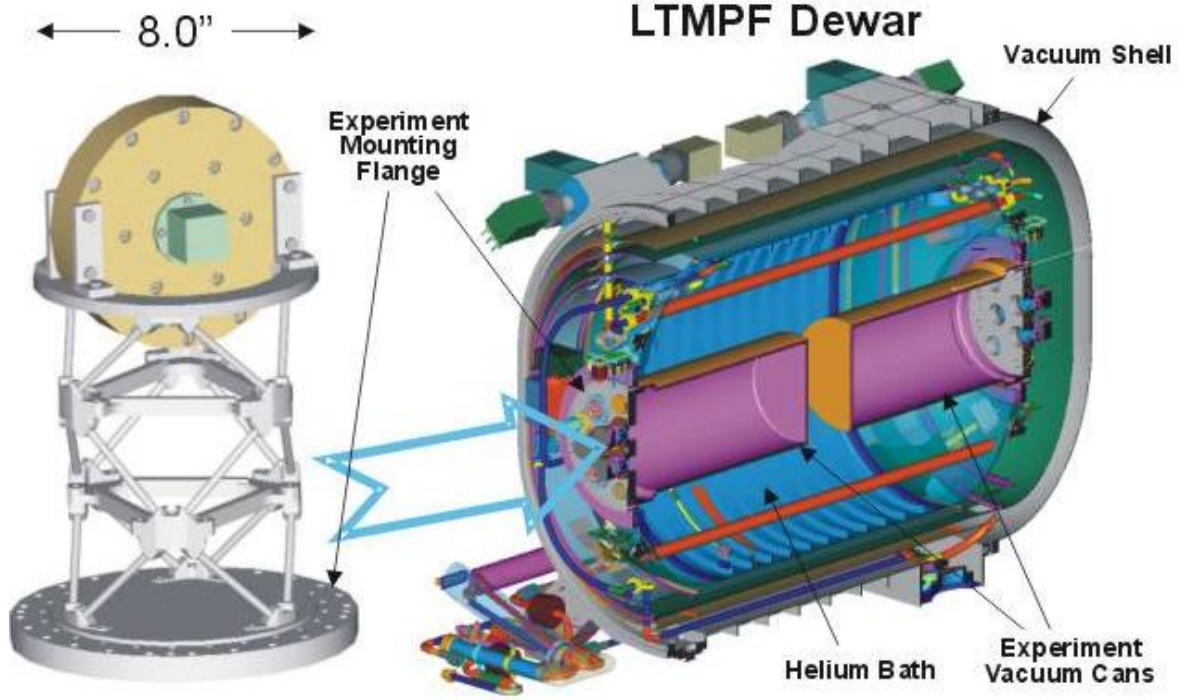


Figure 5. The ISP mounted on the Cryo Insert.

Source and test masses. The source mass is a disk 2.0 mm thick by 140 mm in diameter, with mass $M = 510$ g. The source mass, cantilever springs, and rim are machined out of a single plate of Ta. Ta is chosen for its high density (16.6 g cm^{-3}), which increases the signal, and its relatively high H_c . Each test mass is a Nb disk 0.25 mm thick by 63 mm in diameter, with a rim 0.25 mm thick by 2.0 mm wide, which has 5° slant from the axis. The mass of each test mass is $m = 7.5$ g. The test masses are separated by a baseline $\ell = 2.45$ mm. The position of each test mass is measured by a capacitor plate located near its center (see Figure 2).

The equilibrium spacing between the source and each test mass is $100 \mu\text{m}$. They are shielded from each other by means of a $12.5\text{-}\mu\text{m}$ thick Nb shield, located at $25 \mu\text{m}$ from the surface of the test mass. The source mass is driven magnetically by coupling a small ac current to a superconducting circuit carrying a large persistent current.

Superconducting circuitry and setup procedure. Schematics of the superconducting circuits for the detector are shown in Figure 6. These circuits are similar to the standard differencing circuit used in the SGG (Moody *et al.*, 2002). The test masses are suspended radially by storing persistent currents I_{R1} and I_{R2} in ring coils L_{R1} and L_{R2} and the pancake coils, as shown in Figure 6(a). Due to the slanted rim of the test masses, currents I_{R1} and I_{R2} will exert an axially outward force on the test masses. This force is balanced by the axially inward forces provided by the currents in the sensing, alignment, and feedback circuits, shown in Figures 6(b), (c), and (d). The suspension is stable for all degrees of freedom, except for roll about the sensitive axes.

The scale factors of the component accelerometers are matched by adjusting currents I_{S1} and I_{S2} in pancake coils L_{S1} and L_{S2} , as shown in Figure 6(b). The SQUID measures the differential acceleration a_D , or gravity gradient, along the y-axis. To align an individual test mass parallel to its shield and to also align its axis parallel to the axis of the other mass, two alignment circuits

are provided for each test mass, one per degree of freedom. Figure 6(c) shows the alignment circuit of test mass 1 about the x -axis. This alignment is accomplished by tuning currents I_{q11} and I_{q12} in remotely coupled pancake coils L_{q11} and L_{q12} (see Figure 2).

The balance procedure matches the linear components of the scale factors but does not completely match the nonlinearity. This mismatched nonlinearity is troublesome since it down-converts the wideband acceleration noise to the signal frequency. A standard approach to suppressing the nonlinearity is applying a negative feedback to the test masses, which *actively* stiffens the mode. The feedback circuit is given in Figure 6(d). The common-mode (CM) and differential-mode (DM) outputs i_{FC} and i_{FD} are fed back to the test masses. The CM output is derived from the auxiliary accelerometers. Currents I_{F1} and I_{F2} are adjusted to null the effect of the CM feedback on the DM output.

Coarse and fine heat-switches. Due to the high vibration levels of the ISS ($> 10^{-6} \text{ m s}^{-2} \text{ Hz}^{-1/2}$), a special provision must be made to be able to fine control the magnetic fluxes trapped in various superconducting loops. Coarse heat-switches, denoted by H_{ij} 's, warm up a short length of the Nb wire to a resistance $R \approx 1 \text{ m}\Omega$, resulting in an L/R time of about 10 ms. These coarse switches are used to store currents initially. Fine heat-switches, denoted by h_{ij} 's, couple a low-resistance path with $R_d \approx 0.1 \mu\Omega$ to the circuit, resulting in a time constant of about 100 s. With 1-ms time resolution of the heat-switch, fluxes can then be adjusted to one part in 10^5 . This fine control of the trapped currents gives the ability to match the scale factors to 10^{-5} and to align the sensitive axes to 10^{-5} rad, resulting in an initial CMRR of 10^5 in all three linear degrees of freedom.

Heat-switch H_{SD} in Figure 6(b) is turned on to protect the SQUID from a current surge whenever a current is adjusted in the sensing circuit. The output heat-switches, H_{iC} 's and H_{iD} 's, are turned on to passively damp the corresponding modes, in the event the test masses are excited.

Auxiliary superconducting accelerometers. Figure 4 shows two three-axis auxiliary superconducting accelerometers mounted symmetrically on two sides of the housing. Each test

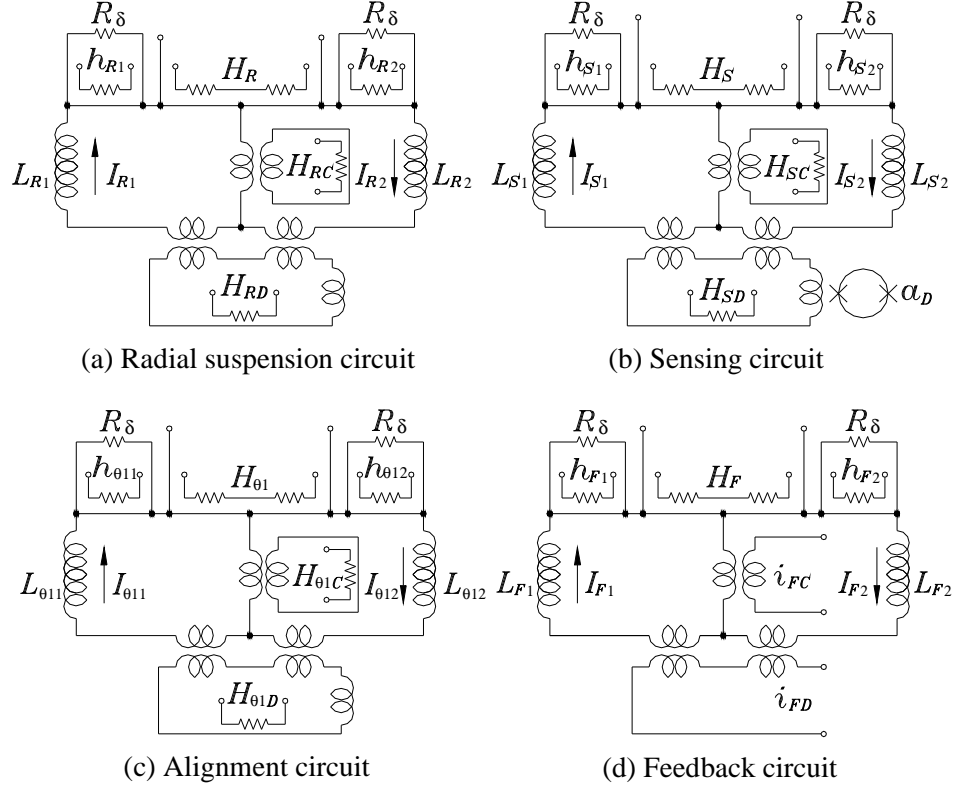


Figure 6. Superconducting circuits for the detector.

mass is a hollow 20-g Nb cube, suspended and sensed by Nb pancake coils on its six faces. The suspension is stable in all degrees of freedom. The accelerometers are coupled to SQUIDs, two SQUIDs per degree of freedom, to measure three linear (a_i) and two angular (α_i) acceleration components, as well as a gravity gradient component (Γ_{ij}).

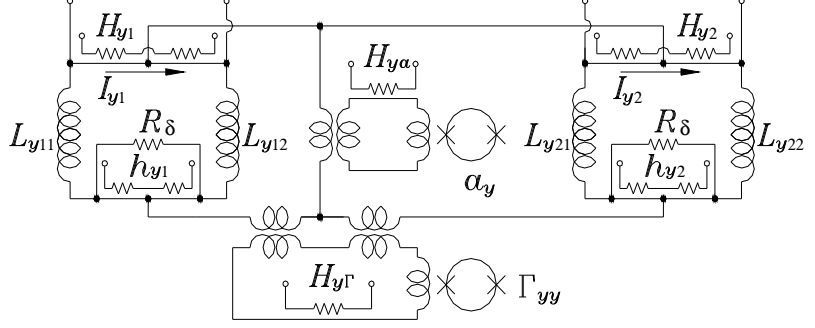


Figure 7. Superconducting circuit for the y-axis of the coupled three-axis auxiliary accelerometers.

Figure 7 shows the superconducting circuit for the y-axis of the auxiliary accelerometer. The four pancake coils separated along the y-axis are combined to sum and difference the signals. The CM and DM signals correspond to a_y and Γ_{yy} , respectively. The gravity gradient signal is used to monitor and remove gravitational disturbances from the detector. The pancake coils separated along the x- and z-axes are combined in similar circuits to measure a_x and a_z , and a_z and a_x , respectively. The only component that is not measured is a_y , which is not needed for error compensation.

The intrinsic noise of the accelerometers at $f = 0.02$ Hz are $S_a^{1/2}(f) \approx 1 \times 10^{-11} \text{ m s}^{-2} \text{ Hz}^{-1/2}$, and $S_a^{1/2}(f) \approx 3 \times 10^{-11} \text{ rad s}^{-2} \text{ Hz}^{-1/2}$, and $S_\Gamma^{1/2}(f) \approx 3 \times 10^{-11} \text{ s}^{-2} \text{ Hz}^{-1/2} = 0.03 \text{ E Hz}^{-1/2}$, where $1 \text{ E (Eötvös)} = 10^{-9} \text{ s}^{-2}$ is a unit of gravity gradient.

5. Dynamic Noise Rejection

Error compensation. Linear and angular accelerations are rejected to 10^{-5} and 10^{-4} m, respectively, by adjusting persistent currents in the sensing and alignment circuits. To improve the acceleration rejection further, we apply error compensation technique that has been demonstrated with our SGG (Moody *et al.*, 2002). The linear and angular accelerations of the platform, measured by the auxiliary accelerometers, are multiplied by the predetermined error coefficients and subtracted from the detector output. By applying the compensation factor 10^3 demonstrated in the laboratory, we should be able to achieve a net CMRR of 10^8 for linear acceleration and a net error coefficient of 10^{-7} m for angular acceleration.

To determine the dynamic error coefficients, accelerations in all degrees of freedom must be provided. If active vibration isolation is implemented, a six-axis shaker will be built into the isolation system, which can be used to apply a sinusoidal acceleration signal in each degree of freedom. Without the vibration isolation system, we will use the ISS vibration noise itself to shake the detector. The accelerations will be random and cross-correlated between degrees of freedom. However, we can apply a well-established procedure in electrical engineering for determining the transfer functions for a multiple-input system using noise alone (Bendat and Piersol, 1971).

Due to the short but finite baseline ($\ell = 2.45$ mm), the $1/r^2$ law detector is a gravity gradiometer, which is sensitive to attitude modulation of Earth's gravity gradient, gravity noise from ISS, and centrifugal acceleration. Fortunately, the auxiliary gradiometer measures exactly the same gradient noise, except for gravity disturbances from nearby objects (< 1 m). This noise can thus be removed from the detector output by applying the above correlation method.

Vibration isolation (option). With the residual acceleration errors compensated, the most important dynamic error source is the nonlinearity of the scale factors. Vibration isolation of the detector is an alternative way of suppressing the nonlinearity noise.

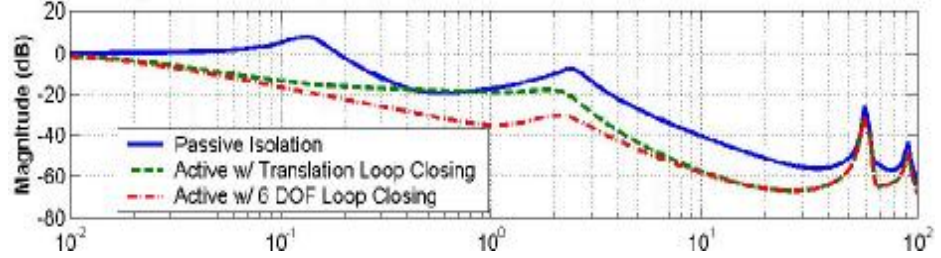


Figure 8. Frequency response of the vibration isolation system for y-axis.

An active vibration isolation system, combined with a single-stage passive isolation, was studied for LTMPF by Ball Aerospace & Technologies Corp. (BATC). As LTMPF is designed presently, the sway space is limited to ± 3 mm. This constrains our ability to extend the isolation to below 0.1 Hz. Eight D-strut isolators were used to attach the facility frame to Payload Interface Unit (PIU). These isolators provide a 40-dB/decade attenuation from 1 to 200 Hz. Each isolator is also equipped with a voice-coil actuator to provide active isolation. The outputs of the superconducting accelerometers are fed back to these actuators.

The result is shown in Figure 8. The first is the passive isolation provided by the eight D-strut isolators. The first active system shown employs only control over the translation degrees of freedom. The second active system employs closed loop control over all six degrees of freedom. The isolation system provides only a 10-dB isolation at 0.05 Hz. The main advantage comes from the reduction of high-frequency noise, which reduces the nonlinearity noise.

6. Error Budget

Metrology errors. Table 1 lists the metrology errors estimated using a numerical model. The effects from the finite diameter of the source and the dynamic mass of the suspension springs are corrected to 10% and 20%, respectively. Linear taper and linear density variation of the source produce second order errors, which become negligible. The test masses tend to rotate slowly about the sensitive axis, further averaging out the asymmetry about the axis. Hence only the radial taper and the radial density variation are important. Due to the null nature of the source, test mass metrology is not important, except for the extended rim. The rim dimension is corrected to 2.5 μm . The requirements on radial positioning of the test masses are greatly relaxed by the cylindrical symmetry. The total metrology error is $1.5 \times 10^{-17} \text{ m s}^{-2}$.

The dimensional tolerances are achievable using hand lapping of the parts. Fabrication of the test masses with a slanted rim will require a special procedure. One possibility is machining the entire structure in a single piece by combining regular machining with electric discharge machining (EDM). Another possibility is machining the disk and the rim as separate pieces and then diffusion-bonding them in a vacuum oven.

Source	Allowance	Error ($\times 10^{-18} \text{ m s}^{-2}$)
Baseline	25 μm	1.0
Source mass		
Finite diameter	10%	12
Suspension spring	20%	2.4
Radial taper	2.5 μm	7.8
Radial density variation	10^{-4}	0.2
Test masses		
Rim dimension	2.5 μm	1.7
Total error		15

Table 1. Metrology errors

Intrinsic instrument noise. The intrinsic power spectral density of a superconducting differential accelerometer can be written (Chan and Paik, 1987; Moody *et al.*, 2002) as

$$S_a(f) = \frac{8}{m} \left[\frac{k_B T w_D}{Q_D} + \frac{w_D^2}{2hb} E_A(f) \right], \quad (3)$$

where m is the mass of each test mass, $w_D = 2\pi f_D$ and Q_D are the DM resonance frequency and quality factor, b is the electromechanical energy coupling coefficient, h is the electrical energy coupling coefficient of the SQUID, and $E_A(f)$ is the input energy resolution of the SQUID.

Equation (3) shows that f_D is a critical parameter for the intrinsic noise. The micro-g on ISS, in principle, allows a suspension 10^6 times softer than on the ground, which corresponds to $f_D < 0.01$ Hz. On the other hand, the differential accelerometer's response to platform vibration must be minimized to reduce errors due to electric charge on the test mass, patch-effect fields, self-gravity of the ISS, and most importantly the nonlinearity of the scale factors. Ideally, one would like to increase f_C as much as possible, while keeping f_D low. Unfortunately, the nonlinearity of the coils couples a fraction of the CM stiffness to DM, providing a practical limit: $f_C/f_D \leq 4$. This forces us to make a compromise. The test masses must remain free before a feedback loop is closed either to the test masses or to the isolator, since otherwise there will be no signal to feed back. We need to keep the test mass excursion to ≤ 10 μm . This requires $f_C \geq 0.2$ Hz and $f_D \geq 0.05$ Hz. This represents a stiffness reduction by 10^4 from the ground experiment.

Analysis of ISLES circuits shows that $I_{11} = I_{21} \approx 4.7$ mA and $I_{13} = I_{23} \approx 47$ mA gives $f_D = 0.05$ Hz and $f_C = 0.2$ Hz. For feedback operation of the detector, this choice of mode frequencies, with signal frequency $f = 0.02$ Hz, minimizes the total dynamic noise. The radial translational mode frequency is found to be ~ 0.06 Hz. The test masses are free to roll about their axes. Rolling will tend to average out azimuthal asymmetries of the source and the test masses. If active vibration isolation is provided, the optimum frequencies shift slightly to $f = 0.05$ Hz, $f_D = 0.1$ Hz and $f_C = 0.4$ Hz. We compute the intrinsic noise for these two sets of frequencies.

The design values for the other parameters of Eq. (3) are: $T = 2$ K, $m = 7.5$ g, $Q_D = 10^6$, $b = h = 0.5$, and $E_A(f) = 10^{-30} (1 + 0.1 \text{ Hz}/f) \text{ J Hz}^{-1}$. The SQUID energy resolution corresponds to the flux noise, $5 \mu\Phi_0 \text{ Hz}^{-1/2}$, originally specified in LTMPF Science Requirement Document. This coincides with the performance typically obtained from commercially available dc SQUIDS. We assume that this SQUID noise level can be achieved for ISLES. With the above parameter values, we find $S_a^{1/2}(f) = 7.0 \times 10^{-14} \text{ m s}^{-2} \text{ Hz}^{-1/2}$ for $f = 0.02$ Hz and $f_D = 0.05$ Hz (for feedback), and $S_a^{1/2}(f) = 10.8 \times 10^{-14} \text{ m s}^{-2} \text{ Hz}^{-1/2}$ for $f = 0.05$ Hz and $f_D = 0.1$ Hz (for vibration isolation).

Acceleration Noise. The upper curve of Figure 9 shows the y-axis linear acceleration spectrum measured by a SAMS II accelerometer in the US Lab on a typical day. The lower curve is the acceleration spectrum with active isolation, which was generated by filtering the acceleration spectrum with the response function given in Figure 8. The noise is quietest at ~ 0.01 Hz, with a value of $3 \times 10^{-6} \text{ m s}^{-2} \text{ Hz}^{-1/2}$. This noise will be reduced to $3 \times 10^{-14} \text{ m s}^{-2} \text{ Hz}^{-1/2}$ by the net CMRR of 10^8 . The angular acceleration noise is reduced to $2 \times 10^{-14} \text{ m s}^{-2} \text{ Hz}^{-1/2}$ by the error coefficient of 10^{-7} m. The centrifugal acceleration noise is negligible.

Using the nonlinearity coefficient measured in our SGG (Moody *et al.*, 2002), we estimate the nonlinearity-induced noise as plotted in Figure 10. The upper curve is the noise without active isolation or feedback, which is 10^3 times higher than the intrinsic noise of the instrument at 0.01 Hz. The middle curve shows the result of applying the active isolation. At 0.01 Hz, the

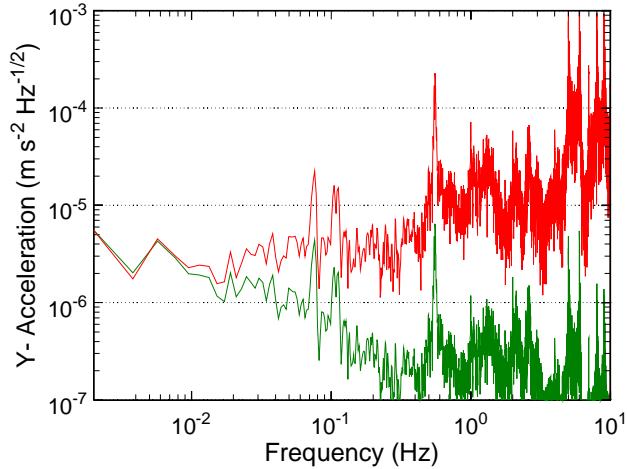


Figure 9. Linear acceleration along y-axis: actual (upper) and with active isolation (lower).

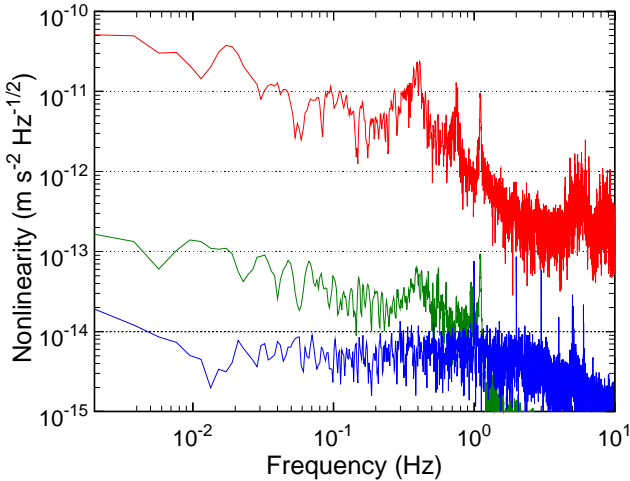


Figure 10. Nonlinearity error for y-axis: actual (upper), with active isolation (middle), and with feedback (lower).

With the high magnetic field required to drive the source mass, magnetic crosstalk between the source and the detector is a very important potential source of error. To solve this problem, the entire housing is machined out of Nb and a Nb shield is provided between the source and each test mass. High-purity Nb will be used. The Nb will be heat-treated to bring the material very close to a type-I superconductor, thus minimizing flux penetration. The superconducting shield is expected to provide over 200 dB isolation (Rigby *et al.*, 1990). This isolation, combined with 60 dB rejection from the second harmonic detection, should provide the required isolation between the source drive signal and the test masses in excess of 260 dB.

Electric charge effects. Levitated test masses in orbit will accumulate electric charge from cosmic rays and from high-energy protons, as the spacecraft traverses through the South Atlantic Anomaly. Scaling from the charge computed for STEP test masses (Blaser *et al.*, 1996), we find that the total charge accumulated in each ISLES test mass over the entire duration of the experi-

nonlinearity noise is at $1 \times 10^{-13} \text{ m s}^{-2} \text{ Hz}^{-1/2}$. The lower curve shows the nonlinearity noise expected in the detector under a feedback control, which stiffens CM to 10 Hz.

Assuming that the above acceleration noise represents the actual noise that will be experienced by the ISLES detector, we find a total acceleration noise to be $6.3 \times 10^{-14} \text{ m s}^{-2} \text{ Hz}^{-1/2}$ at $f = 0.02 \text{ Hz}$ for feedback option and $5.9 \times 10^{-14} \text{ m s}^{-2} \text{ Hz}^{-1/2}$ at $f = 0.05 \text{ Hz}$ for vibration isolation option.

Gravity noise. Helium tide is absent due to the Earth-fixed orientation of the ISS. Helium sloshing is of minor concern since it is expected to occur at a sufficiently low frequency, $\sim 2.5 \text{ mHz}$. The gravity gradiometer along the x-axis will be used to monitor gravitational disturbance of the experiment. The gravity noise from modulation of the Earth's gravity gradient and ISS self-gravity, including the activities of astronauts, will be taken out, along with the centrifugal acceleration, by the error compensation scheme.

Magnetic crosstalk. Trapped flux is not of concern as long as the flux is strongly pinned. Flux creep will be minimized by cooling and performing the experiment in a low magnetic field. For this purpose, LTMPF is equipped with a Cryoperm shield. Flux motion from the incidence of charged particles in orbit can be reduced by material processing and the insertion of flux dams.

ment will be $Q \approx 1.5 \times 10^{-13}$ C. In deriving this number, we used a charge trapping efficiency 10% that of STEP to account for the difference in shape: the ISLES test masses are extremely thin (250 μm) and do not trap charge as efficiently as the much thicker STEP test masses.

The charge trapped in the test mass will induce image charges on the neighboring coils and superconducting ground planes. Most of the trapped charge will appear on the surfaces of the test masses facing the shields since the gap is smallest there ($\sim 20 \mu\text{m}$). This will generate a differential force $Q^2/\epsilon_0 A$, where ϵ_0 is the permittivity of vacuum and A is the area of the test mass. The force results in the maximum differential displacement at the end of the mission:

$$x_{D,\text{max}} = \frac{Q^2}{\epsilon_0 A} \frac{1}{m \omega_D^2} \approx 7 \times 10^{-9} \text{ m}. \quad (4)$$

A differential displacement affects the CMRR through mismatches in the coil areas, gaps, and currents. With the initial coil gap of 10^{-4} m and a mismatch of 10%, we find that the CMRR is affected by 7 ppm at most. This should allow the passive CMRR to remain at the required level of 10^5 throughout the mission. So ISLES does not require a discharging system. To make sure that the trapped charge remains below the threshold, the charge will be measured after each 30-day data run and the test masses will be discharged, if necessary, by simply pushing it against the shields. This may necessitate a recalibration of the detector.

The energetic charged particles will also impart momentum and cause heating of the test masses. These effects were found to be less important than the electrostatic force for STEP. In addition, patch-effect potential will be modulated as charge builds up in the test masses, causing a time-varying acceleration. These ac disturbances occur mostly outside the signal band and therefore are averaged out. The Casimir force is not of concern for the present experiment where the gap between the masses is $\gg 1 \mu\text{m}$ (Lamoreaux, 1997).

Temperature noise. The modulation of the penetration depth of a superconductor with temperature and residual thermal expansion coefficients for different materials give rise to temperature sensitivity in a superconducting accelerometer. These occur through temperature gradients as well as mismatches in the accelerometers (Chan and Paik, 1987). From our experience with the SGG, however, this noise is expected to be negligible with the platform temperature stabilized to 5 μK .

Total errors. Table 2 combines all the errors for the two scenarios: one with feedback and the other with vibration isolation. To reduce the random noise to the levels listed, a 90-day integration was assumed. The vibration isolation approach does not reduce the total noise, but is worth considering because it greatly simplifies the detector design and operation. It allows the use of a slightly stiffer suspension, which will reduce the disturbances from the trapped charge. Therefore, we plan to have a trade study at the beginning of the flight definition phase, comparing the risks and benefits, and the costs of implementing these approaches.

Error Source	Error ($\times 10^{-18} \text{ m s}^{-2}$)	
	w/ feedback	w/ isolation
Metrology	15	15
Random	(90 days)	(90 days)
Intrinsic	25	39
ISS vibration	23	21
Gravity noise	< 1	< 1
Vibration coupling	< 1	< 1
Magnetic coupling	< 10	< 10
Electric charge	< 10	< 10
Other (30% margin)	33	41
Total	52	64

Table 2. Error budget.

7. Expected Resolution

By equating the noise with the expected Yukawa signal, we compute the minimum detectable $|a|$. Figure 1 shows the 1σ error plotted as a function of l for the feedback approach. The case with active isolation is very similar. The best resolution of ISLES is $|a| = 1 \times 10^{-5}$ at $l = 100 \mu\text{m} \sim 1 \text{ mm}$. ISLES will test the $1/r^2$ law with a resolution of 10^{-2} at $l = 10 \mu\text{m}$. Figure 1 shows that the string theory predicted violation with $R_2 \geq 5 \mu\text{m}$ will be detected and axions with strength 10 ~100 times below the maximum will be detected.

ISLES will use the SGG technology fully developed at the University of Maryland. The SGG has been used to perform a null test of Newton's law at a sensitivity ten times beyond that of the other methods at 1-meter distance (Moody and Paik, 1993). The instrument proposed for ISLES is very similar to the existing SGG. The experimental procedure and error analysis are also similar to those in the meter-scale $1/r^2$ law test, already carried out with the SGG.

For the modest cost of the ISS experiment, the scientific gain from ISLES is tremendous. ISLES constitutes a new test of General Relativity in the hitherto largely untested range and the first ever test of a prediction of string theory. The experiment will push the frontiers of searching for new weak forces by several orders of magnitude, with a potential to discover new particles.

The resolution of the experiment could be improved by reducing several errors. The metrology and density errors could be reduced by fabricating the source mass out of a crystalline material such as sapphire or quartz, which can be optically polished. The masses would then be coated with a thin layer of Nb to allow levitation. The intrinsic noise of the detector could be reduced by using a lower noise SQUID (as has already been developed for GP-B). The vibration noise can be improved by a few orders of magnitude by going to a free-flyer, which will allow much softer suspension of the test masses and thus higher instrument sensitivity. With these improvements, the resolution could be improved to $|a| \leq 10^{-6}$.

References

- Adelberger, E. G. *et al.* (1991), *Ann. Rev. Nucl. Part. Sci.* **41**, 269.
Arkani-Hamed, N., Dimopoulos, S., and Dvali, G. (1999), *Phys. Rev. D* **59**, 086004.
Blaser, J.-P. *et al.* (1996), *STEP (Satellite Test of the Equivalence Principle)*, Report on the Phase A Study, SCI(96)5.
Bendat, J. S. and Piersol, A. G. (1971), *Random Data: Analysis and Measurement Procedures* (Wiley, New York), Chapter 5.
Chan, H. A. and Paik, H. J. (1987), *Phys. Rev. D* **35**, 3551.
Cullen, S. and Perelstein, M. (1999), preprint hep-ph/9903422.
Hall, L. J. and Smith, D. (1999), *Phys. Rev. D* **60**, 085008.
Hannestad, S. and Raffelt, G. G. (2002), *Phys. Rev. Lett.* **88**, 071301.
Hoyle, C. D. *et al.* (2001), *Phys. Rev. Lett.* **86**, 1418.
Lamoreaux, S. K. (1997), *Phys. Rev. Lett.* **78**, 5.
Long, J. C. *et al.* (1999), *Nucl. Phys. B* **539**, 23.
Moody, M. V. and Paik, H. J. (1993), *Phys. Rev. Lett.* **70**, 1195.
Moody, M. V., Canavan E. R., and Paik, H. J. (2002), submitted to *Rev. Sci. Instrum.*
Peccei, R. D. and Quinn, H. (1977), *Phys. Rev. Lett.* **38**, 1440.
Rigby, K. W., Marek, D., and Chui, T. C. P. (1990), *Rev. Sci. Instr.* **2**, 834.
Turner, M. S. (1990), *Phys. Rep.* **197**, 67.
Weinberg, S. (1978), *Phys. Rev. Lett.* **40**, 223.
Wilczek, F. (1978), *Phys. Rev. Lett.* **40**, 279.

Test of the Equivalence Principle in an Einstein Elevator: highlights of the first-year progress report

I.I. Shapiro¹, E.C. Lorenzini^{1,*}, P. Cheimets¹, M.L. Cosmo¹, S. Glashow², V. Iafolla³,
C. Bombardelli⁴, and A. Turner⁵

¹Harvard-Smithsonian Center for Astrophysics (CfA); ²Boston University; ³Institute of Space Physics (Rome, Italy); ⁴University of Padova (Italy) and CfA Visiting Student; ⁵Harvard University. *Corresponding author e-mail: elorenzini@cfa.harvard.edu

Abstract

This paper presents the highlights of progress made in the flight definition of an experiment to test the Equivalence Principle in free-fall inside a co-moving vacuum chamber/cryostat. The chamber is part of the falling capsule which is released from a balloon at stratospheric altitude. The paper focuses on the study of key noise sources such as gravity gradients generated by distributed (capsule) and concentrated (equipment) masses near the sensor. The results have led to the choice of the capsule mass distribution and to the determination of requirements of relative motion between the sensor and the capsule. Furthermore, an analysis of the gravity gradient of the Earth as a function of the orientation of the sensor has defined the constraint on sensor attitude motion and centering errors between the centers of mass of the sensing masses.

Introduction

The scientific goal of the experiment is to test the equality of gravitational and inertial mass (i.e., to test the Principle of Equivalence) by measuring the independence of the rate of fall of bodies from the composition of the falling body. The measurement is accomplished by measuring the relative displacement (or equivalently acceleration) of two falling bodies of different materials which are the proof masses of a differential accelerometer. The goal of the experiment is to measure the Eötvös ratio $\delta g/g$ (differential acceleration/common acceleration) with an accuracy goal of a few parts in 10^{15} . The estimated accuracy is about two orders of magnitude better than the present state of the art^{i,ii}. The experiment is a null experiment in which a result different from zero will indicate a violation of the Equivalence Principle.

In summary, the experiment to be designed is aimed at taking differential acceleration measurements with a high-sensitivity detector (the sensor) during free fall conditions lasting up to 30 s in a disturbance-free acceleration environment. During the measurement phase, the sensor free falls inside a few-meter-long (in the vertical direction) evacuated capsule that is falling simultaneously in the rarefied atmosphere after release from a helium balloon flying at a stratospheric altitudeⁱⁱⁱ.

By falling in vacuum inside a co-moving capsule, the noise acceleration level can be kept to a negligible level while the signal strength in free fall is increased by 3 orders of magnitude with respect to the signals available to experiments conducted on the ground.

The free fall technique, therefore, combines some of the advantages of the space-based tests with the accessibility and reusability of ground experiments.

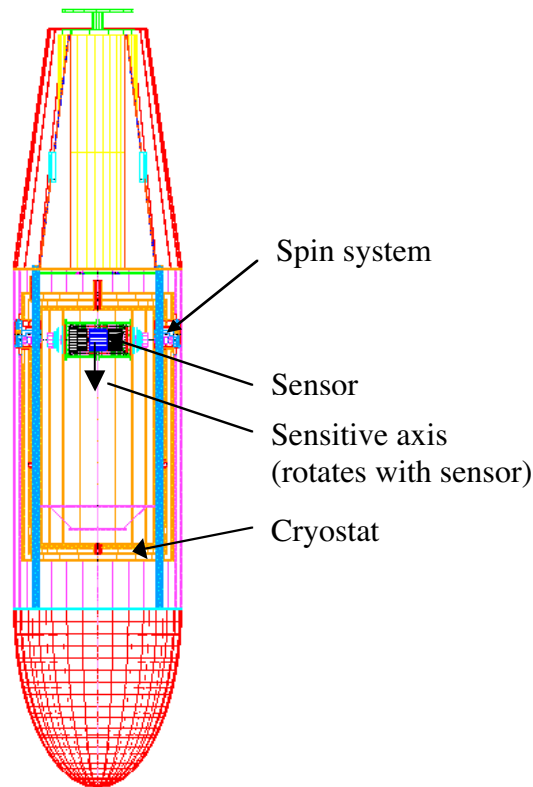


Fig. 1 Schematic of capsule with acceleration detector attached (before release) to the spin up system

Experiment Highlights

The experiment starts with the loading of the sensor into the vacuum chamber/cryostat about 2 weeks before the planned launch. This operation is then followed by the pumping down of the chamber and the refrigeration of the sensor. After connecting the capsule to the gondola and the balloon, the balloon is launched. The estimated time to reach altitude is about 3 hours. Upon reaching altitude, the attitude of the capsule is stabilized along the local vertical by the leveling mechanism on the gondola, the sensor is spun up, and the dynamics of the system is analyzed. When the dynamics is within the acceptable bounds, the capsule is released from the gondola and the sensor is released from the top of the chamber/cryostat immediately afterwards. The science data is taken during the free-fall phase in which the sensor spans the length of the chamber. Shortly after the sensor has reached the bottom of the capsule, a blut (first stage of the deceleration system) is released and, when the speed has decreased below the required value, the parachute is deployed. The chamber is vented before the capsule hits the surface/water and the locator beacon is turned on.

The differential accelerometer (sensor) detects the relative displacement, through capacitive pickups, of two sensing masses of different materials. The two sensing masses

have their centers of mass (CM) as close as possible in order to reduce the effect of gravity gradients and rotational dynamics.

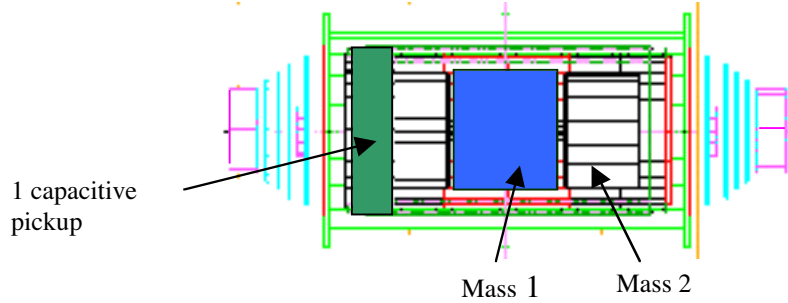


Fig. 2 Schematic of instrument package with exploded view of sensing masses

The differential accelerometer is slowly spun before release to modulate the signal during the measurement phase. The spin also moves some components of gravity gradients to a frequency higher than the signal frequency as shown in the next section. Figure 2 shows an exploded view of the instrument package (that hosts the sensor) with the two sensing masses in open view. The sensor is discussed in greater details in Refs. ^{iv v}. In this paper we will concentrate on the analysis of key perturbations affecting the measurement. Specifically, the effects of the gravity gradients produced by the distributed mass of the capsule, concentrated masses on board the capsule and the Earth's mass on the experiment design.

Analysis of Gravity Gradients

The gravity gradients generated by the distributed mass of the chamber/cryostat and their effects on the differential measurement are analyzed in the following for a generic position of the detector inside the capsule and a generic orientation of its spin axis with respect to the gradient field. For a mass distributed with cylindrical symmetry, the resultant gravitational acceleration has two components: a_z = acceleration component along the cylinder axis; and a_r = acceleration component along the cylinder radius.

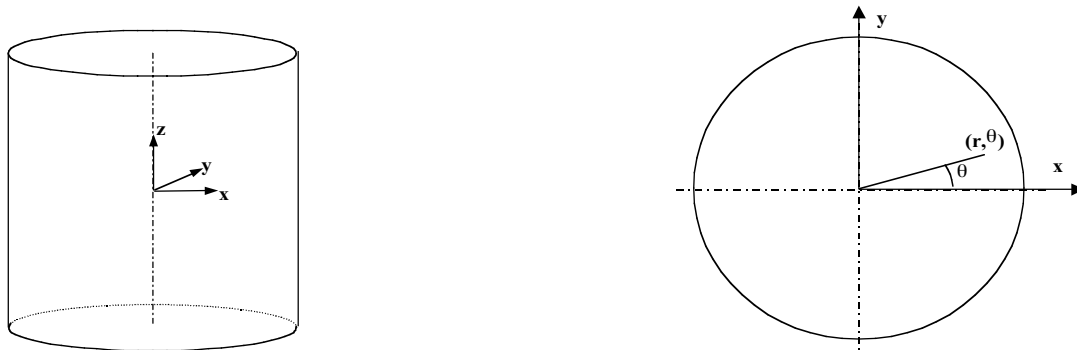


Fig. 3 Reference frames for gravity gradient analysis

After erecting a Cartesian reference system xyz as depicted in Figure 3, the components of the gravity gradient tensor are computed according to the following transformation formulas:

$$\begin{aligned} dx &= \cos(\theta) \cdot dr - r \cdot \sin(\theta) \cdot d\theta \\ dy &= \sin(\theta) \cdot dr + r \cdot \cos(\theta) \cdot d\theta \\ da_x &= \cos(\theta) \cdot da_r - a_r \cdot \sin(\theta) \cdot d\theta \\ da_y &= \sin(\theta) \cdot da_r + a_r \cdot \cos(\theta) \cdot d\theta \end{aligned} \quad (1)$$

Setting $\theta = 0$ and utilizing the cylindrical symmetry:

$$a_x = a_r$$

$$a_y = 0$$

and the gravity gradient components in cylindrical coordinates are

$$\begin{aligned} a_{xx} &= a_{rr} \\ a_{xy} &= 0 \\ a_{yy} &= a_r / r \\ a_{xz} &= a_{zx} = a_{rz} \\ a_{yz} &= a_{zy} = 0 \end{aligned} \quad (2)$$

in which the subscripts indicate spatial derivatives. The gravity gradient tensor takes the form:

$$\Gamma = \begin{bmatrix} a_{rr} & 0 & a_{rz} \\ 0 & a_r / r & 0 \\ a_{rz} & 0 & a_{zz} \end{bmatrix} \quad (3)$$

As a result of the Laplace equation, the trace of the gravity gradient tensor is equal to zero, that is

$$a_{rr} + a_r / r + a_{zz} = 0 \quad (4)$$

In the singular case of $r = 0$ the limit calculation yields:

$$\Gamma(r = 0) = \begin{bmatrix} a_{rr} & 0 & 0 \\ 0 & a_{rr} & 0 \\ 0 & 0 & -2a_{rr} \end{bmatrix} \quad (5)$$

Gravity gradient matrix of a rotating body

In general a gravity gradient matrix has the form:

$$\Gamma = \begin{bmatrix} \Gamma_{xx} & \Gamma_{xy} & \Gamma_{xz} \\ \Gamma_{yx} & \Gamma_{yy} & \Gamma_{yz} \\ \Gamma_{zx} & \Gamma_{yz} & \Gamma_{zz} \end{bmatrix} \quad (6)$$

The rotated matrix Γ' after a $\theta = \omega t$ rotation is:

$$\Gamma \odot = R_\theta \Gamma R_\theta^T \quad (7)$$

where R_θ is the rotation matrix and R_θ^T its transpose.

After a rotation about an axis (i.e., the x axis), the rotated matrix has four components modulated at ω , four components modulated at 2ω and one component that is not modulated.

The ω -modulated components of the transformed matrix (with superscript ') are:

$$\Gamma'_{12} = \Gamma'_{21} = \Gamma_{xz} \sin(\omega \cdot t) + \Gamma_{xy} \cos(\omega \cdot t) \quad (8.1)$$

$$\Gamma'_{13} = \Gamma'_{31} = \Gamma_{xz} \cos(\omega \cdot t) - \Gamma_{xy} \sin(\omega \cdot t) \quad (8.2)$$

where the transformed axes are called $x' = 1, y' = 2, z' = 3$. In summary, the *off-diagonal components* $\Gamma'_{12} = \Gamma'_{21}$ and $\Gamma'_{13} = \Gamma'_{31}$ of the gravity gradient matrix produce components that are *modulated at the rotation frequency*.

Gravity gradient matrix projected onto sensor body axes

In a general case the body reference frame placed at the CM of a sensing mass of the detector can be identified with respect to the cryostat frame by means of 3 successive rotations as follows:

- 1 - Rotation α around z axis (azimuth rotation)
- 2 - Rotation β around the transformed y' axis (elevation rotation)
- 3 - Rotation ωt around the transformed x'' axis (spin rotation)

In the computation of gravity gradients, these rotations can either be rotations of the sensing mass with respect to the cryostat or, equivalently, rotations of the cryostat with respect to the sensing mass. In the former case, and solely for the reason of pointing out a typical geometrical situation, the first and second rotations could, for example, be caused by the detector dynamics during free-fall (e.g., precession of its body axes) while

the third rotation is the ωt rotation of the detector about its longitudinal axis aimed at modulating the signal.

Clearly, we are mostly concerned about the components of the gravity gradient matrix that contain a frequency ω equal to the modulating frequency of the signal. We can choose the body axis $y' = 2$ to coincide with the sensitive axis of the accelerometer and, consequently, we are only concerned with the component Γ'_{21} of eqn. (8.1). In general, the moduli of the two components Γ'_{12} and Γ'_{13} are the same and they can be written as follows:

$$\chi = \sqrt{\Gamma_{xy}^2 + \Gamma_{xz}^2} \quad (9)$$

After rotating the original matrix by two rotations α and β (where α is the azimuth of the spin axis with respect to the radial direction and β is the elevation with respect to the capsule equatorial plane) the expressions of Γ_{xy} and Γ_{xz} in eqn. (9) are as follows

$$\Gamma_{xy} = k_1 \sin(\beta) \sin(\alpha) - k_2 \cos(\beta) \sin(2\alpha) \quad (10.1)$$

$$\Gamma_{xz} = k_3 \sin(2\beta) + k_1 \cos(\alpha) \cos(2\beta) + k_2 \sin(2\beta) \cos^2(\alpha) \quad (10.2)$$

$$k_1 = a_{xz} \quad (10.3)$$

$$k_2 = \frac{1}{2}(a_{xx} - a_{yy}) \quad (10.4)$$

$$k_3 = \frac{1}{2}(a_{yy} - a_{zz}) \quad (10.5)$$

where the a_{ij} are the matrix components before the rotations are carried out. In the case of a body with cylindrical symmetry and for cylindrical coordinates, eqns. (2) yield $a_{xx} = a_{rr}$, $a_{yy} = a_r/r$, $a_{zz} = a_{zz}$, $a_{xz} = a_{rz}$ while the other components are null.

Using numerical analysis of eqns. (10) and taking into account that inside a cylinder k_2 is always at least one order of magnitude less than k_1 and k_3 , we find that the maximum value for χ occurs for $\alpha = 0$. This result implies that the maximum disturbance of the capsule gravity field on the differential accelerometer is produced when the capsule moves radially with respect to the sensor (see Figure 4) in such a way that the spin axis is oriented along the radius of the cylinder through the sensor and the capsule has been displaced radially with respect to the sensor (e.g., by wind shear).

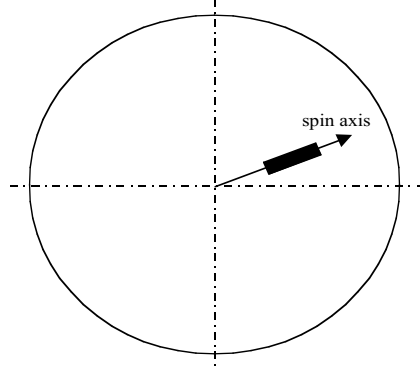


Figure 4 Geometry of sensor and capsule (viewed from the top) for strongest gravity gradient affecting the measurement

On the opposite end, if the motion of the capsule is such as to keep α close to 90° , that is the spin axis is orthogonal to the radial, the disturbance is minimum. Nevertheless, since the translational motion of the external capsule is not predictable nor controlled, the worst condition is analyzed by setting α equal to zero and varying the angle β , so that eqns. (9) and (10) yield:

$$\chi = (k_3 + k_2) \sin(2\beta) + k_1 \cos(2\beta) \quad (11)$$

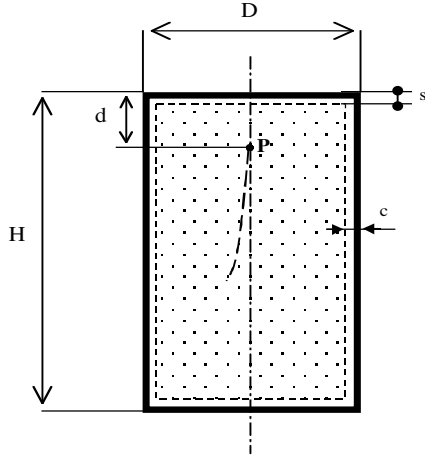
Equation (11) summarizes the disturbances induced by the cryostat mass modulated at the measurement frequency. This equation is important for the cryostat/capsule design.

Capsule gravity gradients

The gravity gradient terms (which are in turn combinations of gravity gradient tensor components) have a complex distribution inside the cryostat. During free fall, the capsule/cryostat moves with respect to the sensor because of the external forces produced by the rarefied atmosphere. The sensor spans the top 1-m vertical distance inside the cryostat in 20-25 s for a capsule ballistic coefficient in the range of interest of 6000-10000 kg/m². Under worst-case conditions of wind shear the side motion relative to the capsule is limited to a cylindrical area of 0.1-m radius centered about the longitudinal axis of the cryostat. An additional contribution to the side motion is due to the verticality error of the capsule during the fall.

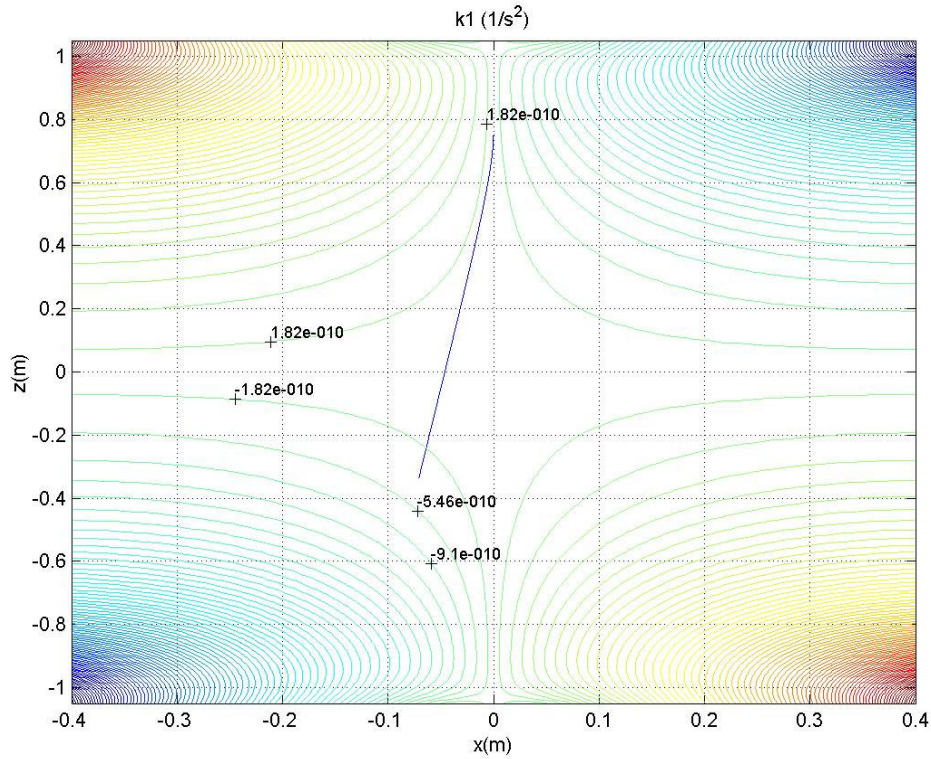
A Matlab routine was developed to compute the gravity gradients inside a cylindrical cryostat with caps of different shapes. The routine creates a two-dimensional mesh of point masses uniformly distributed on the average surface of the cylinder and its caps. In the case of flat caps the mass distribution results in a closed cylindrical surface of height H and diameter D . The gravity gradient field has been mapped on the z - x plane where x coincides with the cylinder's radial and z with the longitudinal axis, as far as $s = 10$ cm from the top and bottom and $c = 20$ cm from the side walls.

The point of release P lies on the symmetry axis of the cylinder and at $d = 40$ cm from the top. A worst-case relative trajectory of the sensor inside the cryostat was computed (see

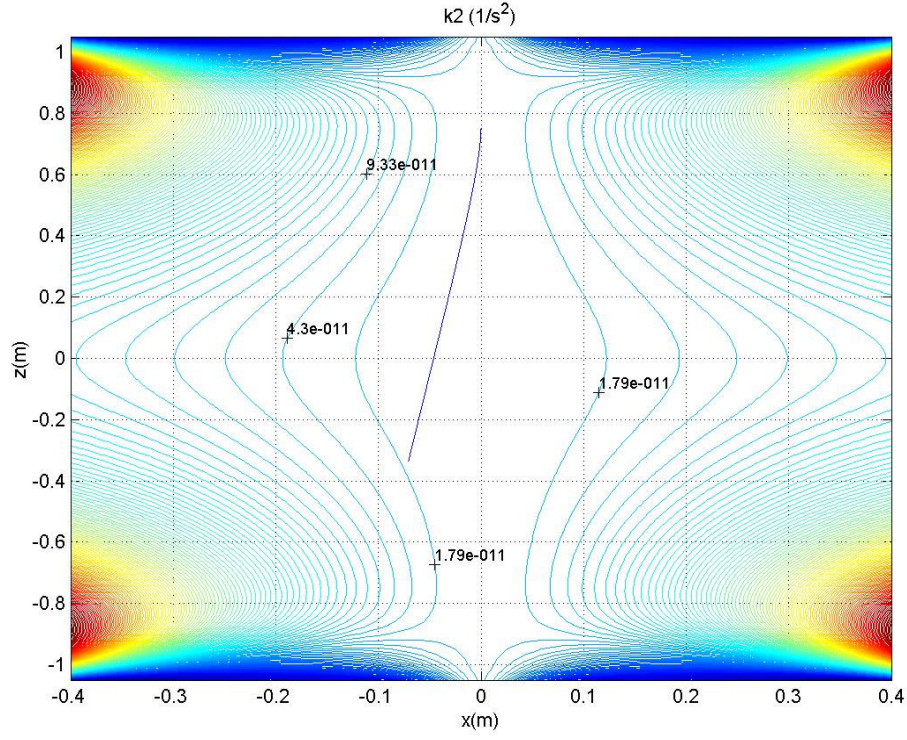


Ref. v) for our current best estimate of the capsule parameters as follows: ballistic coefficient (at low speed) = 10000 kg/m^2 , a release altitude of 40 km, a wind shear of 0.005 s^{-1} (i.e., 10 knots/km) and a maximum verticality error of the capsule of 5° which has been conservatively assumed to produce a constant, lateral displacement of the sensor in the same direction of the wind shear. This worst-case trajectory is superimposed to the contour plots of the relevant gravity gradient terms k_1 , k_2 and k_3 shown in Figs. 5(a)-5(c).

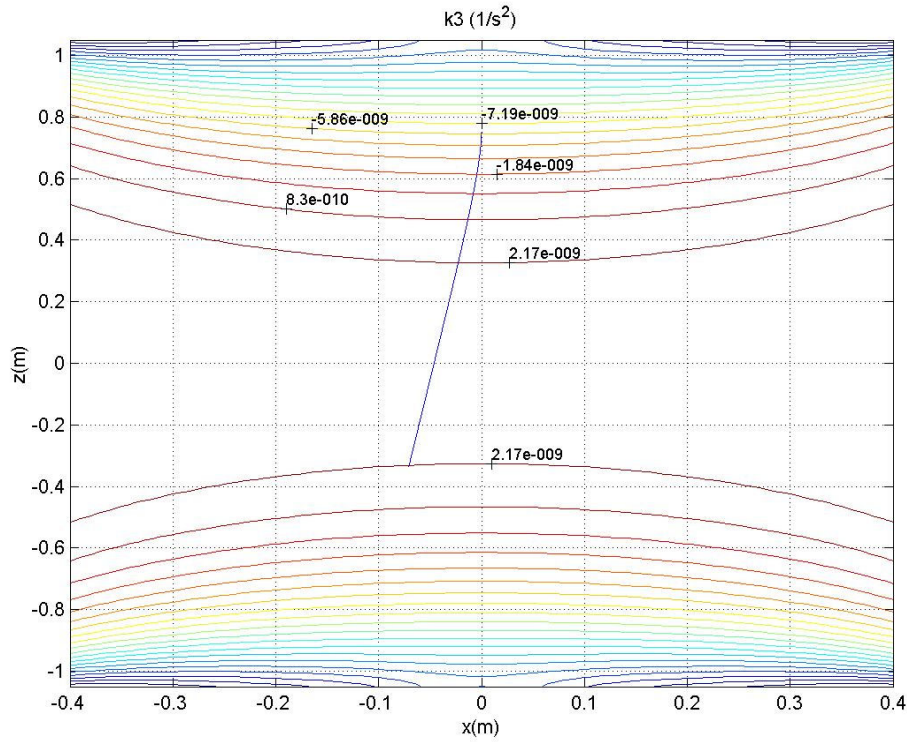
The detector senses the gravity gradient components as a differential acceleration if there is a centering error of the two proof masses. The gravity gradient terms shown in Figs. 5 are those modulated at the sensor rotation frequency ω and, consequently, they are the most damaging gravity gradient components.



(a)



(b)



(c)

Figure 5 Contour plots of gravity gradient terms for a cryostat with flat caps and $H = 2.3$ m, $D = 1.2$ m and total mass = 500 kg: (a) k_1 ; (b) k_2 and (c) k_3 . [see eqns. (10)]

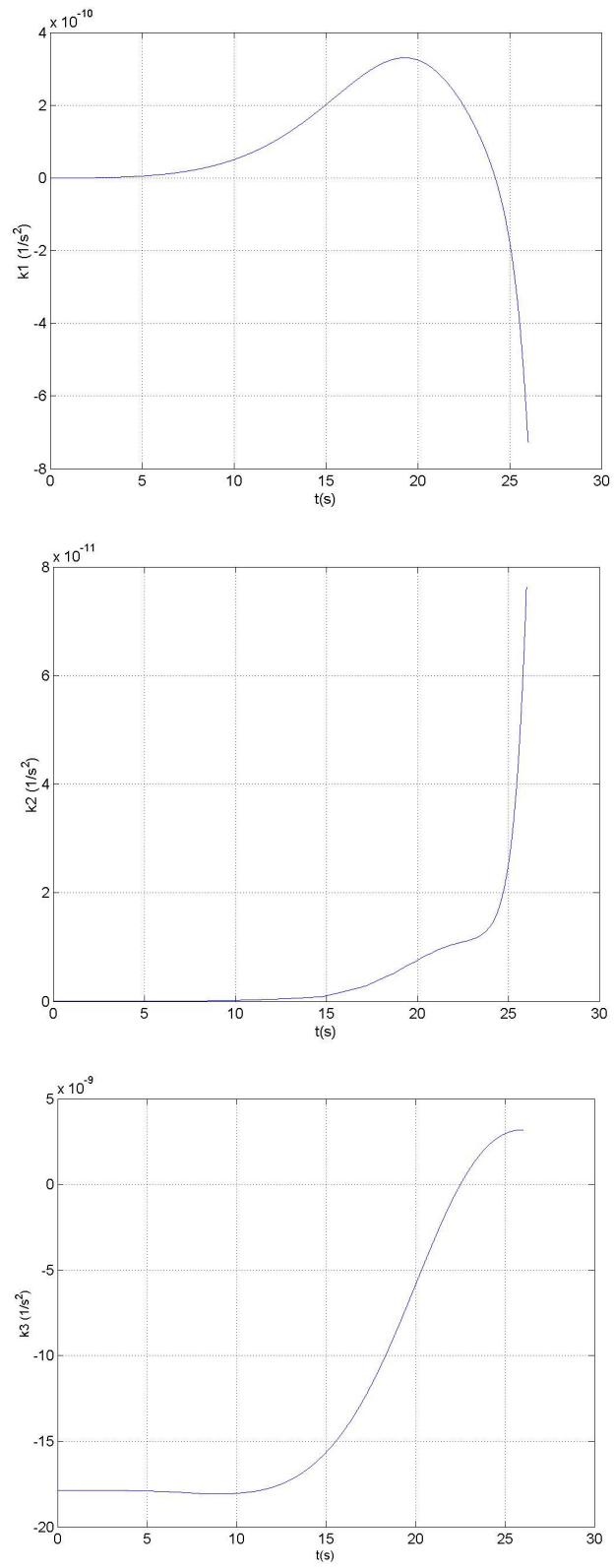


Fig. 6 Values of k_1, k_2, k_3 vs. time along the fall trajectory

Figure 6 shows that the quantity k_3 is relatively larger than k_1 and k_2 . Consequently, eqn. (11) poses a limit for the angle β that defines the capsule attitude with respect to the spin axis of the sensor. After neglecting the much smaller k_2 (and k_1 which depends on $\cos(2\beta)$) we find that the maximum allowable β is:

$$\beta_{\max} = \frac{1}{2} \sin^{-1} \left(\frac{\chi_{\max}}{k_3} \right) \quad (12)$$

With a χ_{\max} of 10^{-9} s^{-2} and the results shown in Fig. (6), we obtain a limit of 4.8 deg for β , which is consistent with the maximum tilt assumed for the capsule in computing the worst-case relative trajectory.

Earth's gravity gradients

We compute here the Earth's gravity gradient tensor and we analyze the effects of Earth's gravity gradient components on a rotating detector with a generic orientation of its spin axis with respect to the gravity gradient field. Let us consider the gravitational potential per unit mass at a point (x, y, z) with respect to the detector's center of mass:

$$V = - \frac{\mu}{\sqrt{(x - R_X)^2 + (y - R_Y)^2 + (z - R_Z)^2}} \quad (13)$$

where R_X, R_Y, R_Z are the components of the radius vector R from the Earth's center to the detector's CM (in which Z is the local vertical) and μ is the Earth's gravitational constant. After projecting about the detector's body axes in which x is the spin axis and calling $\theta = \omega t$ the rotation about the spin axis and ϕ the elevation angle of the spin axis with respect to the horizontal plane:

$$\begin{aligned} R_x &= R(t) \sin(\phi) \\ R_y &= R(t) \cos(\phi) \sin(\omega t) \\ R_z &= R(t) \cos(\phi) \cos(\omega t) \end{aligned} \quad (14)$$

The gravitational acceleration in body axes is obtained by substituting eqns (14) into eqn. (13) and computing the gradient to obtain:

$$g_{xx} = - \frac{\mu}{R^3} [-2 + 3 \cos^2(\phi)] \quad (15.1)$$

$$g_{xy} = 3 \frac{\mu}{R^3} \sin(\omega t) \cos(\phi) \sin(\phi) \quad (15.2)$$

$$g_{xz} = 3 \frac{\mu}{R^3} \cos(\omega t) \cos(\phi) \sin(\phi) \quad (15.3)$$

$$g_{yy} = - \frac{\mu}{R^3} [1 - 3 \cos^2(\phi) + 3 \cos^2(\omega t) \cos^2(\phi)] \quad (15.4)$$

$$g_{yz} = 3 \frac{\mu}{R^3} \cos(\omega t) \sin(\omega t) \cos^2(\phi) \quad (15.5)$$

$$g_{zz} = \frac{\mu}{R^3} [-1 + 3\cos^2(\omega t)\cos^2(\phi)] \quad (15.6)$$

Here again, the components modulated at ω are g_{xy} and g_{xz} (in which x is the spin axis). In other words, if the spin axis lies on the horizontal plane, the detector only sees components modulated at 2ω but if it is not, components modulated at the frequency ω appear. The strengths of these components are proportional to the tilt angle with respect to the horizontal plane. Note also that the effect of the Earth's gravity gradient on a rotating body can be readily applied to the space-based tests of the Equivalence Principle in which the only difference from the balloon-based experiment is the slightly larger value of the radial distance from the space-based sensor to the Earth's center.

Since there are terms modulated at the signal frequency ω , we have to make sure that they are kept lower than the accuracy with which we want to measure the signal. From the detector point of view, there will be requirements imposed on the centering of the sensing masses and their attitude with respect to the Earth's gravity field as shown in the following section.

Gravity gradients produced by concentrated masses on board the capsule

Let us consider the reference system (x, y, z) attached to the sensor with origin at the center of mass and with x oriented along the spin axis and let us indicate the position of a point mass m_p in proximity of the sensor in spherical coordinates (δ, γ, ρ) (see Fig. 7).

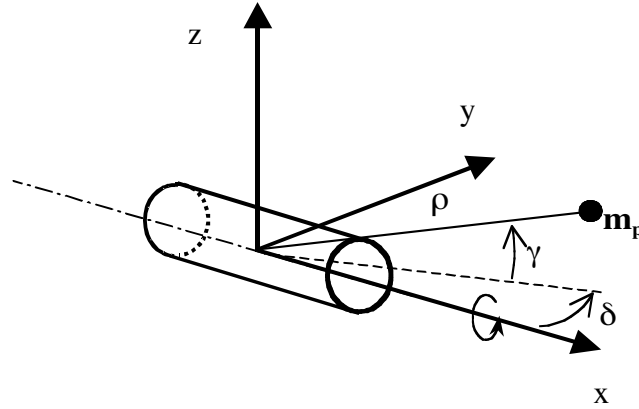


Fig. 7 Geometry of the sensing mass and reference frame

The position of m_p is then expressed as:

$$\begin{aligned} x_p &= \rho \cos \delta \cos \gamma \\ y_p &= \rho \sin \delta \cos \gamma \\ z_p &= \rho \sin \gamma \end{aligned} \quad (16)$$

The gravity gradient matrix at the detector due to the gravity field induced by a mass point m_p is:

$$\Gamma_{m_p} = \frac{G \cdot m_p}{\rho^5} \begin{bmatrix} 3x^2 - \rho^2 & 3xy & 3xz \\ 3yx & 3x^2 - \rho^2 & 3yz \\ 3zx & 3yz & 3x^2 - \rho^2 \end{bmatrix} \quad (17)$$

Considering a sensor that rotates with respect to a fixed point mass in its proximity we obtain the two ω -modulated components already shown in the previous paragraphs:

$$\Gamma'_{12} = \Gamma'_{21} = \Gamma_{xz} \sin(\omega \cdot t) + \Gamma_{xy} \cos(\omega \cdot t) \quad (18.1)$$

$$\Gamma'_{13} = \Gamma'_{31} = \Gamma_{xz} \sin(\omega \cdot t) - \Gamma_{xy} \cos(\omega \cdot t) \quad (18.2)$$

The moduli of the two ω -modulated gravity gradient components Γ'_{12} and Γ'_{13} are the same and can be expressed as follows:

$$\chi = \frac{G \cdot m_p}{\rho^5} |x| \sqrt{z^2 + y^2} \quad (19)$$

which shows that the masses located on the plane y-z (i.e., $x = 0$) do not generate disturbances with the same frequency as the measured signal.

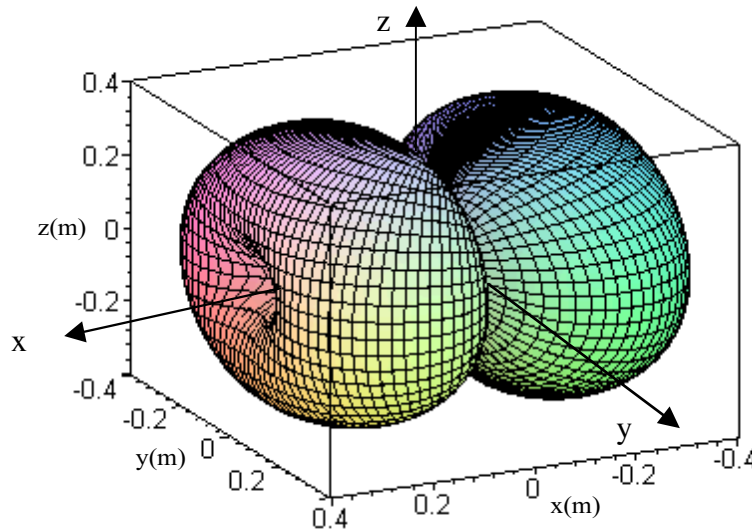


Fig. 8 Locus of ω -modulated gravity gradient component with strength = 10^{-9} s^{-2}

Substituting eqn. (16) into (19) and extracting ρ yields the minimum distance for a point mass to produce a disturbing gradient equal to or less than a critical value $a_{\text{gg-max}}$:

$$\rho_{\min} = \left(\frac{G \cdot m_p}{a_{gg-\max}} |\cos \delta \cos \gamma| \sqrt{\sin^2 \delta \cos^2 \gamma + \sin^2 \gamma} \right)^{1/3} \quad (20)$$

Setting a limit of 10^{-9} s^{-2} for a_{\max} we plot the locus $f(\rho, \gamma, \delta) = 0$ of the points in space with $a_{gg} = a_{gg-\max}$ in Fig. 8 for a disturbing point mass of 1 kg. Meridian sections (rotated about the z -axis by the meridian angle δ) of the same locus are plotted for different values of the angle δ in Fig. 9 where r is the radial direction.

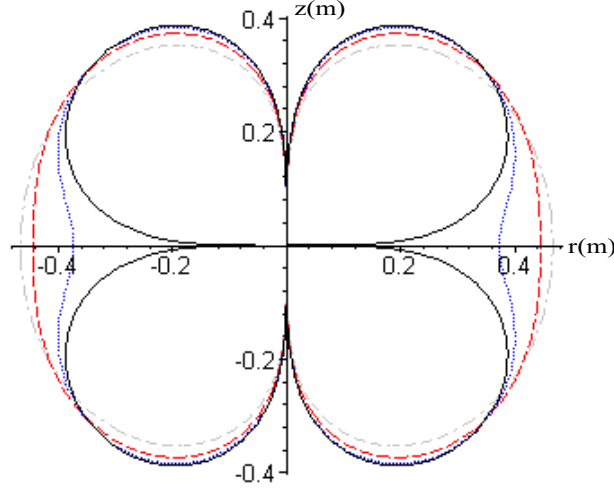


Fig. 9 Meridian sections of locus in Fig. 8 for different angles δ [$\delta = 0$ (i.e., y - z plane) - solid black line; $\delta = 15^\circ$ - blue dots; $\delta = 30^\circ$ - red dash; $\delta = 45^\circ$ - gray dash dot]

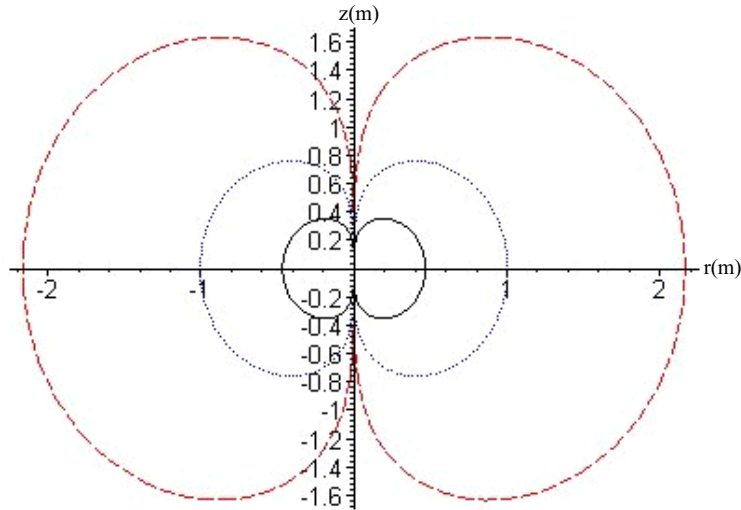


Fig. 10 Meridian sections for $\delta = 45^\circ$ and different values of perturbing mass m_p ($m_p = 1 \text{ kg}$ - solid black line; $m_p = 10 \text{ kg}$ - blue dots; $m_p = 100 \text{ kg}$ - red dash)

The worst case meridian section at $\delta = 45^\circ$ is plotted for different values of the perturbing mass in Fig. 10. The previous analysis defines exclusion zones for concentrated masses on board the capsule. In general, masses can be placed rather freely on the y-z plane (perpendicular to the sensor spin axis). Masses lying on this plane generate only 2ω -modulated components whose strength only needs to be reasonably smaller than the upper bound of the dynamic range of the sensor. The Earth itself produces such 2ω -modulated components with a strength equal to $3 \times 10^{-6} \text{ s}^{-2}$. For the 2ω -modulated term, the equivalent Earth is a mass of 22,500 kg at 1-m or a 22.5 kg at 10 cm from the sensor.

Requirements related to the ω -modulated components are more stringent and, consequently, we will concentrate on these components which have been dealt with in this analysis. In summary, concentrated masses should be placed as close as possible to the y-z plane (perpendicular to the sensor spin axis). For masses away from the y-z plane, Fig. 10 defines the exclusion zones from the sensor for different mass values under the worst possible condition of masses placed on the 45° meridian plane.

Effect of Gravity Gradients on Differential Acceleration Measurement

The differential accelerometer consists (from the mechanical point of view) of two sensing masses with ideally coincident centers of mass (CM). The equivalence violation signal is measured as a differential displacement along the y-body axis of the sensor which is orthogonal to the spin axis (i.e., the x-body axis). In reality the two centers of mass (or more appropriately centers of gravity) do not coincide and CM_2 (i.e., the CM of mass 2) is displaced by a position error vector δ with respect to CM_1 as follows

$$\delta = \begin{bmatrix} \delta_x \\ \delta_y \\ \delta_z \end{bmatrix} \quad (21)$$

We can place the body reference frame at CM_1 and compute the differential acceleration due to gravity gradients by simply multiplying the gravity gradient matrix in body axis, that is

$$\begin{bmatrix} \delta a_x \\ \delta a_y \\ \delta a_z \end{bmatrix} = \left(\Gamma^E + \Gamma^C + \Gamma^M \right) \begin{bmatrix} \delta_x \\ \delta_y \\ \delta_z \end{bmatrix} \quad (22)$$

where Γ^E , Γ^C , Γ^M are the gravity gradient matrices of the Earth, the distributed capsule mass and concentrated masses on board the capsule, respectively. Since the differential accelerometer measures only the component along the y-body axis, we obtain finally:

$$\delta a_y = (\Gamma_{yx}^E + \Gamma_{yx}^C + \Gamma_{yx}^M) \delta_x + (\Gamma_{yy}^E + \Gamma_{yy}^C + \Gamma_{yy}^M) \delta_y + (\Gamma_{yz}^E + \Gamma_{yz}^C + \Gamma_{yz}^M) \delta_z \quad (23)$$

in which Γ_{yx}^E , Γ_{yx}^C , and Γ_{yx}^M are the components modulated at the signal frequency ω while the other terms in eqn. (23) are modulated at 2ω . In conclusion, the disturbing differential acceleration along y produced by gravity gradients can be expressed as follows:

$$\begin{aligned} \delta a_y < 3 \frac{\mu}{R^3} \cos(\phi) \sin(\phi) \sin(\omega t) \delta_x + [(k_2 + k_3) \sin(2\beta) + k_1 \cos(2\beta)] \sin(\omega t) \delta_x \\ + a_M(\omega) + f_y(2\omega, \delta_y) + f_z(2\omega, \delta_z) \end{aligned} \quad (24)$$

where k_1 , k_2 , and k_3 are the gravity gradient terms (see previous subsections) generated by the capsule in the capsule-body reference frame, ϕ is the elevation of the spin axis with respect to the local horizon, β is the elevation of the spin axis with respect to the equatorial plane of the capsule, $a_M(\omega)$ is the ω -modulated disturbing acceleration (in functional form) produced by concentrated mass on board the capsule (see previous subsection) and $f_y(2\omega, \delta_y)$ and $f_z(2\omega, \delta_z)$ represent all the other 2ω -modulated components which have been separated in eqn. (24) according to the centering error components. Note that the 2ω -components depend only on the centering errors δ_y and δ_z while the ω -components depend only on the centering error δ_x . The less-than sign in eqn. (24) is due to the fact that, on the right hand side of the equation, we have adopted the strongest value of the ω -modulated gravity gradient component of the capsule, that is, for $\alpha = 0$ (see Fig. 4). Moreover, from the analysis of the capsule gravity gradients, we have concluded that if we keep the sensor (at the CM) about 40 cm away from the heavy part of the chamber/cryostat walls, the ω -modulated gravity gradients are well below the critical value of about 10^{-9} s^{-2} . Based on similar reasoning, we assume that the concentrated masses on board the capsule are placed outside of the exclusion zones (defined in the previous subsection) in order to keep them below the critical value. In other words, an appropriate design and a careful mechanical construction of the sensing masses (δ_x of order microns) will make the gravity gradient contribution of the capsule and the concentrated masses on board the capsule negligible.

To attenuate the effect of the gravity gradient of the Earth we have to make sure that the product $\sin(\phi)\cos(\phi)\delta_x$ is sufficiently small. In other words we can trade the position error δ_x between the CMs of the sensing masses along the spin axis for the tolerable angle ϕ of the spin axis with respect to the local horizontal. For small values of ϕ , we readily compute that for the first term on the right hand side of eqn. (15.3) to be smaller than, let us say, 10^{-15} g , the product $\phi\delta_x$ must be smaller than $0.1 \text{ deg-}\mu\text{m}$. This requirement must be considered in the design of the detector, the release mechanism, and the capsule leveling system. The complexity of some subsystems can be traded for the simplicity of other subsystems among those three.

Conclusions

The paper focuses on the highlights of the analysis of the effects of gravity gradients produced by distributed masses (capsule/cryostat), concentrated masses (equipment) and the Earth's mass. The results obtained are important for defining: (a) the size of the

cryostat in which the detector free falls; (b) the exclusion zones where heavy equipment should not be placed on board the capsule; and (c) the tolerable tilt of the sensor spin axis with respect to the horizontal plane versus the centering error of the centers of mass of the sensing masses.

Acknowledgements

This work was supported by NASA grant NAG8-1780 with Donald Strayer from the Jet Propulsion laboratory as project scientist and Dorothy Hubbard at NASA Marshall Space Flight Center as technical officer.

References

-
- ⁱ Williams, J.G., X.X. Newhall and J.O. Dickey (1996), Relativity parameters determined from lunar laser ranging, *Phys. Rev. D*, 53, 6730.
 - ⁱⁱ Baessler S., Heckel B., Adelberger, E. Gundlack J., Schmidt U. and Swanson E. (1 Nov. 1999), *Phys Rev Lett.*, Vol. 83.
 - ⁱⁱⁱ Lorenzini, E.C., I.I. Shapiro, F. Fuligni, V. Iafolla, M.L. Cosmo, M.D. Grossi, P.N. Cheimets and J.B. Zielinski, "Test of the Weak-Equivalence Principle in an Einstein Elevator." *Il Nuovo Cimento*, Vol. 109B, No. 11, 1994.
 - ^{iv} Shapiro, I.I., S. Glashow, E.C. Lorenzini, M.L. Cosmo, P.N. Cheimets, V. Iafolla, M. Schneps, and N. Finkelstein, "Flight definition of an experiment to test the Equivalence Principle in an Einstein Elevator." *Procs. of 2nd Pan Pacific Basin Workshop on Microgravity Sciences*, Paper FP-1080, Pasadena, CA, May 2001.
 - ^v Shapiro, I.I. et al. "Test of the Equivalence Principle in an Einstein Elevator." *Annual Report #1, NASA Grant NAG8-1780, Smithsonian Astrophysical Observatory*, May 2002.

Implications of an Accurate Measurement by a SEE Mission of the Rate of Change of the Gravitational Constant

A.J. Sanders*, A.D. Alexeev**, K.A. Bronnikov**, G.T. Gillies***, V.D. Ivashchuk**, N.I. Kolosnitsyn**, M.Yu. Konstantinov**, V.N. Melnikov**, and L.L. Smalley****

* University of Tennessee, also Oak Ridge National Laboratory, USA

** Russian Gravitational Society, Moscow

*** University of Virginia, USA

**** University of Alabama, Huntsville, USA

Abstract

The much-improved accuracy of \dot{G} expected from SEE mission makes it realistic to speak in terms of a *measurement* of \dot{G} , rather than an improvement in the upper bound on $|\dot{G}|$. The design goal for the SEE Mission is to be able to measure $(\dot{G})/G$ to within 1 part in 10^{14} . This accuracy is expected to be sufficient to observe effects predicted by extra-dimension theories and, hence, to discriminate among different models.

1. Introduction

A measurement of \dot{G} can provide one of the very few ways of using experiment to discriminate among the various multidimensional theories (see, for example, Marciano, 1984; Damour, Gibbons & Taylor, 1988; Ivashchuk & Melnikov, 1988; Bronnikov, Ivashchuk & Melnikov, 1988; Melnikov, 1994; Drinkwater *et al.* 1999; and Ivashchuk & Melnikov, 2000). There has never been a laboratory measurement of \dot{G} (using test masses in a controlled situation) at cosmologically interesting levels of precision. Attempts have been made to do so, but the extreme difficulty of such an undertaking has prevented even the best of the terrestrial experiments from reaching the presently foreseen requirements for testing theories. The current observational—*vis-à-vis* experimental—evidence regarding \dot{G} reveals scattered results (Gillies, 1997). A SEE mission (Sanders & Deeds, 1992; Alexeev *et al.*, 1993; Bronnikov *et al.*, 1993; Alexeev *et al.*, 1994; Sanders & Gillies, 1996; Sanders *et al.*, 1997; Israelsson, Lee & Sanders, 1999; Sanders *et al.*, 1999; Sanders *et al.*, 2000; Alexeev *et al.*, 2001), on the other hand, may hold promise of providing a *controlled* experiment with test masses which, via their use in space, have the potential to provide very fine accuracy, thus perhaps making it possible for the first time to discriminate among various possible unified theories.

The capability for making such accurate measurements of \dot{G} will require the successful handling of a host of potential perturbations (Sanders *et al.*, 2000). For example, we have found ways to drastically reduce the effective drag on test bodies within a satellite. The SEE concept of “Almost Zero Time-Averaged Drag” relies on focusing on *test bodies*, in contrast to the original Lange-APL concept, which focused on the satellite as a whole rather than the test bodies (Lange, 1964; Staffs, 1974). The result of this is that drag is predicted to be $\sim 10^{-18}$ g, which if achieved would be about 6 orders of magnitude lower than in any previous or planned space mission.

Most of the current promising approaches to unification theory, including string theories, p-brane theories, and supergravity, incorporate the gravitational force at a fundamental level. Although a number of different theoretical schemes have been proposed, a lack of precise experimental evidence presently makes it almost impossible to assess the validity of alternative schemes. Gravitation is the missing link in efforts to achieve a satisfactory unification theory of physics. The very precise experimental data which would be sought via a SEE mission could thus be key for advancing the prospects of unification theory.

In any case, it would be of great scientific value to demonstrate unequivocally that a fundamental “constant” of Nature is not constant; almost nothing could do more to invigorate interest in the

new theories, most of which do in fact predict time variation of G and other fundamental "constants."

A finding of non-zero $G\text{-dot}$ would at the very least require revision of general relativity, since it assumes a constant value of G . More broadly, this would clearly mark the boundaries where general relativity is valid, and specify the onset of new physics.

2. Objectives of a SEE Mission

The SEE mission has six measurement goals:

- 1) Measure the value of $G\text{-dot}$, the time derivative of G .
- 2) Test for violation of the Inverse-Square-Law (ISL) at distances on the order of meters.
- 3) Test for ISL violation at distances on the order of the radius of the Earth (R_E).
- 4) absolute value of the Gravitational constant G .
- 5) Test for violation of the Weak Equivalence-Principle (WEP)—i.e., for composition-dependent violations—at distances on the order of meters.
- 6) Test for WEP violations at distances on the order of R_E .

The targeted design accuracies for the SEE mission are shown in Table 1. In this paper we focus on the $G\text{-dot}$ component of the mission.

3. Expected Significance of a SEE Mission

The general focus of the SEE Mission is one of advancing the experimental base required for testing unification theories. As such, SEE is being designed to substantially increase the precision and

accuracy of measurement of $G\text{-dot}$, since it is likely to be decisive in discriminating among modern theories, which are expected to make predictions in the range

$$\sim 10^{-13}/\text{yr} < |G\text{-dot}|/G < \sim 10^{-11}/\text{yr}.$$

The recent discovery that the expansion of the Universe seems to be accelerating—rather than decelerating, as previously expected (Garnavich *et al.* 1998a; Garnavich *et al.* 1998b; Riess *et al.*; Perlmutter *et al.*, 1998)—raises fundamental questions about the structure of space-time and about the possible existence of some form of "Dark Energy," or "quintessence" (Caldwell, Dave, & Steinhardt, 1997). The need to have experimental windows opened on these questions and, hence, on cosmology and unification theory, is one of the strongest motivating factors underlying the design of the SEE Mission. The very precise experimental data that will be sought during the course of a SEE interaction will, for instance, be aimed at revealing the role that gravity plays in cosmologies that incorporate quintessence.

Therefore, we expect that the SEE mission results will either:

- give extremely accurate confirmation of presently-accepted theories, or
- indicate violations of them, while suggesting the direction of necessary changes.

4. Calculations of Secular Change in G

A striking feature of recent theories of quantum gravity and string theory is that they cannot retain a constant G , but rather require various secular rates of change. The assumption that the "coupling constant" G is actually constant is not consistent

Table 1: Expected Accuracy of SEE Tests and Measurements

$(G\text{-dot})/G$	$\sim 10^{-14}/\text{yr}$ in one year	1,000 times better than current bound; likely to discriminate against most modern theories
ISL at \sim few meters	2×10^{-7}	1,000 to 10,000 times better than current bound
ISL at $\sim R_E$	1×10^{-10}	100 times better than current bound
G	0.33 ppm (330 ppb)	100 times more precise in single day than ground-based experiment in months
WEP at \sim few meters	$< 10^{-7}$ ($\square \square < 10^{-4}$)	Moderately better than ground-based experiments
WEP at $\sim R_E$	$< 10^{-16}$ ($\square \square < 10^{-13}$)	1,000 to 10,000 better than current bound but 100 times weaker than STEP

with these unification theories.

Moreover, the rate of deceleration or acceleration of the Universe is closely linked with the value of $G\text{-dot}$, and the form of the linkage is very model-dependent. The measurement of $G\text{-dot}$ on a SEE mission will be sufficiently accurate that it will place severe constraints on how the Universe is evolving by showing that there is a very narrow range of allowed combinations of (1) the value of the acceleration and (2) viable forms of unification theory.

We have calculated the values of $(G\text{-dot})/G$ under various assumptions (Melnikov *et al.*, 2002). Two important cases are (a) 10-dimensional supergravity (p-brane theory requires 10 or 11 dimensions; see, for example, Overduin & Wesson, 1997) and (b) scalar-tensor (S-T) cosmologies (of which Brans-Dicke theory is a special case). We find that a 10-dimensional cosmology with two-component anisotropic fluid and positive acceleration (negative “deceleration parameter” q) leads to

$$(G\text{-dot})/G \approx -4 \times 10^{-12}/\text{yr}. \quad (1)$$

Observational data indicates that q is negative—i.e., the expansion rate is increasing rather than decreasing, as previously expected. A key question in modern cosmology is the nature of the so-called “dark energy” and the field resulting from it which could cause this acceleration.

Smaller values of $(G\text{-dot})/G$ are obtained from scalar-tensor cosmologies (see Figure 1). The expression for $G\text{-dot}$ in this case is

$$\Box g^2 + g - q' = 0 \quad (2)$$

where g is the ratio of $(G\text{-dot})/G$ to the Hubble rate H . The results are sensitive to the S-T parameter \Box , which is very large ($\Box > 2500$) because it is the ratio of the tensor to the scalar amplitudes, and general relativity is so nearly correct. (If the metric were pure tensor, as in general relativity, \Box would be infinite.) The results for $(G\text{-dot})/G$ are also very sensitive to the value assumed for the deceleration parameter q . More particularly, the result depends critically on the related parameter, $q' \approx 1.1 + q$. If $q' = 0$, we find

$$|G\text{-dot}|/G < 3 \times 10^{-14}/\text{yr} \quad (3)$$

However, if we choose the largest value of q' consistent with observations, viz. $q' = 0.4$, we find:

$$|G\text{-dot}|/G < 0.9 \times 10^{-12}/\text{yr}. \quad (4)$$

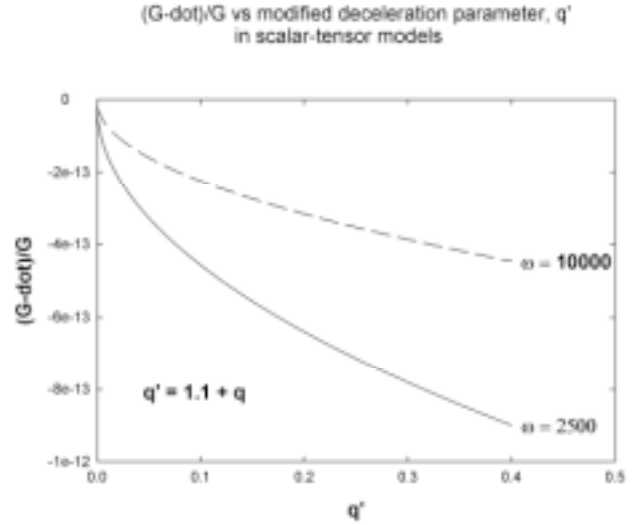


Figure 1. $G\text{-dot}$ depends on the rate of acceleration of the expansion of the Universe in scalar-tensor theories

All of the above $G\text{-dot}$ predictions (Eqs. 1, 3, & 4) assume that the Hubble rate, H , is $H \approx 0.7 \times 10^{-10}/\text{yr}$.

We note that the error bars for a measurement of $(G\text{-dot})/G$ at the level of 10^{-14} would be about 1 mm high on the scale of Figure 1. Thus, it is clear that such accuracy, coupled with likely future improved knowledge of the deceleration parameter, would place extremely severe constraints on \Box .

From the spread among the predictions for $G\text{-dot}$, we see that the value of $G\text{-dot}$ is a very sensitive probe of the type of cosmology and the values of key parameters. It is highly unlikely that, by coincidence, more than one theoretical model will predict any given value of $(G\text{-dot})/G$ to within the accuracy expected from a SEE mission, viz. $\sim 10^{-14}/\text{yr}$. Thus, a measurement of $(G\text{-dot})/G$ at this accuracy will be able to discriminate strongly against all but a handful of specific theoretical models. It will be an effective “theory selector”.

A number of other authors have also investigated the relationship among $G\text{-dot}$ and various parameters of extra-dimension models. Recently Perrotta, Baccigalupi, & Matarrese (1999) explored variants of Brans-Dicke theory which they call “Extended Quintessence.” For illustration they obtained numerical results for two simple forms of the gravitational part of the Lagrangian, namely “Induced Gravity” (IG),

$$F(\Box R) = \Box^2 R, \quad (5)$$

as given in their equation 27, and “Nonminimal Coupling” (NMC),

$$F(\Box R) = (1 + \Box^2) R$$

$$\text{or } (1/(8\Omega G) + \Omega^2)R, \quad (6)$$

as given in their equations 30 and 31. Here R is the Ricci curvature scalar, Ω is the quintessence field, and Ω is a coupling parameter. Note that choosing $\Omega=0$ gives ordinary general relativity. The authors investigate the experimental bounds on Ω and conclude that the tightest bounds come from the present lower bound the Brans-Dicke parameter—which the authors conservatively take as $\Omega \geq 500$ —rather than from the present upper bound on G -dot, viz. $|G\text{-dot}|/G \leq 10^{-11}/\text{yr}$ (Hellings and Damour & Taylor). To wit, they find that the bound on Ω obtained from G -dot is roughly only

$$\Omega \leq 3 \times 10^{-2} \text{ (IG and NMC)} \quad (7)$$

while the bounds obtained from Ω are much tighter, namely roughly

$$\Omega \leq 5 \times 10^{-4} \text{ (IG)} \quad (8)$$

and

$$\Omega \leq 5 \times 10^{-3} \text{ (NMC)}. \quad (9)$$

Perrotta et al. arrived at their conclusions by appealing to a definition of the Planck Mass that sets it equal to $1/G^{1/2}$, which in turn is taken to be the low energy value of the quintessence coupling parameter. By choosing this particular parameterization, they make it possible to interpret predictions of the quintessence field strength in terms of a quantity (M_{pl}) which is well understood in relativistic theories of gravity and cosmology.

A similar approach has been used by Chiba (1999). His choice of the gravitational part of the Lagrangian was essentially the same as for the NMC case of Perrotta et al., viz.

$$R/2 \times [1/(8\Omega G_{\text{bare}}) - \Omega^2] \quad (10)$$

See Chiba's equation 2.1 and the discussion in the immediately following paragraph. Thus, $-\Omega^2$ in Chiba's notation is essentially equivalent to Ω in the notation of Perrotta et al. Chiba uses two different forms of the potential, namely an inverse-power law (his equation 2.6) and an exponential (his page 2, 2nd column, near bottom), following Zlatev et al. and Steinhardt et al. With these choices of potential, Chiba finds that the bound on Ω inferred from the current experimental bound on G -dot is

$$-10^{-2} \leq \Omega \leq 10^{-2} \sim 10^{-1} \quad (11)$$

(Chiba's equation 2.23). This is roughly equivalent to the result obtained by Perrotta et al.

(Eq. 8) when account is taken of the factor of -2 between the meanings of Ω in the two papers.

Earlier investigators have explored the time variation of fundamental constants, but unfortunately most of this work would now require modification in the light of our present knowledge of accelerating Hubble expansion. Among early work with explicit numerical results are those of Wu and colleagues (Wu & Wang, 1986; Wu & Wang, 1987; Chen & Wu, 1989).

5. Implications of a SEE Mission

If SEE is able to achieve the goal of $|(G\text{-dot})/G \sim 10^{-14}$, one result will be a very accurate measurement of Ω from G -dot in the context of the two models of Perrotta et al. The predicted uncertainties should be approximately

$$\Omega \sim 3 \times 10^{-5} \text{ (IG)} \quad (12)$$

$$\Omega \sim 2 \times 10^{-5} \text{ to } 8 \times 10^{-5} \text{ (NMC)} \quad (13)$$

(The latter error varies with Ω and G -dot because of non-linearity.) These anticipated uncertainties are significantly smaller than the upper bounds now available from Ω . The improvement is about 1 order of magnitude over the IG case of Perrotta et al. (Eq. 8) and 2 orders of magnitude over their NMC case (Eq. 9).

A measurement of G -dot can provide an experimental test of the specific theoretical models via the implications for parameter values and whether these are consistent. For example, if the G -dot measured by as SEE mission gives

$$(G\text{-dot})/G = 3 \times 10^{-13}, \quad (14)$$

then the IG model of Perrotta et al. requires the value of Ω to be

$$\Omega \sim 9 \times 10^{-4} \text{ (IG)}. \quad (15)$$

This is moderately inconsistent with the bound from Ω (Eq. 8). Moreover, if the lower bound on Ω is significantly raised, then the inconsistency would become unacceptably large. Thus, this version of IG model would fail the test of experiment.

An alternative test suggested by Perrotta et al. relies on the variation of the Hubble length H^{-1} with the distance parameter z . From their figure 2, one may infer that the Hubble length at $z+1=1000$ is $\sim 26\%$ higher if Ω is zero than if it has the illustrative value 10^{-2} . It follows that, when the state of the art of Hubble measurements is capable of an

error $\sim 1\%$, its variation with z will constitute a measurement of \dot{G} with error $\sim 10^{-3}$. Although this is looser than the present bound of \dot{G} from \dot{H} and the expected error on \dot{G} from G -dot, in the future Hubble measurements could possibly provide the necessary complement to other measurements to carry out a cosmologically-significant test of the IG model or other models.

6. Conclusion

A measurement of G -dot can provide one of the very few ways of using experiment to discriminate among the various multidimensional theories. A SEE mission may hold promise of providing a *controlled* experiment with test masses which have the potential to provide very fine accuracy, thus perhaps making it possible for the first time to discriminate among various possible unified theories. Gravitation is the missing link in efforts to achieve a satisfactory unification theory of physics. The very precise experimental data which would be sought via a SEE mission could thus be key for advancing the prospects of unification theory.

- Because of the significance associated with experimental confirmation of a time-varying G , nothing could do more to invigorate interest in the new theories, most of which do in fact predict time variation of G and other fundamental "constants."
- A finding of non-zero G -dot would of course require extensions of general relativity, since it assumes a constant value of G . More broadly, this would clearly mark the boundaries where general relativity is valid, and specify the onset of new physics.

Acknowledgements

We thank Prof. T. Chiba for helpful suggestions. This work was supported largely by NASA grant NAG 8-1442 in the Fundamental Physics in Microgravity Program. We are also pleased to acknowledge support from a NATO Linkage Grant, an NSF travel grant, and a Scholarly Achievement and Research Incentive Grant from The University of Tennessee.

References

- A.D. ALEXEEV, K.A. BRONNIKOV, N.I. KOLOSNITSIN, M.Yu. KONSTANTINOV, V.N. MELNIKOV, and A.J. SANDERS; "Measurement of the gravitational constant G in space (Project SEE): sensitivity to orbital parameters and space charge effect in space"; *Metrologia* **38** (No. 5), 397-408 (2001).
- A.D. ALEKSEEV, K.A. BRONNIKOV, N.I. KOLOSNITSYN, V.N. MEL'NIKOV, and A.G. RADYNOV; "Error sources in Earth satellite measurements of gravitational interaction parameters"; *Meas. Tech.* **36** (No. 10), 1070-1077 (1993).
- A.D. ALEKSEEV, K.A. BRONNIKOV, N.I. KOLOSNITSYN, V.N. MEL'NIKOV, and A.G. RADYNOV; "Simulation of the procedure for measuring the gravitational constant on a Earth satellite"; *Meas. Tech.* **37** (No. 1), 1-5 (1994).
- K.A. BRONNIKOV, N.I. KOLOSNITSYN, M.Yu. KONSTANTINOV, V.N. MEL'NIKOV, and A.G. RADYNOV; "Measurement of the gravitational interaction. parameters of an Earth-orbiting satellite"; *Meas. Tech.* **36** (No. 8), 845-852 (1993).
- K.A. BRONNIKOV, N.I. KOLOSNITSYN, M.Yu. KONSTANTINOV, V.N. MEL'NIKOV, and A.G. RADYNOV; "Numerical modeling of the trajectories of particles for measuring the gravitational constant on an artificial satellite"; *Meas. Tech.* **36** (No. 9), 951-957 (1993).
- K.A. BRONNIKOV, V.D. IVASHCHUK and V.N. MELNIKOV; "Time variation of gravitational constant in multidimensinoal cosmology"; *Nuovo Cim.* **102 B** (No 2), 209-215 (1988).

- R.R. CALDWELL, R. DAVE, and P.J. STEINHARDT; "Cosmological Imprint of an Energy Component with General Equation of State"; *Phys. Rev. Lett.* **80** (No. 8), 1582–1585 (1998).
- T. CHIBA; "Quintessence, the gravitational constant, and gravity"; *Phys. Rev. D* **60**, 083508, 1-4 (1999).
- W. CHEN and Y-S WU; "Implications of a cosmological constant varying as R^{-2} "; *Phys. Rev. D* **41** (No. 2), 695-698 (1990).
- T. DAMOUR, G.W. GIBBONS, & J.H. TAYLOR; "Limits on the variability of G using binary-pulsar data"; *Phys. Rev. Lett.* **61** (No. 10), 1151-1154 (1988).
- T. DAMOUR & J.H. TAYLOR; "G-dot limit from binary pulsar"; *Astrophys. J.* **366**, 501-511 (1991).
- M. DRINKWATER *et al.* MNRAS, 1999, November 1999, astro-ph/9711290.
- G.T. GILLIES; "The Newtonian gravitational constant: Recent measurements and related studies"; *Reports on Progress in Physics* **60**, 151-225 (1997).
- R.W. HELTINGS, P.J. ADAMS, J.D. ANDERSON, M.S. KEESY, E.L. LAU, E.M. STANDISH, V.M. CANUTO, and I. GOLDMAN; "Experimental test of the variability of G using Viking Lander ranging data"; *Phys. Rev. Lett.* **51** (No. 18), 1609-1612 (1983).
- P.M. GARNAVICH, S. JHA, P. CHALLIS, A. CLOCCHIATTI, A. DIERCKS, A.V. FILIPPENKO, R.L. GILLILAND, C.J. HOGAN, R.P. KIRSHNER, B. LEIBUNDGUT, M.M. PHILLIPS, D. REISS, A.G. RIESS, B.P. SCHMIDT, R.A. SCHOMMER, R.C. SMITH, J. SPYROMILIO, CHRISTOPHER STUBBS, N.B. SUNTZEFF, and J. TONRY; "Supernova limits on the cosmic equation of state"; *Astrophys. J.* **509** (No. 1): 74-79 Part 1 (1998).
- U. ISRAELSSON, M.C. LEE, and A.J. SANDERS; "Roadmap: NASA Plans for Future Gravity Missions"; *Proceedings of the Fourth Alexander Friedmann Seminar, June 18-25, 1998*; St. Petersburg, Russia (1999).
- V.D. IVASHCHUK & V.N. MELNIKOV; "On time variation of gravitational constant in superstring theories"; *Nuovo Cim.* **102 B** (No 2), 131-138 (1988).
- V.D. IVASHCHUK & V.N. MELNIKOV. In: Lecture Notes in Physics, v. 537. *Mathematical and Quantum Aspects of Relativity and Cosmology*. Springer, 2000, p. 214.
- B. LANGE; "The drag-free satellite"; *AIAA J.* **2** (No. 9), 1590-1606 (1964).
- W.J. MARCIANO; "Time variation of the fundamental 'constants' and Kaluza-Klein theories"; *Phys. Rev. Lett.* **52**, 489-491 (1984).
- VN MELNIKOV, KA BRONNIKOV, VD IVASHCHUK, NI KOLOSNITSYN, MYu, KONSTANTINOV; "Time variations of G in different theoretical models and the problem of their measurement"; internal SEE report (February, 2002).
- V.N. MELNIKOV; "Fundamental physical constants and their stability"; *Int. J. Theor. Phys.* **33** (No. 7), 1569-1579 (1994).
- K. NORDTVEDT; "On the geodetic precession of the lunar orbit"; *Class. Quantum Grav.* **13**, 1309-1316 (1996a).
- JM OVERDUIN & PS WESSON; "Kaluza-Klein Gravity"; *Phys. Rep.* **283**, 303-378 (1997).
- S. PERLMUTTER, G. ALDERLING, M. DELLA VALLE, S. DEUSTUA, R.S. ELLIS, S. FABBRO, A. FRUCHTER, G. GOLDBABER, A. GOOBAR, D.E. GROOM, I.M. HOOK, A.G. KIM, M.Y. KIM, R.A. KNOP, C. LIDMAN, R.G. McMAHON, P. NUGENT, R. PAIN, N. PANAGIA, C.R. PENNYMAKER, P. RUIZ-LAPUENTE, B. SCHAEFER, and N. WALTON; "Discovery of a supernova explosion at half the age of the Universe"; *NATURE (London)* **391** (6662): 51-54 (1998).
- F. PERROTTA, C. BACCIGALUPI, and S. MATARRESE; "Extended Quintessence"; *Phys. Rev. D* **61**, 023507, 1-12 (1999).
- R.D. REASENBERG; "The constancy of G and other gravitational experiments"; *Phil Trans. Royal Soc. Lond. A* **310**, 227-238 (1983).

- A.G. RIESS, A.V. FILIPPENKO, P. CHALLIS, A. CLOCCHIATTI, A. DIERCKS, P.M. GARNAVICH, R.L. GILLILAND, C.J. HOGAN, S. JHA, R.P. KIRSHNER, B. LEIBUNDGUT, M.M. PHILLIPS, D. REISS, B.P. SCHMIDT, R.A. SCHOMMER, R.C. SMITH, J. SPYROMILIO, CHRISTOPHER STUBBS, N.B. SUNTZEFF, and J. TONRY; "Observational evidence from supernovae for an accelerating universe and a cosmological constant"; *Astron. J.* **116** 1009-1038 (1998).
- A.J. SANDERS and DEEDS W.E., 1992a. Proposed new determination of the gravitational constant G and tests of Newtonian gravitation. *Phys. Rev. D* **46** (No. 2), 489-504.
- A.J. SANDERS and DEEDS W.E., 1992b. Project SEE: Proposed New Determination of the Gravitational Constant G and Tests of Newtonian Gravitation. *Bull. Am. Phys. Soc.* **37** (No. 7), 1675.
- A.J. SANDERS and DEEDS W.E., 1993. Reply to 'Perturbative Forces in the Proposed Satellite Energy Exchange Experiment'. *Phys. Rev. D.* **47** (No. 8), 3660-3661.
- A.J. SANDERS, DEEDS W.E., and GILLIES G.T., 1993. Proposed new space-based method for more accurate gravitational measurements. In *The Earth and the Universe: Festschrift in honour of Hans-Jürgen Treder*, edited by WILFRIED SCHRÖDER (International Association of Geomagnetism and Aeronomy, Bremen-Rönnebeck, Germany, 1993), pp. 360-365.
- A.J. SANDERS and GILLIES G.T.; "A comparative survey of proposals for space-based determination of the gravitational constant G "; *Rivista Nuovo Cimento* **19** (No. 2), 1-54 (1996).
- A.J. SANDERS and GILLIES GT, 1998. Project SEE (Satellite Energy Exchange): Proposed Space-Based Method for More Accurate Gravitational Measurements. In Bergmann, P. G., de Sabbata, V., Gillies, G. T., and Pronin, P. I., eds., *Spin in Gravity: Is it Possible to Give an Experimental Basis to Torsion?* (International School of Cosmology and Gravitation XVth Course), The Science and Culture Series - Physics, No. 16 (World Scientific, Singapore, 1998), pp. 225-230.
- A.J. SANDERS, A.D. ALEXEEV, S.W. ALLISON, K.A. BRONNIKOV, J.W. CAMPBELL, M.R. CATES, T.A. CORCOVILOS, D.D. EARL, T. GADFORT, G.T. GILLIES, M.J. HARRIS, N.I. KOLOSNITSYN, M.Yu. KONSTANTINOV, V.N. MELNIKOV, R.J. NEWBY, R.G. SCHUNK, and L.L. SMALLEY; "Precision control and measurement issues in the SEE (Satellite Energy Exchange) Satellite"; *Gravitation and Cosmol.* **3**, 287-292 (1997).
- A.J. SANDERS, A.D. ALEXEEV, S.W. ALLISON, K.A. BRONNIKOV, J.W. CAMPBELL, M.R. CATES, T.A. CORCOVILOS, D.D. EARL, T. GADFORT, G.T. GILLIES, M.J. HARRIS, N.I. KOLOSNITSYN, M.Yu. KONSTANTINOV, V.N. MELNIKOV, R.J. NEWBY, R.G. SCHUNK, and L.L. SMALLEY; "Project SEE (Satellite Energy Exchange): An international effort to develop a space-based mission for precise measurements of gravity"; *Class. Quant. Grav.* **17** (no. 12), 2331-2346, 2000.
- A.J. SANDERS, S.W. ALLISON, J.W. CAMPBELL, M.R. CATES, D.D. EARL, G.T. GILLIES, M.J. HARRIS, R.J. NEWBY, & R.G. SCHUNK; "Project SEE (Satellite Energy Exchange): Proposal for Space-based Gravitational Measurements"; *Meas. Sci. Technol.* **10** (No. 6), 514-524 (1999).
- STAFF OF THE SPACE DEPARTMENT, Johns Hopkins Univ., Applied Physics Lab., and STAFF OF THE GUIDANCE AND CONTROL LABORATORY, Stanford Univ.; "A satellite freed of all but gravitational forces: 'TRIAD I'"; *J. Spacecraft and Rockets* **11** (No. 9), 637-644 (1974).
- J.G. WILLIAMS, J.O. DICKEY, and A.X. NEWHALL; "Relativity parameters determined from lunar laser ranging"; *Phys. Rev. D* **53** (No. 12), 6730-6739 (1996).
- Y-S. WU and Z. Wang; "Time variation of Newton's gravitational constant in superstring theories"; *Phys. Rev. Lett.* **57** (No. 16), 1978-1981 (1986).
- Y-S. WU and Z. Wang; "Essay on gravitation: present-time variation of Newton's gravitational constant in superstring theories"; *Gen. Rel. & Grav.* **20** (No. 1), 1-5 (1988).

Tests of CPT and Lorentz Symmetry using Hydrogen and Noble-Gas Masers

Ronald L. Walsworth

*Harvard-Smithsonian Center for Astrophysics
Cambridge, MA 02138, U.S.A.*

We discuss two recent measurements constraining CPT and Lorentz violation using the $^{129}\text{Xe}/^3\text{He}$ Zeeman maser and atomic hydrogen masers. Experimental investigations of CPT and Lorentz symmetry provide important tests of the framework of the standard model of particle physics and theories of gravity. The two-species $^{129}\text{Xe}/^3\text{He}$ Zeeman maser bounds violations of CPT and Lorentz symmetry of the neutron at the 10^{-31} GeV level. Measurements with atomic hydrogen masers provide a clean limit of CPT and Lorentz symmetry violation of the proton at the 10^{-27} GeV level.

Introduction

Lorentz symmetry is a fundamental feature of modern descriptions of nature. Lorentz transformations include both spatial rotations and boosts. Therefore, experimental investigations of rotation symmetry provide important tests of the framework of the standard model of particle physics and single-metric theories of gravity¹.

In particular, the minimal $\text{SU}(3)\times\text{SU}(2)\times\text{U}(1)$ standard model successfully describes particle phenomenology, but is believed to be the low energy limit of a more fundamental theory that incorporates gravity. While the fundamental theory should remain invariant under Lorentz transformations, spontaneous symmetry-breaking could result at the level of the standard model in small violations of Lorentz invariance and CPT (symmetry under simultaneous application of Charge conjugation, Parity inversion, and Time reversal)².

Clock comparisons provide sensitive tests of rotation invariance and hence Lorentz symmetry by bounding the frequency variation of a given clock as its orientation changes, e.g., with respect to the distant stars³. In practice, the most precise limits are obtained by comparing the frequencies of two co-located clocks as they rotate with the Earth. Atomic clocks are typically used, involving the electromagnetic signals emitted or absorbed on hyperfine or Zeeman transitions.

Here we discuss results from two recent atomic clock tests of CPT and Lorentz symmetry:

- (1) Using a two-species $^{129}\text{Xe}/^3\text{He}$ Zeeman maser^{4,5,6} we placed a limit on CPT and Lorentz violation of the neutron of approximately 10^{-31} GeV⁷,

improving by more than a factor of six on the best previous measurement^{8,9}.

- (2) We employed atomic hydrogen masers to set an improved clean limit on CPT and Lorentz violation of the proton, at the level of nearly 10^{-27} GeV¹⁰.

Motivation

Our atomic clock comparisons are motivated by a standard model extension developed by Kostelecký and others^{3,11,12,13,14,15,16,17,18,19}. This theoretical framework accommodates possible spontaneous violation of CPT and Lorentz symmetry, which may occur in a fundamental theory combining the standard model with gravity. For example, this might occur in string theory²⁰. The standard model extension is quite general: it emerges as the low-energy limit of any underlying theory that generates the standard model and contains spontaneous Lorentz symmetry violation²¹. The extension retains the usual gauge structure and power-counting renormalizability of the standard model. It also has many other desirable properties, including energy-momentum conservation, observer Lorentz covariance, conventional quantization, and hermiticity. Microcausality and energy positivity are expected.

This well-motivated theoretical framework suggests that small, low-energy signals of CPT and Lorentz violation may be detectable in high-precision experiments. The dimensionless suppression factor for such effects would likely be the ratio of the low-energy scale to the Planck scale, perhaps combined with dimensionless coupling constants^{3,11,12,13,14,15,16,17,18,19,20,21}. A key feature of the standard model extension of Kostelecký *et al.* is that it is at the level of the known elementary particles, and thus enables quantitative comparison of a wide array of tests of Lorentz symmetry. In recent work the standard model extension has been used to quantify bounds on CPT and Lorentz violation from measurements of neutral meson oscillations¹¹; tests of QED in Penning traps¹²; photon birefringence in the vacuum^{13,14}; baryogenesis¹⁵; hydrogen and antihydrogen spectroscopy¹⁶; experiments with muons¹⁷; a spin-polarized torsion pendulum¹⁸; observations with cosmic rays¹⁹; and atomic clock comparisons³. Recent experimental work motivated by this standard model extension includes Penning trap tests by Gabrielse *et al.* on the antiproton and H^- ²², and by Dehmelt *et al.* on the electron and positron^{23,24}, which place improved limits on CPT and Lorentz violation in these systems. Also, a re-analysis by Adelberger, Gundlach, Heckel, and co-workers of existing data from the “Eöt-Wash II” spin-polarized torsion pendulum^{25,26} sets the most stringent bound

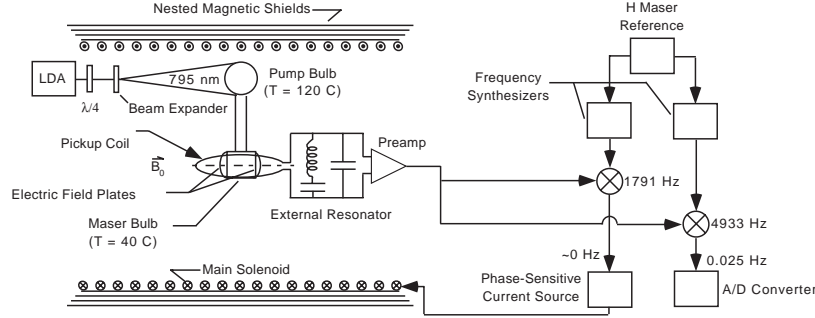


Figure 1: Schematic of the $^{129}\text{Xe}/^3\text{He}$ Zeeman maser

to date on CPT and Lorentz violation of the electron: approximately 10^{-29} GeV²⁷.

In particular, the standard model extension admits Lorentz-violating couplings of noble gas nuclei and hydrogen atoms to expectation values of tensor fields. (Some of these couplings also violate CPT.) Each of the tensor fields may have an unknown magnitude and orientation in space, to be limited by experiment.

$^{129}\text{Xe}/^3\text{He}$ maser test of CPT and Lorentz symmetry

The design and operation of the two-species $^{129}\text{Xe}/^3\text{He}$ maser has been discussed in recent publications^{4,5,6}. (See the schematic in Fig. 1.) Two dense, co-located ensembles of ^3He and ^{129}Xe atoms perform continuous and simultaneous maser oscillations on their respective nuclear spin 1/2 Zeeman transitions at approximately 4.9 kHz for ^3He and 1.7 kHz for ^{129}Xe in a static magnetic field of 1.5 gauss. This two-species maser operation can be maintained indefinitely. The population inversion for both maser ensembles is created by spin exchange collisions between the noble gas atoms and optically-pumped Rb vapor²⁸. The $^{129}\text{Xe}/^3\text{He}$ maser has two chambers, one acting as the spin exchange “pump bulb” and the other serving as the “maser bulb”. This two chamber configuration permits the combination of physical conditions necessary for a high flux of spin-polarized noble gas atoms into the maser bulb, while also maintaining ^3He and ^{129}Xe maser oscillations with good frequency stability: ~ 100 nHz stability is typical for measurement intervals of ~ 1 hour⁶. (A single-bulb $^{129}\text{Xe}/^3\text{He}$ maser does not provide good frequency stability because of the large Fermi contact shift of the ^{129}Xe Zeeman frequency caused

by ^{129}Xe -Rb collisions²⁹.) Either of the noble gas species can serve as a precision magnetometer to stabilize the system's static magnetic field, while the other species is employed as a sensitive probe for CPT and Lorentz-violating interactions or other subtle physical influences. (For example, we are also using the $^{129}\text{Xe}/^3\text{He}$ maser to search for a permanent electric dipole moment of ^{129}Xe as a test of time reversal symmetry; hence the electric field plates in Fig. 1.)

We search for a signature of Lorentz violation by monitoring the relative phases and Zeeman frequencies of the co-located ^3He and ^{129}Xe masers as the laboratory reference frame rotates with respect to the distant stars. We operate the system with the quantization axis directed east-west on the Earth, the ^3He maser free-running, and the ^{129}Xe maser phase-locked to a signal derived from a hydrogen maser in order to stabilize the magnetic field. To leading order, the standard model extension of Kostelecký *et al.* predicts that the Lorentz-violating frequency shifts for the ^3He and ^{129}Xe maser are the same size and sign³. Hence the possible Lorentz-violating frequency shift in the free-running ^3He maser ($\delta\nu_{He}$) is given by:

$$\delta\nu_{He} = \delta\nu_{Lorentz} [\gamma_{He}/\gamma_{Xe} - 1], \quad (1)$$

where $\delta\nu_{Lorentz}$ is the sidereal-day-period modulation induced in both noble gas Zeeman frequencies by the Lorentz-violating interaction, and $\gamma_{He}/\gamma_{Xe} \approx 2.75$ is the ratio of gyromagnetic ratios for ^3He and ^{129}Xe .

We acquired 90 days of data for this experiment over the period April, 1999 to May, 2000. We reversed the main magnetic field of the apparatus every ~ 4 days to help distinguish possible Lorentz-violating effects from diurnal systematic variations. In addition, we carefully assessed the effectiveness of the ^{129}Xe co-magnetometer, and found that it provides excellent isolation from possible diurnally-varying ambient magnetic fields, which would not average away with field reversals. Furthermore, the relative phase between the solar and sidereal day evolved about 2π radians over the course of the experiment; hence diurnal systematic effects from any source would be reduced by averaging the results from the measurement sets.

We analyzed each day's data and determined the amplitude and phase of a possible sidereal-day-period variation in the free-running ^3He maser frequency. (See Fig. 2 for an example of one day's data.) We employed a linear least squares method to fit the free-running maser phase vs. time using a minimal model including: a constant (phase offset); a linear term (Larmor precession); and cosine and sine terms with sidereal day period. For each day's data, we included terms corresponding to quadratic and maser amplitude-induced phase drift if they significantly improved the reduced chi-squared³⁰. As a final

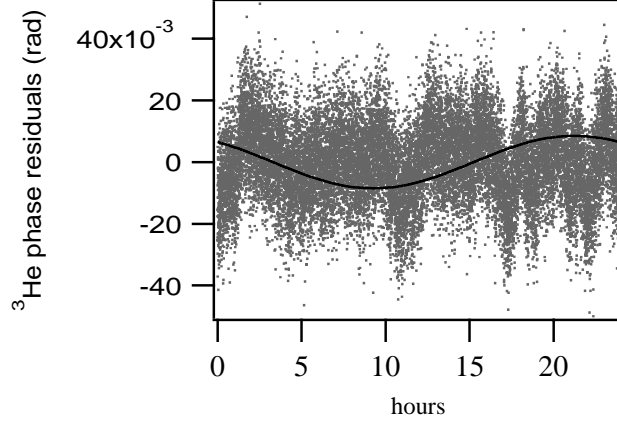


Figure 2: Typical data from the Lorentz/CPT test using the $^{129}\text{Xe}/^3\text{He}$ maser. ^3He maser phase data residuals are shown for one sidereal day. Larmor precession and drift terms have been removed, and the best-fit sinusoid curve (with sidereal-day-period) is displayed

check, we added a *faux* Lorentz-violating effect of known phase and amplitude to the raw data and performed the analysis as before. We considered our data reduction for a given sidereal day to be successful if the synthetic physics was recovered and there was no significant change in the covariance matrix generated by the fitting routine.

Using the 90 days of data, we found no statistically significant sidereal variation of the free-running ^3He maser frequency at the level of 45 nHz (one-sigma confidence). Kostelecký and Lane report that the nuclear Zeeman transitions of ^{129}Xe and ^3He are primarily sensitive to Lorentz-violating couplings of the neutron, assuming the correctness of the Schmidt model of the nuclei³. Thus our search for a sidereal-period frequency shift of the free-running ^3He maser ($\delta\nu_{He}$) provides a bound to the following parameters characterizing the magnitude of Lorentz/CPT violations in the standard model extension:

$$\left| -3.5\tilde{b}_J^n + 0.012\tilde{d}_J^n + 0.012\tilde{g}_{D,J}^n \right| \leq 2\pi\delta\nu_{He,J} \quad (^{129}\text{Xe}/^3\text{He} \text{ maser}) \quad (2)$$

Here $J = X, Y$ denotes spatial indices in a non-rotating frame, with X and Y oriented in a plane perpendicular to the Earth's rotation axis and we have taken $\hbar = c = 1$. The parameters \tilde{b}_J^n , \tilde{d}_J^n , and $\tilde{g}_{D,J}^n$ describe the strength of Lorentz-violating couplings of the neutron to possible background tensor

fields. \tilde{b}_J^n and $\tilde{g}_{D,J}^n$ correspond to couplings that violate both CPT and Lorentz symmetry, while \tilde{d}_J^n corresponds to a coupling that violates Lorentz symmetry but not CPT. All three of these parameters are different linear combinations of fundamental parameters in the underlying relativistic Lagrangian of the standard model extension^{3,11,12,13,14,15,16,17,18}.

It is clear from Eqn. (2) that the $^{129}\text{Xe}/^3\text{He}$ clock comparison is primarily sensitive to Lorentz/CPT violations associated with the neutron parameter \tilde{b}_J^n . Similarly, the most precise previous search for Lorentz/CPT violations of the neutron, the $^{199}\text{Hg}/^{133}\text{Cs}$ experiment of Lamoreaux, Hunter *et al.*^{8,9}, also had principal sensitivity to \tilde{b}_J^n at the following level³:

$$\left| \frac{2}{3} \tilde{b}_J^n + \{\text{small terms}\} \right| \leq 2\pi\delta\nu_{Hg,J} \quad (^{199}\text{Hg}/^{133}\text{Cs}). \quad (3)$$

In this case, the experimental limit, $\delta\nu_{Hg,J}$, was a bound of 55 nHz (one-sigma confidence) on a sidereal-period variation of the ^{199}Hg nuclear Zeeman frequency, with the ^{133}Cs electronic Zeeman frequency serving as a co-magnetometer.

Therefore, in the context of the standard model extension of Kostelecký and co-workers³, our $^{129}\text{Xe}/^3\text{He}$ maser measurement improves the constraint on \tilde{b}_J^n to approximately 10^{-31} GeV, or more than six times better than the $^{199}\text{Hg}/^{133}\text{Cs}$ clock comparison^{8,9}. Note that the ratio of this limit to the neutron mass ($10^{-31}\text{GeV}/m_n \sim 10^{-31}$) compares favorably to the dimensionless suppression factor $m_n/M_{\text{Planck}} \sim 10^{-19}$ that might be expected to govern spontaneous CPT and Lorentz symmetry breaking originating at the Planck scale.

We expect more than an order of magnitude improvement in sensitivity to Lorentz/CPT violation of the neutron using a new device recently demonstrated in our laboratory: the $^{21}\text{Ne}/^3\text{He}$ Zeeman maser. The expected exceptional performance of the $^{21}\text{Ne}/^3\text{He}$ maser is largely due to two factors: (i) the greater theoretical sensitivity of the $^{21}\text{Ne}/^3\text{He}$ system to CPT and Lorentz violation because of a larger ratio of nuclear magnetic moments; and (ii) the more similar physical and chemical properties of ^{21}Ne and ^3He , compared to ^{129}Xe and ^3He , with resultant practical advantages for the $^{21}\text{Ne}/^3\text{He}$ maser as a differential atomic clock.

Hydrogen maser test of CPT and Lorentz symmetry

The hydrogen maser is an established tool in precision tests of fundamental physics³¹. Hydrogen masers operate on the $\Delta F = 1$, $\Delta m_F = 0$ hyperfine transition in the ground state of atomic hydrogen³². Hydrogen molecules are

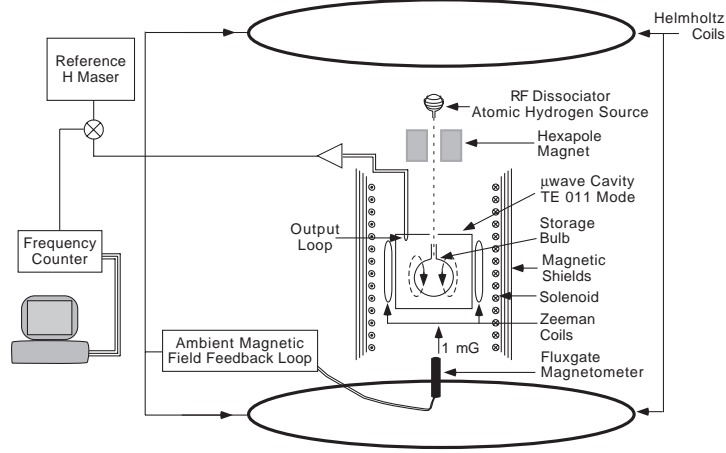


Figure 3: Schematic of the H maser in its ambient field stabilization loop.

dissociated into atoms in an RF discharge, and the atoms are state selected via a hexapole magnet (Fig. 3). The high field seeking states, ($F = 1$, $m_F = +1, 0$) are focused into a Teflon coated cell which resides in a microwave cavity resonant with the $\Delta F = 1$ transition at 1420 MHz. The $F = 1$, $m_F = 0$ atoms are stimulated to make a transition to the $F = 0$ state by the field of the cavity. A static magnetic field of ~ 1 milligauss is applied to maintain the quantization axis of the H atoms.

The hydrogen transitions most sensitive to potential CPT and Lorentz violations are the $F = 1$, $\Delta m_F = \pm 1$ Zeeman transitions. In the 0.6 mG static field applied for these measurements, the Zeeman frequency is $\nu_Z \approx 850$ Hz. We utilize a double resonance technique to measure this frequency with a precision of ~ 1 mHz^{33,34}. We apply a weak magnetic field perpendicular to the static field and oscillating at a frequency close to the Zeeman transition. This audio-frequency driving field couples the three sublevels of the $F = 1$ manifold of the H atoms. Provided a population difference exists between the $m_F = \pm 1$ states, the energy of the $m_F = 0$ state is altered by this coupling, thus shifting the measured maser frequency in a carefully analyzed manner^{33,34} described by a dispersive shape (Fig. 4(a)). Importantly, the maser frequency is unchanged when the driving field is exactly equal to the Zeeman frequency. Therefore, we determine the Zeeman frequency by measuring the driving field frequency at which the maser frequency in the presence of the driving field is equal to the unperturbed maser frequency.

The $F = 1$, $\Delta m_F = \pm 1$ Zeeman frequency is directly proportional to the static magnetic field, in the small-field limit. Four layers of high permeability (μ -metal) magnetic shields surround the maser (Fig. 3), screening external field fluctuations by a factor of 32 000. Nevertheless, external magnetic field fluctuations cause remnant variations in the observed Zeeman frequency. As low frequency magnetic noise in the neighborhood of this experiment is much larger during the day than late at night, the measured Zeeman frequency could be preferentially shifted by this noise (at levels up to ~ 0.5 Hz) with a 24 hour periodicity which is difficult to distinguish from a true sidereal signal in our relatively short data sample. Therefore, we employ an active stabilization system to cancel such magnetic field fluctuations (Fig. 3). A fluxgate magnetometer placed within the maser's outer magnetic shield controls large (2.4 m dia.) Helmholtz coils surrounding the maser via a feedback loop to maintain a constant ambient field. This feedback loop reduces the fluctuations at the sidereal frequency to below the equivalent of $1 \mu\text{Hz}$ on the Zeeman frequency at the location of the magnetometer.

The Zeeman frequency of a hydrogen maser was measured for 32 days over the period Nov., 1999 to March, 2000. During data taking, the maser remained in a closed, temperature controlled room to reduce potential systematics from thermal drifts which might be expected to have 24 hour periodicities. The feedback system also maintained a constant ambient magnetic field. Each Zeeman measurement took approximately 20 minutes to acquire and was subsequently fit to extract a Zeeman frequency (Fig. 4(a)). Also monitored were maser amplitude, residual magnetic field fluctuation, ambient temperature, and current through the solenoidal coil which determines the Zeeman frequency (Fig. 3).

The data were then fit to extract the sidereal-period sinusoidal variation of the Zeeman frequency. (See Fig. 4(b) for an example of 11 days of data.) In addition to the sinusoid, piecewise linear terms (whose slopes were allowed to vary independently for each day) were used to model the slow remnant drift of the Zeeman frequency. No significant sidereal-day-period variation of the hydrogen $F = 1$, $\Delta m_F = \pm 1$ Zeeman frequency was observed. Our measurements set a bound on the magnitude of such a variation of $\delta\nu_Z^H \leq 0.37$ mHz (one-sigma level). Expressed in terms of energy, this is a shift in the Zeeman splitting of about $1 \cdot 10^{-27}$ GeV.

The hydrogen atom is directly sensitive to CPT and Lorentz violations of the proton and the electron. Following the notation of reference¹⁶, one finds that a limit on a sidereal-day-period modulation of the Zeeman frequency ($\delta\nu_Z^H$) provides a bound to the following parameters characterizing the magnitude of Lorentz/CPT violations in the standard model extension of Kostelecký

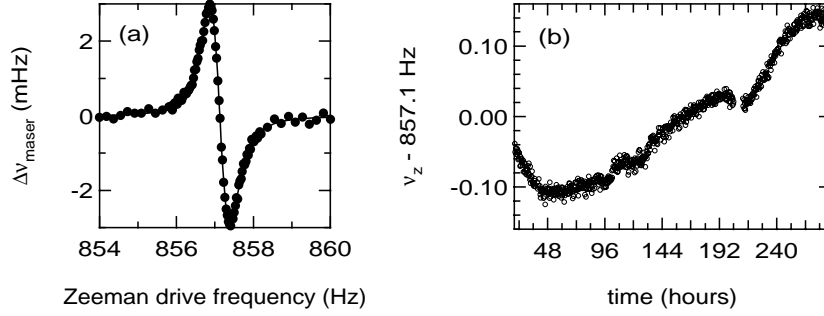


Figure 4: (a) An example of a double resonance measurement of the $F = 1$, $\Delta m_F = \pm 1$ Zeeman frequency in the hydrogen maser. The change from the unperturbed maser frequency is plotted versus the driving field frequency. (b) Zeeman frequency data from 11 days of the Lorentz/CPT test using the H maser.

and co-workers:

$$|b_3^e + b_3^p - d_{30}^e m_e - d_{30}^p m_p - H_{12}^e - H_{12}^p| \leq 2\pi\delta\nu_Z^H \quad (4)$$

for the low static magnetic fields at which we operate. (Again, we have taken $\hbar = c = 1$.) The terms b^e and b^p describe the strength of background tensor field couplings that violate CPT and Lorentz symmetry while the H and d terms describe couplings that violate Lorentz symmetry but not CPT¹⁶. The subscript 3 in Eqn. (4) indicates the direction along the quantization axis of the apparatus, which is vertical in the lab frame but rotates with respect to the fixed stars with the period of the sidereal day.

As in refs.^{3,23}, we can re-express the time varying change in the hydrogen Zeeman frequency in terms of parameters expressed in a non-rotating frame as

$$2\pi\delta\nu_{Z,J}^H = \left(\tilde{b}_J^p + \tilde{b}_J^e\right) \sin \chi. \quad (5)$$

where $\tilde{b}_J^w = b_J^w - d_{j0}^w m_w - \frac{1}{2}\epsilon_{JKL}H_{KL}^w$, $J = X, Y$ refers to non-rotating spatial indices in the plane perpendicular to the rotation vector of the earth, w refers to either the proton or electron parameters, and $\chi = 48^\circ$ is the co-latitude of the experiment.

As noted above, a re-analysis by Adelberger, Gundlach, Heckel, and co-workers of existing data from the “Eöt-Wash II” spin-polarized torsion pendulum^{25,26} sets the most stringent bound to date on CPT and Lorentz violation

of the electron: $\tilde{b}_J^e \leq 10^{-29}$ GeV²⁷. Therefore, in the context of the standard model extension of Kostelecký and co-workers^{16,3} the H maser measurement to date constrains CPT and Lorentz violations of the proton parameter $\tilde{b}_J^p \leq 2 \cdot 10^{-27}$ GeV at the one sigma level. This limit is comparable to that derived from the ¹⁹⁹Hg/¹³³Cs experiment of Lamoreaux, Hunter *et al.*^{8,9} but in a much cleaner system (the hydrogen atom nucleus is a proton, compared to the complicated nuclei of ¹⁹⁹Hg and ¹³³Cs).

We expect that the sensitivity of the H maser Lorentz/CPT test can be improved by more than an order of magnitude through technical upgrades to the maser's thermal and magnetic field systems; better environmental control of the room housing the maser; and a longer period of data acquisition.

Conclusions

Precision comparisons of atomic clocks provide sensitive tests of CPT and Lorentz symmetry, thereby probing extensions to the standard model in which these symmetries can be spontaneously broken. Measurements using the two-species ¹²⁹Xe/³He Zeeman maser constrain violations of CPT and Lorentz symmetry of the neutron at the 10⁻³¹ GeV level. Measurements with atomic hydrogen masers provide clean tests of CPT and Lorentz symmetry violation of the proton at the 10⁻²⁷ GeV level. Improvements in both experiments are being pursued.

Acknowledgments

I gratefully acknowledge my collaborators on the work described above: David Bear, Federico Cane, Marc Humphrey, Alan Kostelecky, Charles Lane, Edward Mattison, David Phillips, Richard Stoner, and Robert Vessot. Support for the Lorentz/CPT violation tests was provided by NASA and the Smithsonian Institution.

References

1. C. M. Will, *Theory and Experiment in Gravitational Physics*, Cambridge University Press, New York, 1981.
2. The discrete symmetries C, P, and T are discussed, for example, in R. G. Sachs, *The Physics of Time Reversal*, University of Chicago, Chicago, 1987.
3. V. A. Kostelecký and C. D. Lane, *Phys. Rev. D* **60**, 116010/1-17 (1999).
4. T. E. Chupp, R. J. Hoare, R. L. Walsworth, and B. Wu, *Phys. Rev. Lett.* **72**, 2363-2366 (1994).

5. R. E. Stoner, M. A. Rosenberry, J. T. Wright, T. E. Chupp, E. R. Oteiza, and R. L. Walsworth, *Phys. Rev. Lett.* **77**, 3971-3974 (1996).
6. D. Bear, T. E. Chupp, K. Cooper, S. DeDeo, M. A. Rosenberry, R. E. Stoner, and R. L. Walsworth, *Phys. Rev. A* **57**, 5006-5008 (1998).
7. D. Bear, R. E. Stoner, R. L. Walsworth, V. A. Kostelecký, and C. D. Lane, *Phys. Rev. Lett.* **85**, 5038-5041 (2000).
8. C. J. Berglund, L. R. Hunter, D. Krause, Jr., E. O. Prigge, M. S. Ronfeldt, and S. K. Lamoreaux, *Phys. Rev. Lett.* **75**, 1879-1882 (1995).
9. L. R. Hunter, C. J. Berglund, M. S. Ronfeldt, E. O. Prigge, D. Krause, Jr., and S. K. Lamoreaux, "A Test of Local Lorentz Invariance Using Hg and Cs Magnetometers," in *CPT and Lorentz Symmetry*, edited by V. A. Kostelecký, World Scientific, Singapore, 1999, pp. 180-186.
10. D. F. Phillips, M. A. Humphrey, E. M. Mattison, R. E. Stoner, R. F. C. Vessot, and R. L. Walsworth, *Phys. Rev. D* **63**, 111101-111104 (2001).
11. V. A. Kostelecký and R. Potting, "CPT, Strings, and the $K - \bar{K}$ System," in *Gamma Ray-Neutrino Cosmology and Planck Scale Physics*, edited by D. B. Cline, World Scientific, Singapore, 1993, hep-th/9211116; *Phys. Rev. D* **51**, 3923-3935 (1995); D. Colladay and V. A. Kostelecký, *Phys. Lett. B* **344**, 259-265 (1995); *Phys. Rev. D* **52**, 6224-6230 (1995); V. A. Kostelecký and R. Van Kooten, *Phys. Rev. D* **54**, 5585 (1996); V. A. Kostelecký, *Phys. Rev. Lett.* **80**, 1818-1821 (1998); *Phys. Rev. D* **61**, 16002/1-9 (2000).
12. R. Bluhm, V. A. Kostelecký, and N. Russell, *Phys. Rev. Lett.* **79**, 1432-1435 (1997); *Phys. Rev. D* **57**, 3932-3943 (1998).
13. S. M. Carroll, G. B. Field, and R. Jackiw, *Phys. Rev. D* **41**, 1231-1240 (1990).
14. D. Colladay and V. A. Kostelecký, *Phys. Rev. D* **55**, 6760-6774 (1997); *ibid.* **58**, 116002/1-23 (1998); R. Jackiw and V. A. Kostelecký, *Phys. Rev. Lett.* **82**, 3572-3575 (1999);
15. O. Bertolami, D. Colladay, V. A. Kostelecký, and R. Potting, *Phys. Lett. B* **395**, 178-183 (1997).
16. R. Bluhm, V. A. Kostelecký, and N. Russell, *Phys. Rev. Lett.* **82**, 2254-2257 (1999).
17. R. Bluhm, V. A. Kostelecký, and C. D. Lane, *Phys. Rev. Lett.* **84**, 1098-1101 (2000).
18. R. Bluhm and V. A. Kostelecký, *Phys. Rev. Lett.* **84**, 1381-1384 (2000).
19. S. Coleman and S. L. Glashow, *Phys. Rev. D* **56**, 116008/1-14 (1999).
20. V. A. Kostelecký and S. Samuel, *Phys. Rev. D* **39**, 683-685 (1989); *ibid.* **40**, 1886-1903 (1989); V. A. Kostelecký and R. Potting, *Nucl. Phys. B* **359**, 545-570 (1991); *Phys. Lett. B* **381**, 89-96 (1996).

21. V. A. Kostelecký and S. Samuel, *Phys. Rev. Lett.* **63**, 224-227 (1989); *ibid.* **66**, 1811-1814 (1991).
22. G. Gabrielse, A. Khabbaz, D. S. Hall, C. Heimenn, H. Kalinowski, and W. Jhe, *Phys. Rev. Lett.* **82**, 3198-3201 (1999).
23. R. K. Mittleman, I. I. Ioannou, H. G. Dehmelt, and N. Russell, *Phys. Rev. Lett.* **83**, 2116-2119 (1999).
24. H. Dehmelt, R. Mittleman, R. S. Van Dyck, Jr., and P. Schwinberg, *Phys. Rev. Lett.* **83**, 4694-4696 (1999).
25. E. G. Adelberger, *et al.*, in *Physics Beyond the Standard Model*, edited by P. Herczeg *et al.*, World Scientific, Singapore, 1999, p. 717.
26. M. G. Harris, Ph.D. thesis, Univ. of Washington, 1998.
27. B. Heckel, presented at International Conference on Orbis Scientiae 1999: Quantum Gravity, Generalized Theory of Gravitation and Superstring Theory Based Unification (28th Conference on High Energy Physics and Cosmology Since 1964), Fort Lauderdale, Florida, 16-19 Dec., 1999.
28. T. G. Walker and W. Happer, *Rev. Mod. Phys.* **69**, 629-642 (1997).
29. M. V. Romalis and G. D. Cates, *Phys. Rev. A* **58**, 3004-3011 (1998); N. R. Newbury, A. S. Barton, P. Bogorad, G. D. Cates, H. Mabuchi, and B. Saam, *Phys. Rev. A* **48**, 558-568 (1993); S. R. Schafer, G. D. Cates, T. R. Chien, D. Gonatas, W. Happer, and T. G. Walker, *Phys. Rev. A* **39**, 5613-5623 (1989).
30. We employed the F-test at the 99% confidence level to decide whether the addition of a new term to the fit model was justified. See Philip R. Bevington, *Data Reduction and Error Analysis for the Physical Sciences, Second Ed.*, McGraw-Hill, Boston, 1992, ch. 11.
31. R. F. C. Vessot, *et al.*, *Phys. Rev. Lett.* **45**, 2081-2084 (1980); R. J. P. Turneaure, C. M. Will, B. F. Farrell, E. M. Mattison, and R. F. C. Vessot, *Phys. Rev. D* **27**, 1705-1714 (1983); R. L. Walsworth, I. F. Silvera, E. M. Mattison, and R. F. C. Vessot, *Phys. Rev. Lett.* **64**, 2599-2602 (1990).
32. D. Kleppner, H. M. Goldenberg, and N. F. Ramsey, *Phys. Rev.* **126**, 603-615 (1962); D. Kleppner, H. C. Berg, S. B. Crampton, N. F. Ramsey, R. F. C. Vessot, H. E. Peters, and J. Vanier, *Phys. Rev.* **138**, A972-983 (1965).
33. H. G. Andresen, *Z. Physik*, **210**, 113-141 (1968).
34. M. A. Humphrey, D. F. Phillips, and R. L. Walsworth, *Phys. Rev. A* **62**, 063405-063405 (2000).

Optical Atomic Clocks for Space

Leo Hollberg, Jim Bergquist, and Chris Oates

*Time and Frequency Division
National Institute of Standards and Technology, Boulder, CO*

At NIST, in Boulder, we have started a project to develop and evaluate advanced optical frequency standards for applications in space. Optical standards promise many advantages over traditional microwave standards primarily because they operate at 100,000 times higher frequency (see Slide 1). Thus, stable laser oscillators, referenced to narrow resonances in laser-cooled atoms will be the time and frequency standards of the future. Projected fractional frequency uncertainties for optical standards are at the 10^{-18} level. Our research effort focuses on eliminating or reducing the most serious impediments to the performance of the optical frequency standards, and in particular studying what might be possible by taking advantage of a micro-g environment.

We are presently evaluating the performance of two independent optical frequency standards, one based on 5 million laser-cooled calcium atoms (at 456 THz or 657 nm) (see Slides 2-4), and the other on a single trapped Hg^+ ion (at 1064 THz or 282 nm) (Slides 5-7)). We have developed a mode-locked fs-laser system that can generate an octave-spanning frequency comb (Slides 8-10), which allows us to compare the performance of these two standards with each other and with H masers that are calibrated by the NIST Cs fountain. A first comparison of the short-term fractional instability between the two optical standards achieved a level of 7×10^{-15} @ 1 s (Slide 12), more than an order of magnitude better than state-of-the-art microwave standards. Recent absolute frequency measurements of the optical standards relative to Cs had uncertainties of 1×10^{-14} for the Hg^+ system (Slide 13) and 7×10^{-14} for the Ca system (Slide 14). Repeated frequency measurements have put constraints on the drifts of the transition frequencies relative to Cs at $< 10^{-13} \text{ yr}^{-1}$ level; these measurements could have serious implications concerning possible drifts in the fundamental constants, a topic currently of great interest.

In order to bring these optical standards to their fundamental limits, we are presently investigating several critical issues, two of which could directly benefit from a micro-g environment. The first concerns the laser local oscillators for these systems, which need to have to exceptional spectral purity (instability less than 10^{-16}) on short time scales (< 10 s) for the optical standards to reach their predicted performance levels. Most often this is achieved by locking the frequency of the laser to a high-finesse, environmentally-isolated optical cavity. Frequency fluctuations of the optical oscillator are then dominantly caused by seismic perturbations that are coupled through the suspension system that must support the cavity against the pull of gravity. Since the frequency of the fundamental resonance of the isolation support system is proportional to $g^{1/2}$, seismic isolation could be more than three orders of magnitude better in a micro-g environment. Secondly, for the neutral atom systems, the pull of gravity limits the attainable laser-atom interaction time to a fraction of a second, which in turn limits the achievable line Q for the reference transition. With suitably cold atoms, interaction times of 10 or more seconds would be possible in micro-g, thus improving the performance of the neutral optical standards by more than an order of magnitude. We recently demonstrated a second-stage cooling scheme for Ca that reduces the atomic temperature 200-fold (Slide 15), moving it into the velocity regime where the acceleration due to gravity becomes problematic.

Introduction to optical atomic clocks

1. High line Q and good signal-to-noise ratio (stable)

$$\text{Fractional frequency instability} \propto \frac{\Delta \omega}{\omega_0 \cdot S / N} \propto \frac{1}{Q \cdot S / N}$$

$$\frac{\Delta \omega_{\text{optical}}}{\Delta \omega_{\text{microwave}}} \propto \frac{10^{15}}{10^{10}} \propto 10^5$$

$$\frac{1}{Q \cdot N_{\text{atoms}}} \propto 10^{-16} @ 1\text{s}$$

2. Insensitive to external perturbations (accurate)

Single trapped ions vs. trapped neutrals ($> 10^6$)

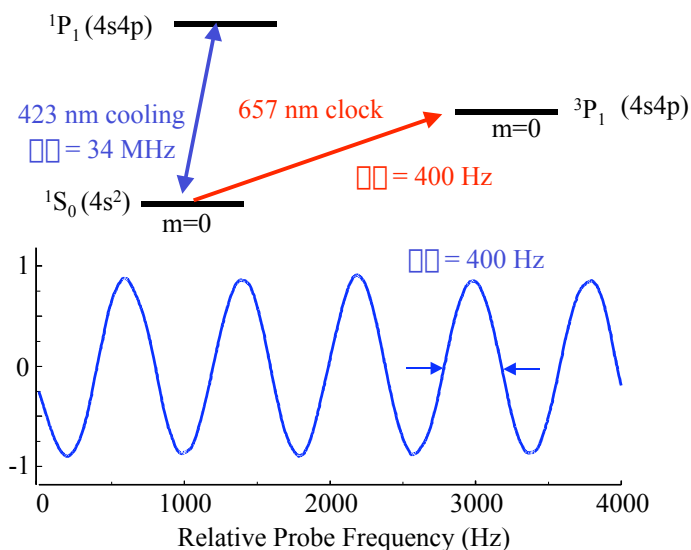
$\text{Hg}^+, \text{Yb}^+, \text{In}^+$ vs. $\text{Ca}, \text{Sr}, \text{Mg}, \text{H}$

$\propto 10^{-18}$

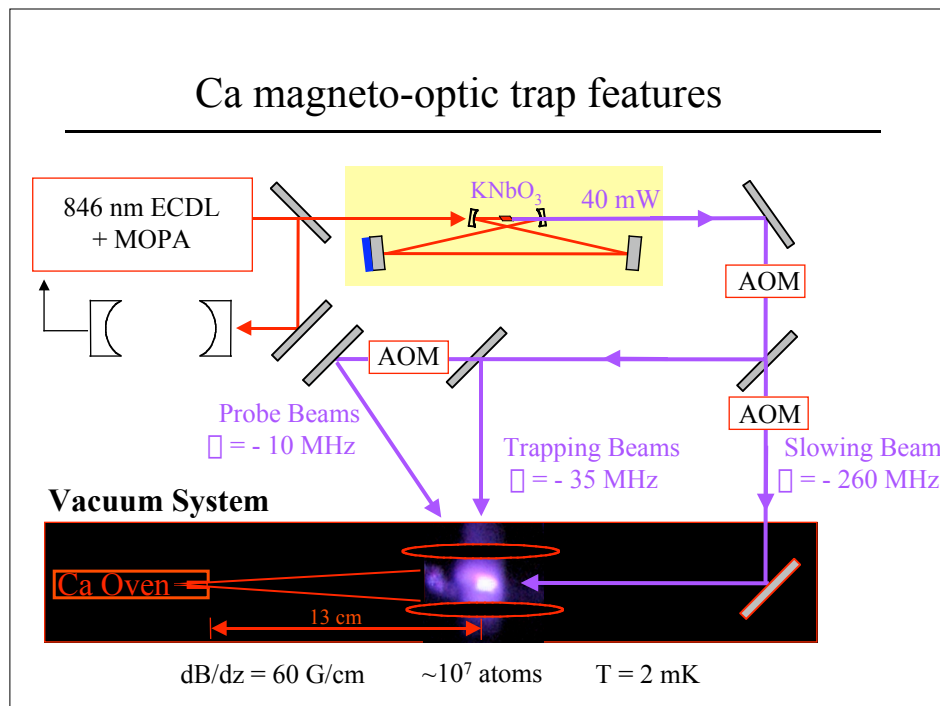
Systems under development at NIST

Slide 1 Introduction to optical atomic clocks, highlighting their advantages over their microwave counterparts.

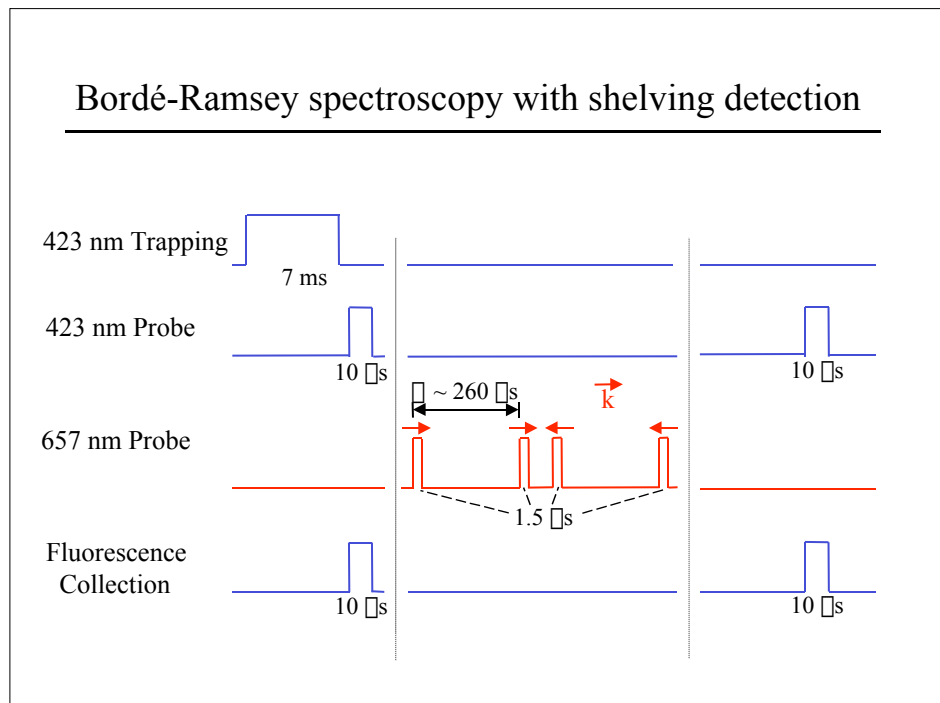
Spectroscopy of the Ca clock transition



Slide 2 High resolution Bordé-Ramsey spectroscopy of the Ca clock transition using 5×10^6 cold atoms. Data shown required 60 s of averaging time.

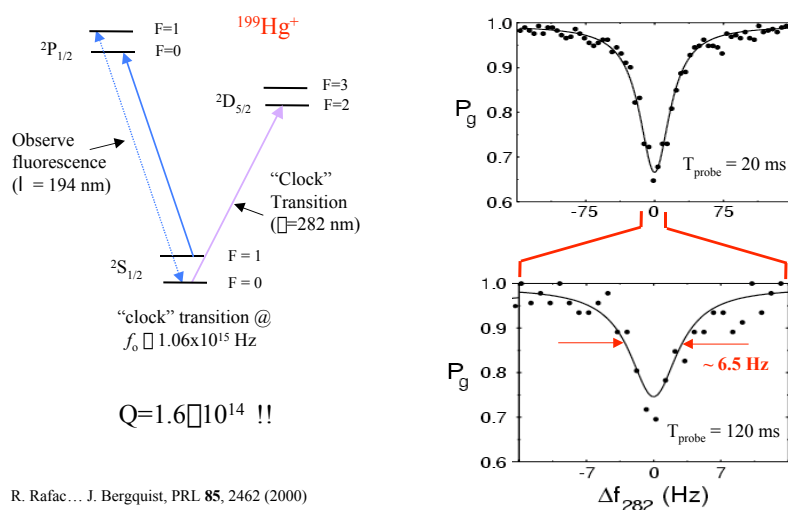


Slide 3 Schematic diagram of the Ca trapping apparatus based on a frequency-doubled diode laser. With this system we can load $\sim 10^7$ atoms in 20 ms.



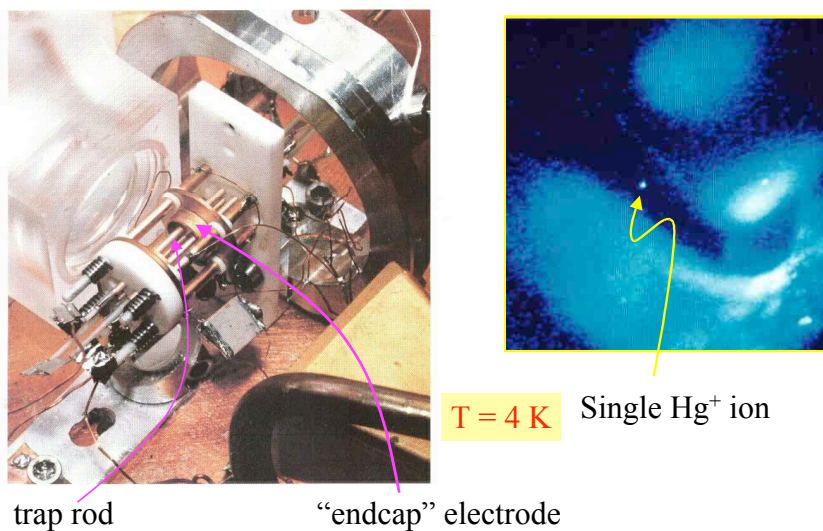
Slide 4 Measurement sequence for the generation of Ca spectroscopic signals. Normalized shelving detection improves the signal-to-noise ratio by more than one order of magnitude over red fluorescence detection.

Single Hg^+ Ion Optical Standard



Slide 5 Ultra-high resolution spectroscopy of a single trapped ^{199}Hg ion. Linewidths shown are Fourier-transform limited.

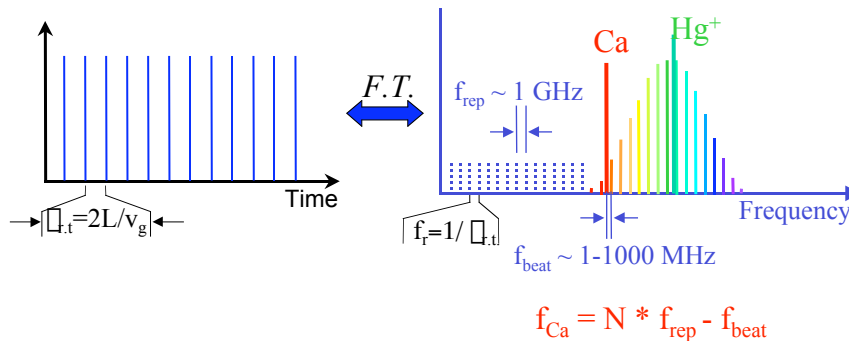
Cryogenic Hg^+ trap



Slide 6 Photographs of ion trap (left) and a single trapped ion (right).

Mode-locked fs-laser-based frequency combs

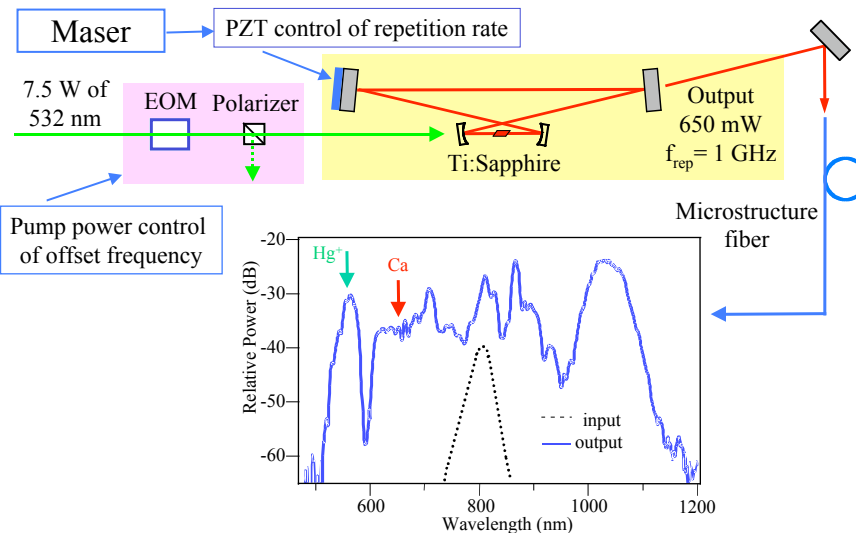
Periodicity in Time Domain = Periodicity in Frequency Domain



•Initial efforts/ideas: J. Eckstein, A. Ferguson & T. Hänsch (1978), V. P. Chebotayev (1988)

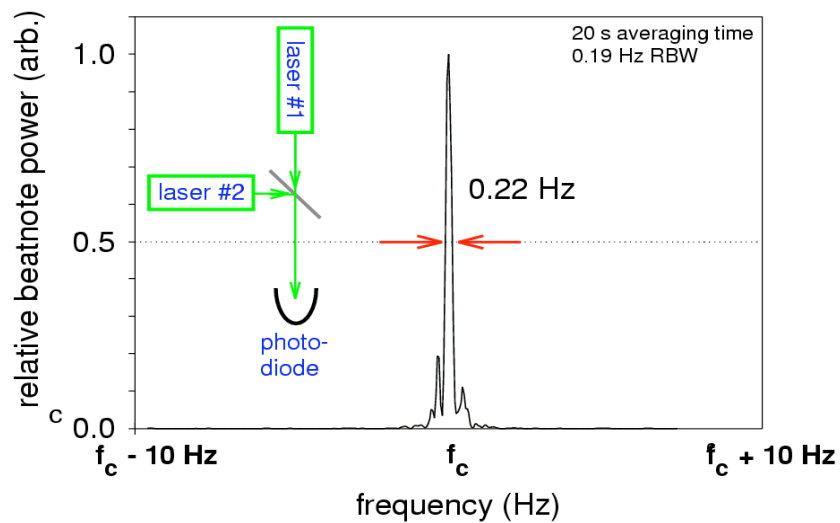
Slide 9 Introduction to mode-locked fs-laser-based frequency combs. The Fourier Transform of the pulse train in the time domain yields a comb of evenly-spaced (frequency spacing equal to the repetition rate) lines in the frequency domain.

Output spectrum of stabilized fs-laser



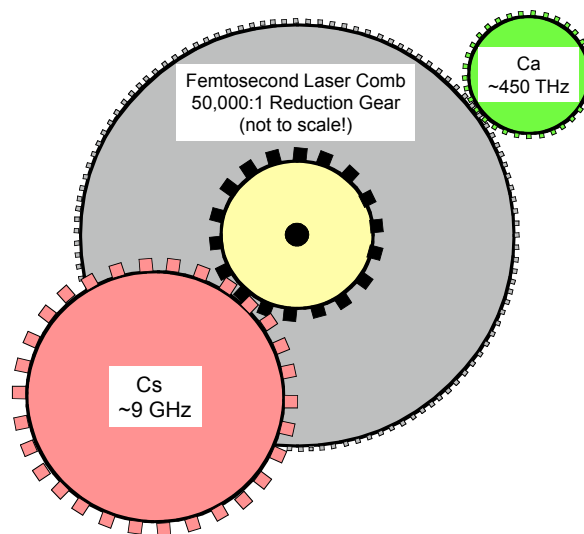
Slide 10 “Self-referencing” of the comb produces a signal used to control the offset frequency between the comb lines and absolute zero. Locking up the repetition rate to a maser referenced to the NIST time scale then enables absolute frequency measurements of the optical standards. To increase the frequency span of the comb to one octave or more, the output of the fs-laser is sent through a microstructure fiber.

Beatnote Between Lasers Stabilized to **Independent** Cavities



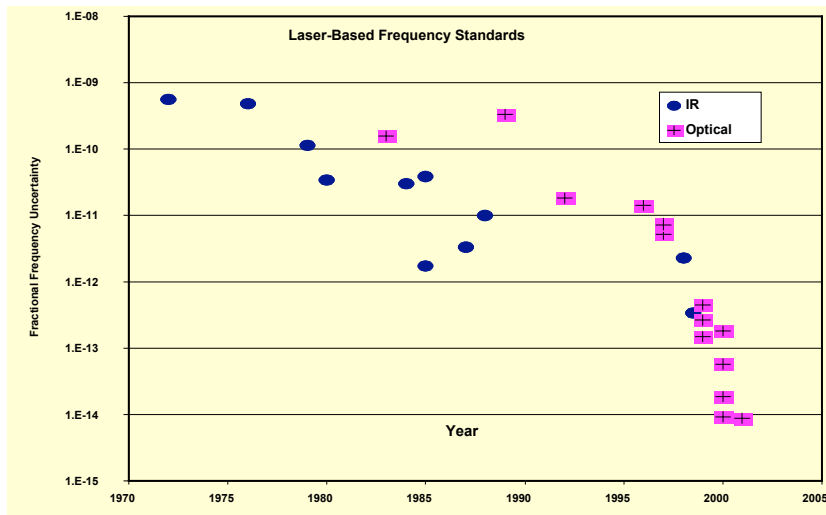
Slide 7 Spectroscopy at the decahertz level requires extremely stable lasers. Here the resultant beatnote between lasers locked to independent cavities shows a width well under 1 Hz over an averaging time of 20 s.

RF to optical clockwork with a femtosecond laser comb



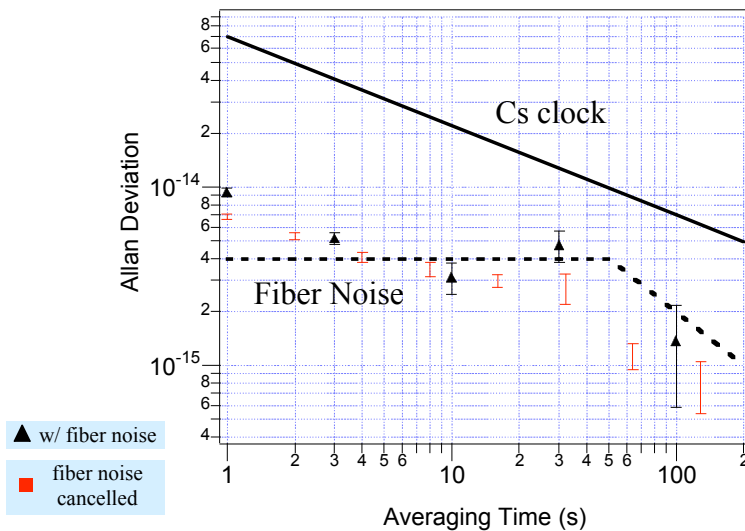
Slide 8 In order to connect frequencies between the optical and microwave domains we use a mode-locked femtosecond laser to serve as a “reduction gear”.

Absolute frequency measurements



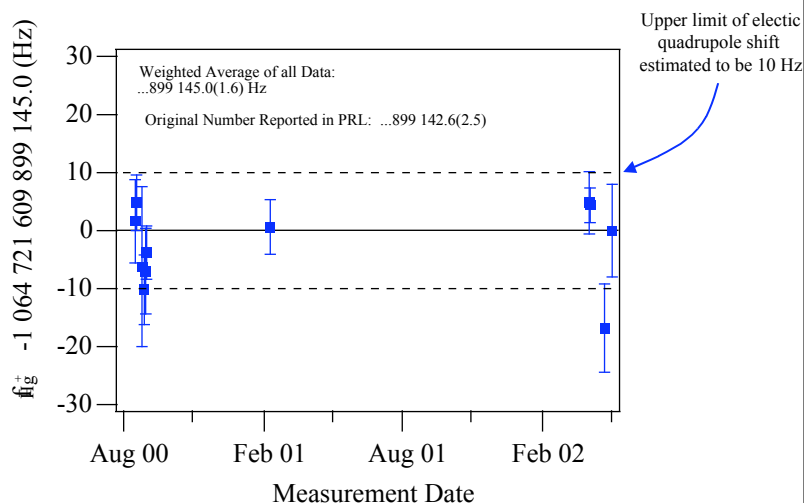
Slide 11 The introduction of mode-locked fs-laser frequency metrology has revolutionized the field of optical standards. Here we see the dramatic increase in the number of absolute frequency measurements per year.

NIST optical clock comparison - Hg^+ vs. Ca



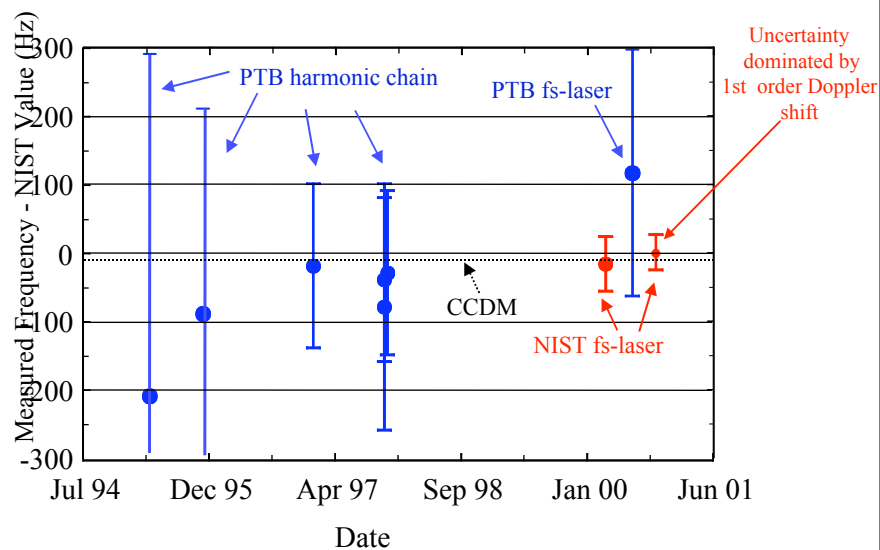
Slide 12 The measured Allan Deviation between the Hg^+ and Ca systems. The 76 THz frequency gap between the standards is bridged by the mode-locked laser. Note that the optical standards perform significantly better than the best microwave atomic standards.

Hg⁺ clock absolute frequency measurements



Slide 13 A time series of frequency measurements of the Hg⁺ clock transition relative to the NIST time scale calibrated by the primary Cs standard.

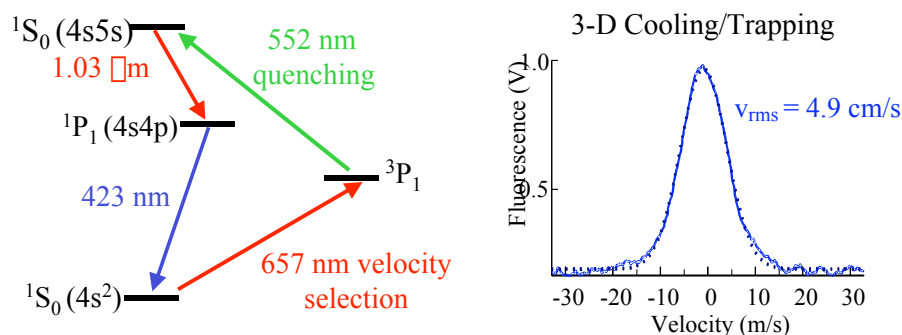
Ca absolute frequency measurements- comparisons



Slide 14 Measurements of the Ca clock transition frequency. The NIST fs-laser measurements had a statistical uncertainty of ~ 5 Hz, but residual Doppler shifts led to a final uncertainty of 26 Hz.

Quenched narrow line laser cooling of ^{40}Ca

- First demonstrated with trapped ions (Diedrich et al.)
- Use 657 nm light for high velocity selectivity
- Use 552 nm quenching light to pump atoms to ground state



Slide 15 Since the Ca clock results were limited by the residual velocity of the laser-cooled atoms ($v_{\text{rms}} \sim 70 \text{ cm/s}$), we have implemented second-stage cooling of Ca. This technique takes advantage of the high velocity selectivity of the clock transition and enhances the cooling rate by quenching the excited state with a laser at 552 nm.

Status and future work

- | | |
|---------------|--------------------------------------------------------------------------------------------------------------------------------------------------------------------------------------------------------------------------------------------------------------------------------------------------------------------------------------------------------------------------------------------------------------------------------------------|
| Hg^+ | <ul style="list-style-type: none"> - projected fractional frequency uncertainty $\sim 10^{-18}$ and short-term instability of 10^{-15} @ 1s - two years of Hg^+, Ca, and Cs intercomparisons - recently completed construction of second ion trap and cooling for evaluation of systematic shifts |
| Ca | <ul style="list-style-type: none"> - projected short-term instability of 10^{-16} @ 1s and fractional frequency uncertainty of $< 10^{-16}$ - recent second-stage cooling results should lead to improved clock accuracy - second-stage trapping should enable efficient loading of a far-detuned optical lattice for further cooling and confinement to the Lamb-Dicke regime |

Slide 16 Future improvements in these standards should produce fractional frequency uncertainties below 10^{-16} .

Relevant Publications

L. Hollberg, C. W. Oates, E. A. Curtis, E. N. Ivanov, S. A. Diddams, Th. Udem, H. G. Robinson, J. C. Bergquist, R. J. Rafac, W. M. Itano, R. E. Drullinger, and D. J. Wineland, “Optical Frequency Standards and Measurements”, J. Quant. Elect. **37**, 1502 (2001).

S. A. Diddams, Th. Udem, J. C. Bergquist, E. A. Curtis, R. E. Drullinger, L. Hollberg, W. M. Itano, W. D. Lee, C. W. Oates, K. R. Vogel, and D. J. Wineland, “An optical clock based on a single trapped Hg-199(+) ion”, Science **293**, 825 (2001).

Th. Udem, S. A. Diddams, K. R. Vogel, C. W. Oates, E. A. Curtis, W. D. Lee, W. M. Itano, R. E. Drullinger, J. C. Bergquist, and L. Hollberg, “Absolute frequency measurements of the Hg^+ and Ca clock transitions with a femtosecond laser”, Phys. Rev. Lett. **86**, 4996 (2001).

R. J. Rafac, B. C. Young, J. A. Beall, W. M. Itano, D. J. Wineland, and J. C. Bergquist, “Sub-dekahlertz ultraviolet spectroscopy of Hg-199(+)”, Phys. Rev. Lett. **85**, 2462 (2000).

E. A. Curtis, C. W. Oates, and L. Hollberg, “Quenched narrow-line laser cooling of ^{40}Ca to near the photon recoil limit”, Phys. Rev. A **64**, 031403(R) (2001).

T. Binnewies, G. Wilpers, U. Sterr, F. Riehle, J. Helmcke, T. E. Mehlstaubler, E. M. Rasel, W. Ertmer, “Doppler cooling and trapping on forbidden transitions”, Phys. Rev. Lett. **87**, 123002 (2001).

Spin-Mass Interaction Low-Temperature Experiment on ISS

Ho Jung Paik and M. Vol Moody

Department of Physics, University of Maryland, College Park, MD 20742

Donald M. Strayer

Jet Propulsion Laboratory, 4800 Oak Grove Drive, Pasadena, CA 91109

The objective of SMILE (Spin-Mass Interaction Low-temperature Experiment) is to search for interaction between intrinsic spin of particles and mass. SMILE is an ISS experiment capable of approaching, to within a factor of 100, the spin-mass interaction allowed for the axion. The Brownian motion provides the ultimate limit of sensitivity for a gravity experiment. The low-g environment of space permits nearly free suspension of the test mass, under which the highest resonance quality factor can be attained, limited only by interaction with residual gas molecules. SMILE employs a superconducting differential angular accelerator, a very sensitive force sensor. The differential accelerometer is capable of rejecting the accelerations of the platform to extremely high precision. The spin source is an elongated toroid with alternating sections formed from two high-permeability materials with different saturation spin densities.

1. Objectives of SMILE

Several modern theories predict the existence of light-mass pseudoscalar bosons, which should give rise to a force between intrinsic spin and mass. The best motivated of such bosons, the *axion*, appears in the well-known Peccei-Quinn (1977) solution to the “strong CP problem” of particle physics. For an electron with spin polarized in the direction \hat{n} and an unpolarized nucleon, the interaction potential is given (Moody and Wilczek, 1984) by

$$V_a = g_s g_p \frac{\hbar^2}{8m_e} (\hat{n} \cdot \hat{r}) \left[\frac{1}{r} + \frac{1}{r^2} e^{-r/\lambda} \right], \quad (1)$$

where m_e is the mass of the electron, \hat{r} is the unit position vector of the nucleon relative to the electron, and λ is the range of the force, which is inversely proportional to the axion mass. The dimensionless coupling constants g_s and g_p are related to α and β (Blaser *et al.*, 1996) by

$$g_s g_p \approx \frac{\alpha}{\beta^2} \approx 6 \times 10^{33}, \quad (2)$$

where α is a dimensionless angle $\approx 3 \times 10^{-10}$ and β is in meters.

The best direct limit on $g_s g_p$ at short range comes from the experiment of Ni *et al.* (1999): $g_s g_p < 1 \times 10^{-28}$ for $\beta \geq 3$ cm. SMILE (Spin-Mass Interaction Low-temperature Experiment) aims at approaching the axion limit to within two orders of magnitude at $\beta = 1$ mm. Although the experiment may fall short of actually detecting the axion, it will search for generic spin-mass coupling mechanisms 10^8 times weaker than currently observable. A positive result would constitute the discovery of a new interaction in nature, and would have a major impact in particle physics and astrophysics.

Figure 1 shows the expected resolution of SMILE versus α . Also shown are the best existing limit by α , the theoretical upper limit for the axion, and the expected resolution of our ground experiment, and the potential sensitivity of a free-flyer experiment. SMILE will demonstrate many crucial components of the ultimate free-flyer experiment, including the high Q of the test masses in micro-g and the acceleration rejection capability of the detector.

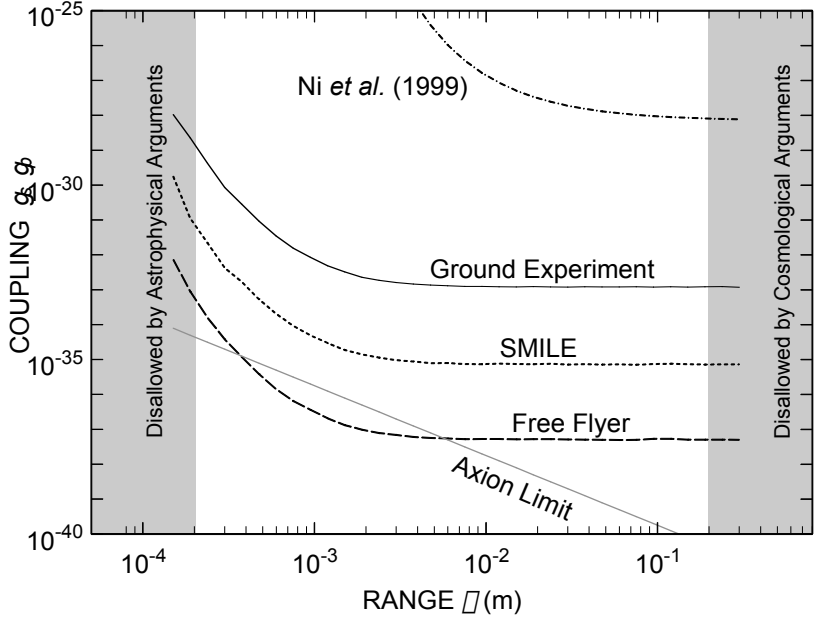


Figure 1. Sensitivity of SMILE versus the existing limit.

2. Scientific Value of Spin-Mass Coupling Experiment

Test of General Relativity. The existence of a spin-mass coupling implies a violation of the Equivalence Principle, a cornerstone of General Relativity. Although STEP (Satellite Test of the Equivalence Principle) aims at extending the limits of the Equivalence Principle to one part in 10^{18} , the spin-coupling violation cannot be detected by STEP, since it uses unpolarized test masses. Thus SMILE complements STEP in testing General Relativity.

Strong CP problem. The Standard Model of particle physics successfully accounts for all existing particle data; however, it has one serious blemish: the strong CP problem. Strong interactions are such that parity (P), time reversal (T), and charge conjugation (C) symmetries are automatically conserved in perturbation theory. However, non-perturbative effects induce violations of P and CP , parameterized by α . The *a priori* expectation of α is of the order of unity, but no violations of P or CP have been observed in strong interactions. In particular, present upper bounds on the neutron electric dipole moment (Altarev *et al.*, 1992) require $\alpha \leq 3 \times 10^{-10}$. Peccei and Quinn (1977) developed an attractive resolution of this problem. One ramification of their theory is the existence of a new light-mass boson, the *axion* (Weinberg, 1978; Wilczek, 1978).

Thus, the detection of spin-mass coupling at the level predicted by axion models would provide the first direct experimental confirmation of a solution to the serious deficiency in the Standard Model. In a more general sense, the detection of spin-mass coupling would be the first observation of macroscopic parity (P) and time reversal (T) symmetry violation.

Cold dark matter. The axion could also solve the major open question in astrophysics: the composition of dark matter. Galactic rotation curves and inflation theory require that there should be more mass in the universe than has been observed. Although neutrino mass, MACHOs (MASSive Compact Halo Objects), and many hypothetical particles have been offered as explanations, the solution remains elusive. The axion is one of the strongest candidates for the cold dark matter (Turner, 1990).

3. Principle of Experiment

Required sensitivity. The torque between a polarized source with an electron spin density ρ_s and a test mass of nucleon density ρ_N is given (Blaser *et al.*, 1996) by

$$N_a = \frac{\rho_s}{\rho_N} \frac{1}{4\pi} \frac{dI}{d\rho} (\text{mks}), \quad (3)$$

where I is the integral of the potential:

$$I = \frac{1}{8\pi} \int \int \frac{\rho_s(\mathbf{r})}{r} + \frac{1}{r^2} \rho_N(\mathbf{r}) dV_s dV_N. \quad (4)$$

Here the integration is performed over the volumes of the spin source and the test mass. There is some subtlety involved in the design of a spin source. The integral I vanishes identically for any closed loop of spin (Shaul *et al.*, 1996). Thus, a source with alternating materials is needed, with the greatest possible contrast in spin density.

Figure 2 shows the angular acceleration signal computed for our source and detector design as a function of ρ for $\rho = 3 \times 10^{-10}$. A maximum differential angular acceleration signal of $1.0 \times 10^{-19} \text{ rad s}^{-2}$ occurs at $\rho \sim 1 \text{ mm}$. To achieve the required sensitivity, the intrinsic noise of the instrument as well as its isolation from seismic, gravitational, and electromagnetic disturbances must be improved by several orders of magnitude over existing devices.

Spin source. Figure 3 shows the cross section of the spin source and a test mass perpendicular to the rotation axis, along with associated coils. The source is an elongated toroid with 32 alternating sections formed from two high-permeability materials with different saturation spin densities. Sixteen ridges on the inner surface of the test mass shell allow coupling to the spin source. To generate a differential torque, the ridges of test mass 1 are aligned with material A while those of test mass 2 are aligned with material B. A low-frequency current through toroidal windings modulates the spins in the source materials. A superconducting shield (not shown) isolates the test masses from the magnetic field of the source.

Detector. The detector consists of two identical angular accelerometers. The test masses are magnetically levitated and have cylindrical symmetry to high order. Due to its quantum nature, superconducting magnetic levitation is *extremely stable*, permitting a very high passive common-mode rejection ratio (CMRR) to be maintained.

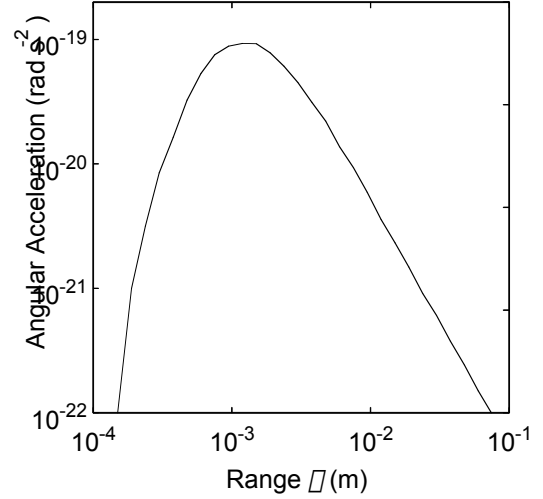


Figure 2. Angular acceleration corresponding to $\rho = 3 \times 10^{-10}$ as a function of ρ .

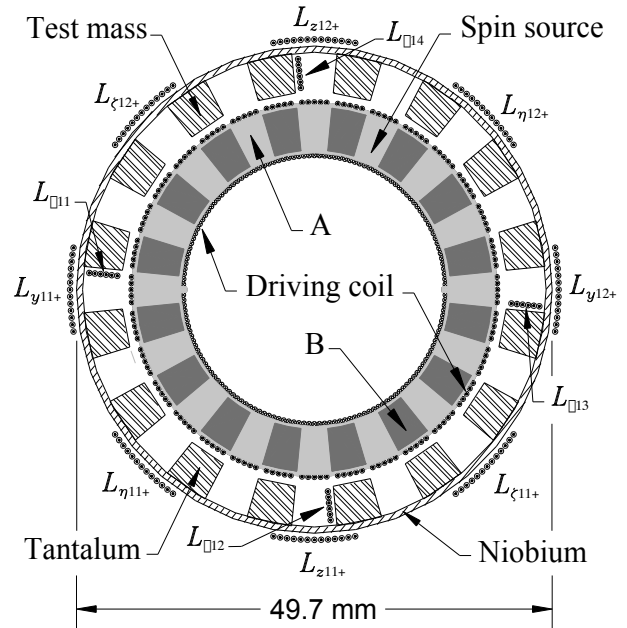


Figure 3. Cross section of the spin source and one test mass with alignment and sensing coils.

Figure 4 shows a cross section of the spin source and test masses parallel to the rotation axis. Coils coupled to the outer surfaces of the test masses permit alignment of the accelerometer sensitive axes as well as detection of the linear and angular acceleration of the platform. The two test masses are coupled together through the rotation sensing coils, facing their ridges (see Figure 3), to form a differential angular accelerometer.

Due to the *cylindrical symmetry*, the forces applied by the external coils do *not* couple to the test mass angular degree of freedom about the sensitive axis. Further, an angular accelerometer is intrinsically insensitive to forces arising from the charge on the test mass and temperature gradient across the instrument.

4. Experimental Hardware

Overview of the apparatus. The spin source is completely wrapped with a niobium (Nb) shield. Two sensing coil forms are mounted on the middle flange outside the shield, and the two test masses ride on these coil forms. Outside the test masses, four alignment coil forms are assembled and mounted on the middle flange. The entire apparatus is fastened to the second-stage thermal platform of the Cryo Insert, with its long axis pointing along-track (x -axis) (Figure 5). The temperature of the platform is stabilized to 5 \square K. The basic cryogenic requirements of

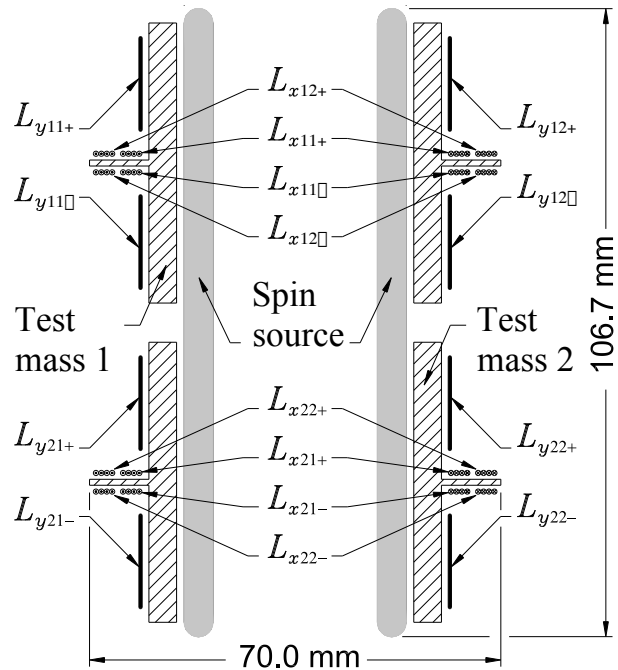


Figure 4. Cross sectional view of the apparatus along with suspension and alignment coils.

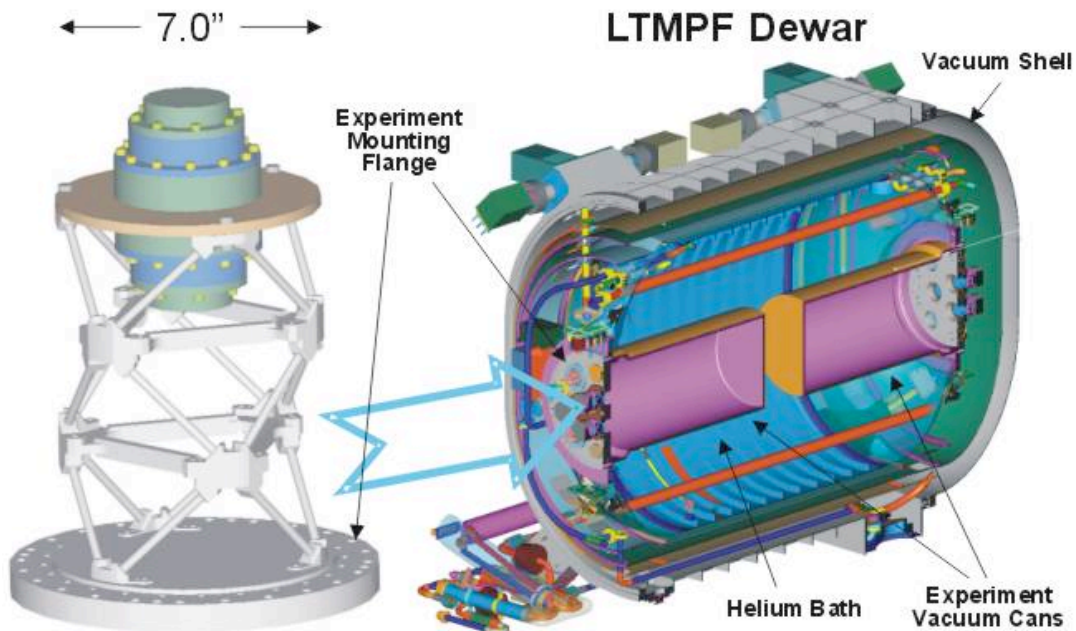


Figure 5. The ISP mounted on the Cryo Insert and the LTMPF dewar.

SMILE are met by the standard provision of LTMPF. The main upgrade required is adding a cryopump to reduce the pressure to 10^{-10} torr. Due to the excellent CMRR of the superconducting differential accelerometer, SMILE does not require vibration isolation.

Spin source. For transition metals, crystal field quenching of orbital angular momentum, L , implies that total atomic angular momentum, J , approximately equals the intrinsic spin, S . Below the Curie temperature, $\bar{\mu}_s$ is given by $2M/g\bar{\mu}_B$, where M is the magnetization, g is the spectroscopic splitting factor (≈ 2), and $\bar{\mu}_B$ is the Bohr magneton. Hence, materials with similar magnetizations will have similar spin densities. The solution lies in the use of materials containing rare-earth elements. The rare-earth elements below gadolinium (Gd) are particularly interesting, because for these, $J = L - S$, so the intrinsic spins are anti-parallel to the magnetization.

Newman (1983) used this concept in a toroidal spin source consisting of NdNi and GdNi₅. For SMILE, we propose to combine NdNi with Magnifer 7904 (80% Ni, 14% Fe, 5% Mo), a soft high- μ transition metal. The source is designed such that Magnifer completely shields NdNi, intercepting any magnetic field from it. The saturation magnetic field of Magnifer is ~ 0.75 T. When driven to an amplitude of 0.35 T, $\bar{\mu}_s$ will be modulated to $2.9 \times 10^{28} \text{ m}^{-3}$ for NdNi (Graham, 1987) and $3.0 \times 10^{28} \text{ m}^{-3}$ for Magnifer, with opposite spin directions. This results in the angular acceleration signal plotted in Figure 2.

The main structure of the source is machined out of Magnifer. Along the length of the toroid, 16 identical, evenly distributed, pockets are machined using wire EDM (electric discharge machine). NdNi is melted and poured into the pockets in the Magnifer form. A Nb coil is wound toroidally about the source to provide the charging field. A 0.38-mm thick Nb tube shields test masses from the magnetic field in the spin sources. To reduce the crosstalk between the leads, the source will be driven with a small external current through a superconducting transformer located inside the toroid.

Test masses. The test mass will have 16 ridges which interact with the source. To obtain a large nucleon density ($\bar{\mu}_N = 1.00 \times 10^{31} \text{ m}^{-3}$), the ridges will be fabricated out of tantalum (Ta), a type-I superconductor of high density (16.6 g cm^{-3}), with a relatively high transition temperature and critical field. However, to minimize the stray mass, the rest of the test mass will be made out of Nb, a lighter material (8.57 g cm^{-3}) with excellent superconducting properties. This design gives a mass of 0.28 kg and a moment of inertia of $I = 1.5 \times 10^{-4} \text{ kg m}^2$.

Two prototype test masses have been machined out of a single block of Nb, by turning the outer surfaces on a lathe and then cutting the ridges with a wire EDM (see Figure 6). To fabricate a SMILE test mass, a Ta cylinder will first be tightly fitted inside a Nb shell and diffusion-bonded. The rest of



Figure 6. Photograph of the prototype spin source, test mass, and sensing coil form.

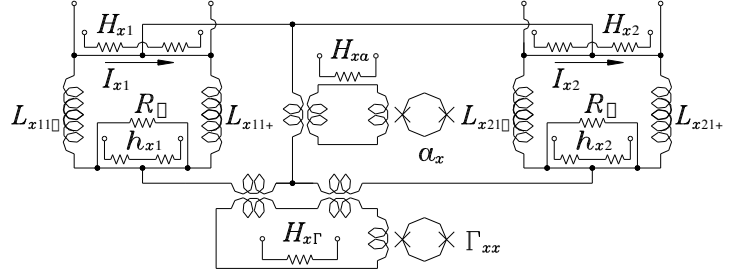
the machining will follow the procedure established for the prototype.

General requirements for the circuits. The superconducting circuits used in SMILE are of the type fully analyzed and tested in our superconducting gravity gradiometer (SGG) project (Chan and Paik, 1987; Chan *et al.*, 1987). A new feature is the feedback circuits provided for the auxiliary accelerometers, which are required to actively stiffen and damp resonant modes of the test masses. The linearity requirement of the differential accelerometer is met without feedback.

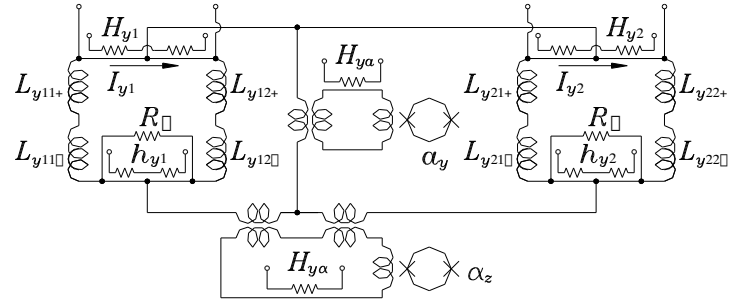
In general, higher sensitivity can be achieved by reducing the resonance frequency of an accelerometer. On the other hand, the nonlinearity of scale factors, which couples in the platform noise, favors stiffer suspension. We choose a compromise solution: the differential-mode (DM) and common-mode (CM) frequencies of $f_D = 0.01$ Hz and $f_C = 0.04$ Hz, respectively. This choice is also partially to take advantage of the quietest noise spectrum of the ISS at ~ 0.01 Hz.

The translational modes can be tuned to higher frequencies to reduce the displacements of the test masses. However, the test masses must be left as free as possible to obtain the highest Q for the accelerometer. We choose ~ 0.2 Hz, the minimum frequency required to keep the random excursion of the test masses to ≤ 10 μ m, 10% of the coil gaps. The modes are then stiffened *actively* to ~ 100 Hz to suppress the nonlinearity noise.

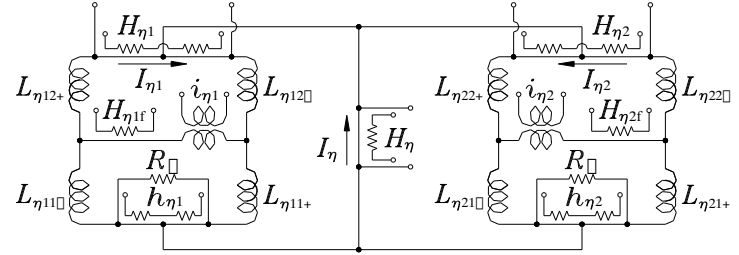
Suspension and alignment circuits. Two concentric pancake coils ($L_{xj1\pm}$'s in Figure 4) face either side of each test mass flange. Two inner coils are coupled in the circuit shown in Figure 7(a) to provide axial suspension. The two SQUIDs detect linear acceleration a_x and gravity gradient \square_{xx} along the x -axis. Two outer coils ($L_{xj2\pm}$'s in Figure 4) are coupled in an identical circuit (not shown), except



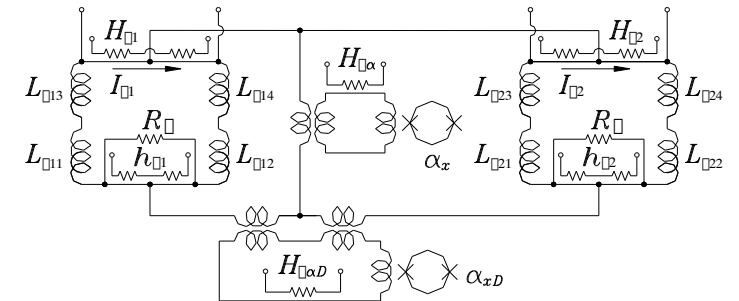
(a) Axial suspension circuit



(b) Radial suspension circuit



(c) Angular alignment circuit



(d) Signal sensing circuit

Figure 7. Superconducting circuits for SMILE.

that the SQUIDs are replaced by the leads for feedback currents. This circuit will stiffen and damp the CM and DM along the x -axis.

Eight curved pancake coils are symmetrically located about the outer surface of the cylinder on either side of the flange. The coils at 0° and 90° angles ($L_{yij\pm}$'s and $L_{zij\pm}$'s in Figure 3) are connected to suspend the radial degrees of freedom. Figure 7(b) is a schematic of the suspension circuit for the y -axis. The SQUIDs detect linear acceleration a_y and angular acceleration $\ddot{\phi}_z$.

To remove coupling to cross-component angular accelerations, the accelerometer axes must be aligned precisely. The coils located at 45° angles ($L_{\phi j\pm}$'s and $L_{\psi j\pm}$'s in Figure 3) are used to provide this alignment. Figure 7(c) is the alignment circuit for the $y = z$ plane. This circuit is also used to control the angular motion about the $y = \phi z$ axis and the linear motion along the $y = z$ axis. The signals from the radial suspension circuits are mixed with proper scale factors and fed back to the feedback transformers to stiffen and damp both the linear and angular modes.

Angular acceleration sensing circuit. Four elongated pancake coils ($L_{\phi j}$'s in Figure 3) are provided for each test mass to sense the angular motion about the symmetry axis. These coils are connected in a circuit shown in Figure 7(d) to form a differential angular accelerometer. The two SQUIDs sense the common ($\ddot{\phi}_x$) and differential ($\ddot{\phi}_{xD}$) angular acceleration about the x -axis. The current ratio, $I_{\phi}/I_{\phi'}$, is adjusted to balance out the CM from the DM output. With the angular modes not actively controlled, the DM of $Q_D = 10^{10}$ implies a decay time of 10 years! The SQUID protection heat-switches, $H_{x\phi}$ and $H_{x\phi'}$, are turned on when the modes get excited.

To wind the elongated pancake coils, the coil form holder is cut from Nb by wire EDM. In four orthogonal ridges, pockets are removed and filled with Stycast epoxy (see Figure 6) such that, when a coil is wound, it is partially on the Nb and partially on the epoxy. The part on the epoxy is the active component of the coil, which senses the angular displacement of the test mass. The coils have been successfully fabricated using this procedure for the ground apparatus.

Coarse and fine heat-switches. Due to the high vibration levels of ISS, a special provision must be made to be able to fine control the magnetic fluxes trapped in various superconducting loops. While a current is sent from a current source to a circuit, a test mass undergoes a random excursion of $10 \mu\text{m}$, which is about 10% of the nominal spacing of the coils. This means that at the moment the heat-switch is turned off, the coil inductance, hence the trapped flux, is uncertain to 10%, regardless of the resolution of the external current supply. To overcome this problem, two sets of heat-switches are provided.

Coarse heat-switches (H_{ij} 's in Figure 7) warm up a short length of the Nb wire to a resistance $R \approx 1 \text{ m}\Omega$, resulting in an L/R time of about 10 ms. These switches are used to store the currents initially. Fine heat-switches (h_{ij} 's) couple a low resistance path with $R_{\phi} \approx 0.1 \Omega$ to the circuit, resulting in a time constant of about 100 s. With 1-ms time resolution of the heat-switch, fluxes can then be adjusted to 10^{15} . This gives the ability to match the scale factors to 10^{15} and align the sensitive axes to 10^{15} rad, resulting in a passive CMRR of 10^5 in all three degrees of freedom.

Dynamic error compensation. The vibration rejection capability of a superconducting differential accelerometer can be improved by compensating for the residual errors (Moody *et al.*, 1986). With linear and angular accelerations measured simultaneously, the error coefficients can be determined by shaking the platform along or about an axis and dividing the differential acceleration output by the particular acceleration component. In our laboratory SGG, the component accelerometers were balanced and aligned to 10^{14} , which gave an initial CMRR of 10^4 . Using

this error compensation technique, we were able to improve both the linear and angular acceleration rejection by a factor of 10^3 to a CMRR of 10^7 (Moody *et al.*, 2002).

Applying the same gain to the SMILE detector, we should be able to achieve a CMRR of 10^8 for angular acceleration. Due to the cylindrical symmetry, the outer coils cannot convert the linear acceleration of the platform into a torque on the test masses. The linear acceleration does couple, however, to the angular sensing circuit through mismatches in the inner sensing coils, in particular, through mismatch in the coil areas. With the expected mismatch of $\Delta A/A = 10^{-2}$ and a stiffness ratio of $(f_D/f_R)^2 = 10^{-8}$ (with feedback) between the differential angular and linear modes, the linear error coefficient for a_y and a_z becomes

$$\Delta_L = \frac{\Delta A}{A} \frac{f_D}{f_R} \frac{1}{r_S} = 5 \times 10^{-11} \text{ m}^{-1}, \quad (5)$$

where r_S is the radial position of the sensing coils. The error compensation reduces Δ_L to $5 \times 10^{-11} \text{ m}^{-1}$. The detector is insensitive to a_x .

We will use the ISS vibration noise itself to shake the detector. The accelerations will be random and cross-correlated between various degrees of freedom. However, we can apply a well-established procedure in electrical engineering for determining the transfer functions for a multiple-input system using noise alone (Bendat and Piersol, 1971).

5. Error Budget

Intrinsic instrument noise. The intrinsic noise of an accelerometer is given by the Brownian motion noise of the test masses and the noise in the readout circuit. A dc SQUID is employed as a very quiet amplifier. The effect of the amplifier noise is reduced further by conducting a *resonance* experiment. When the spin source is driven at the resonance frequency f_0 for integration time Δ the response of the test masses to both the spin-mass coupling and the Nyquist torque, as well as the back-action noise of the amplifier, increases as Q_{eff} , where Q_{eff} represents the smaller of the Q and the product $\Delta_0 \Delta$. Since the wideband noise of the amplifier is not affected, the total amplifier contribution to the noise power is reduced by Q_{eff} .

The intrinsic power spectral density of a differential angular accelerometer, operating as a resonant detector, can be shown (Paik, 1982) to be

$$S_{\Delta}(f) = \frac{8\Delta_0}{I} \left[\frac{k_B T}{Q} + \frac{k_B T_N}{Q_{\text{eff}}} \right], \quad (6)$$

where I is the moment of inertia and T_N is the noise temperature of the amplifier. The SQUID spec for LTMPF, $30 \text{ } \mu\text{V}_0 \text{ Hz}^{-1/2}$ with $1/f$ noise corner $< 0.5 \text{ Hz}$, corresponds to $T_N \approx 1.7 \times 10^{-6} \text{ K}$ at $f_0 = 10^{-2} \text{ Hz}$. With $\Delta \approx 7.8 \times 10^6 \text{ s}$ (3 months), Q_{eff} becomes 4.9×10^4 . The amplifier noise is then negligible for cases where $Q < 10^{11}$.

A crucial question is how high a Q one can achieve for weakly suspended superconducting test masses at 10^{-2} Hz . The residual gas pressure can be improved to $\approx 10^{-10} \text{ torr}$ by cryopumping with activated charcoal. The limit by residual gas damping at 10^{-10} torr is $Q \approx 10^{10}$ at 10^{-2} Hz . There is no known damping mechanism in a high-purity superconductor cooled in a low field that makes this level of Q unachievable. With $Q = 10^{10}$ and the design value $I = 1.5 \times 10^{-4}$

kg m^2 , the intrinsic noise of the differential angular accelerometer becomes $S_{\square}^{1/2}(f) = 3.1 \square 10^{-15} \text{ rad s}^{-2} \text{ Hz}^{-1/2}$. While this is a demanding sensitivity, the existing SGG has already achieved the required resolution when the sensitivity is expressed in terms of test mass displacement.

Acceleration noise. Figure 8 shows the roll (x), pitch (y), and yaw (z) angular acceleration spectra of ISS derived from the differential GPS data during a reasonably quiet period. The ISS is quietest between 0.003 and 0.03 Hz. The angular acceleration noise at the signal frequency 0.01 Hz is $\sim 1 \square 10^{-7} \text{ rad s}^{-2} \text{ Hz}^{-1/2}$. The net CMRR of 10^8 of the detector will reject this noise to $1 \square 10^{-15} \text{ rad s}^{-2} \text{ Hz}^{-1/2}$ per axis.

Figure 9 shows the linear acceleration spectra from MAMS data taken over the same period as the above GPS data. The accelerometer position with respect to the ISS center of mass (c.m.) was (16.472, $\square 0.096$, 0.222) m. Along the y- and z-axis, the amplitude of the linear acceleration is within a factor of two from the value, angular acceleration times the lever arm from the c.m. This indicates that the linear acceleration along these axes is mainly the result of the angular acceleration of ISS. This conclusion is confirmed by the fact that the linear acceleration is lowest along the x-axis, which runs within 1 m from the c.m.

With ISS fully assembled, LTMPF is expected to be at about the same distance from the new c.m. of ISS. So we use the spectra shown in Figure 9 to estimate the linear acceleration noise. The detector couples to the y- and z-axis acceleration, $3 \square 10^{-6} \text{ m s}^{-2} \text{ Hz}^{-1/2}$ at 0.01 Hz. With $\square = 5 \square 10^{-11} \text{ m}^{\square 1}$, this noise is reduced to $1.5 \square 10^{-16} \text{ m s}^{-2} \text{ Hz}^{-1/2}$ per axis.

The nonlinearity in the detector coils couples to the y- and z-axis linear acceleration as well as the angular acceleration about the x-axis. Using the nonlinearity coefficient measured in our SGG, we estimate the nonlinearity-induced noise as plotted in Figure 10 before

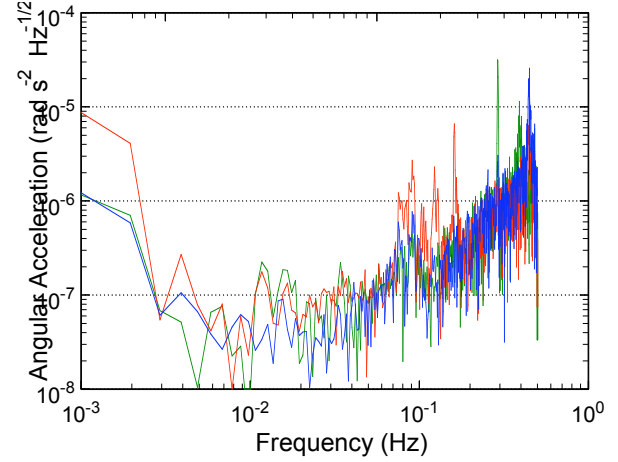


Figure 8. ISS angular acceleration about x- (red), y- (green), z- (blue) axis.

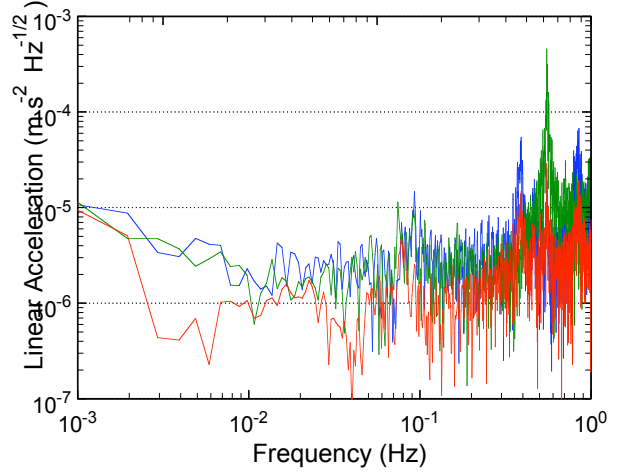


Figure 9. ISS linear acceleration along x- (red), y- (green) and z- (blue) axis.

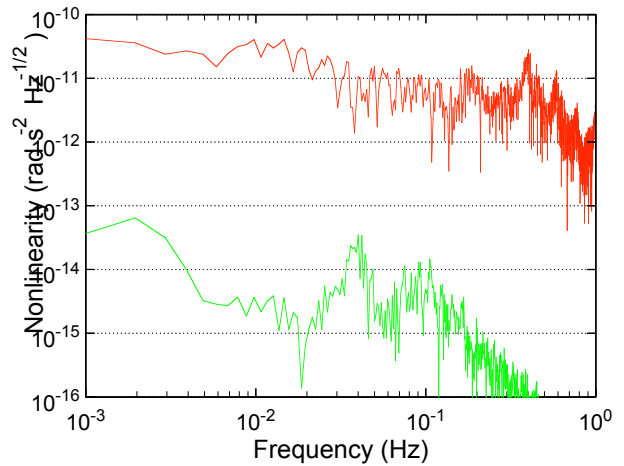


Figure 10. ISS nonlinear coupling to linear (upper) and angular (lower) acceleration.

applying feedback to the linear degrees of freedom. While angular acceleration-induced noise is at an acceptable level, $3 \times 10^{-15} \text{ m s}^{-2} \text{ Hz}^{-1/2}$, the linear acceleration-induced noise is five orders of magnitude too high! We solve this problem by actively stiffening the translational modes by five orders of magnitude to a frequency of $\sim 100 \text{ Hz}$.

Gravity noise. Helium tide, which is an important error source for STEP, is absent due to the Earth-fixed orientation of the ISS. Helium sloshing is of minor concern since it is expected to occur at a sufficiently low frequency, $\sim 2.5 \text{ mHz}$. The angular sensing and cylindrical symmetry employed makes the detector very insensitive to gravity noise from helium slosh, the Earth's gravity gradient, and ISS self-gravity, including the activities of astronauts.

The source could couple to the detector gravitationally by magnetostriction and thermal expansion. Fortunately, these effects will occur at the second harmonic and produce mainly a radial distortion of the source, which does not couple to the detector.

Magnetic noise. Cooling and performing the experiment in a low magnetic field will minimize flux creep. LTMPF is equipped with a Cryoperm shield that will help to produce a low-field region. The NdNi in the source will generate a remanent field as it cools through its Curie temperature ($\sim 30 \text{ K}$). This field will be trapped by the Magnifer and thus will be kept within the source.

Magnetic crosstalk between the source and the detector is of serious concern. The source is completely wrapped with a Nb shield and all the detector coils are mounted inside a Nb housing. The signal leads to the SQUIDS will be shielded with lead (Pb) tubing. High-purity Nb will be used and heat-treated to bring the material close to a type-I superconductor. The superconducting shield is expected to give over 200-dB isolation (Rigby *et al.*, 1990).

Electric charge effects. The levitated test masses will accumulate electric charge from cosmic rays and from high-energy protons. This charge will induce image charges on the neighboring coils and superconducting ground planes, which produce a net force through asymmetries. This would gradually displace the test masses, possibly deteriorating the CMRR of the detector. SMILE is designed to be inherently insensitive to this effect. By the fundamental nature of electricity, the excess charge always resides on the outer surface of a conductor, and the image charges on the periphery of the test mass cannot exert a torque, again due to its *cylindrical symmetry*! The radial force will couple to angular motion through asymmetry in cylindrical geometry. A cylindricity of 10^{-5} leads to a maximum angular displacement of $5 \times 10^{-9} \text{ rad}$, which is an order-of-magnitude below the level required to maintain a CMRR of 10^5 .

The patch-effect potential on the test mass ridges and angular sensing coils could produce a torque. However, most crystal domain boundaries will remain frozen at 2 K and the resulting dc torque will be balanced out upon the CM balance.

Temperature noise. The modulation of the penetration depth of a superconductor with temperature and residual thermal expansion coefficients for different materials give rise to temperature sensitivity in a superconducting accelerometer (Chan and Paik, 1987). These effects lead to a temperature control requirement of $\sim 10^{-4} \text{ K Hz}^{-1/2}$ for SMILE. A thermal link to the bath will be made to restrict the temperature rise to $< 0.1 \text{ K}$ above the bath

Error Source	Error ($\times 10^{-19} \text{ rad s}^{-2}$)
Random	(90 days)
Intrinsic	11
Vibration	12
Gravity coupling	< 1
Magnetic coupling	< 5
Electric charge	< 1
Others (30% margin)	14
Total	22

Table 1. Error budget.

temperature when 1 mW power is produced by the experiment. The temperature of the experiment will be stabilized to ± 5 mK.

Total errors. Table 1 combines all the errors. To reduce the random noise to the levels listed, a 90-day integration was assumed. The vibration noise contributes equally to the error budget as the intrinsic noise of the instrument.

6. Expected Resolution of SMILE

By equating the total noise with the acceleration signal from spin-mass interaction (Figure 2), we obtain the 1- σ resolution of SMILE plotted in Figure 1. This is compared with the sensitivities of the ground experiment as well as a free-flyer experiment. For the ground experiment, we have computed the sensitivity expected for the prototype source and test masses, which have already been fabricated.

For the free-flyer, we have scaled up the instrument by a factor of two and the noise is averaged over two detectors flown together for 360 days. Another improvement is cooling to 0.05 K by He^3/He^4 dilution refrigerator. Dilution refrigerators with this capability in zero-g are under development at NASA Ames Research Center and elsewhere (Roach and Helvensteijn, 1999). With $f_D = 10^{-3}$ Hz and $Q = 10^{10}$, the intrinsic noise is improved by more than 200. Improvement in the vibration noise will be similar. With a modest improvement of the spin contrast by a factor of two, we obtain an overall improvement of two orders of magnitude over SMILE.

Although the possible detection of the axion at the level allowed by the present theory may take an experiment on a quieter free-flyer, SMILE will search for a generic spin-coupling force in the large parameter space that has never been explored and constitutes an important new test of General Relativity. The ISS experiment will also pave way to an ultimate free-flyer experiment by testing many crucial components of the apparatus.

References

- Altarev, I. S. *et al.* (1992), *Phys. Lett. B* **276**, 242.
- Bendat, J.S. and Piersol, A. G. (1971), *Random Data: Analysis and Measurement Procedures* (Wiley, New York), Chapter 5.
- Blaser, J.-P. *et al.* (1996), *STEP (Satellite Test of the Equivalence Principle)*, Report on the Phase A Study, SCI(96) 5.
- Chan, H. A. and Paik, H. J. (1987), *Phys. Rev. D* **35**, 3551.
- Chan, H. A., Moody, M. V., and Paik, H. J. (1987), *Phys. Rev. D* **35**, 3572.
- Graham, D. M. (1987), Ph.D. thesis, University of California, Irvine.
- Moody, J. E. and Wilczek, F. (1984), *Phys. Rev. D* **30**, 130.
- Moody, M. V., Chan, H. A., and Paik, H. J. (1986), *J. Appl. Phys.* **60**, 4308.
- Moody, M. V., Canavan E. R., and Paik, H. J., submitted to *Rev. Sci. Instrum.*
- Newman, R. D. (1983), in *Proceedings of the Third Marcel Grossmann Meeting on General Relativity*, ed. H. Ning (North Holland, Amsterdam), p.1497.
- Ni, W. T. *et al.* (1999), *Phys. Rev. Lett* **82**, 2439.
- Paik, H. J. (1982), in *Proceedings of the Second Marcel Grossmann Meeting on General Relativity*, ed. R. Ruffini (North Holland, Amsterdam), p.1193.
- Peccei, R. D. and Quinn, H. (1977), *Phys. Rev. Lett.* **38**, 1440.
- Rigby, K. W., Marek, D., and Chui, T. C. P. (1990), *Rev. Sci. Instr.* **2**, 834.

- Roach, P. R. and Helvensteijn, B. P. M. (1999), in *Cryocoolers 10*, Ed. R. G. Gross, Jr. (Kluwer/Plenum, New York), p.647.
- Shaul, D. *et al.* (1996), *Class. Quantum Grav.* **13**, A107.
- Turner, M. S. (1990), *Phys. Rep.* **197**, 67.
- Weinberg, S. (1978), *Phys. Rev. Lett.* **40**, 223.
- Wilczek, F. (1978), *Phys. Rev. Lett.* **40**, 279.